5-2015

Surface-Enhanced Raman Spectroscopy-Based Biomarker Detection for B-Cell Malignancies

Nathan Israelsen
Utah State University

SURFACE-ENHANCED RAMAN SPECTROSCOPY-BASED BIOMARKER DETECTION FOR B-CELL MALIGNANCIES

by

Nathan Israelsen

A thesis submitted in partial fulfillment
of the requirements for the degree

of

MASTER OF SCIENCE

in

Biological Engineering

Approved:

_____	_____
Dr. Elizabeth Vargis Major Professor	Dr. Vincent B. Wickwar Committee Member
_____	_____
Dr. David Britt Committee Member	Dr. Mark McLellan Vice President for Research and Dean of the School of Graduate Studies

UTAH STATE UNIVERSITY
Logan, Utah

2015

ABSTRACT

Surface-Enhanced Raman Spectroscopy-Based Biomarker Detection for B-cell Malignancies

by

Nathan Israelsen, Master of Science

Utah State University, 2015

Major Professor: Dr. Elizabeth Vargis
Department: Biological Engineering

This thesis presents a light scattering-based method for biomarker detection, which could potentially be used for the quantification of multiple biomarkers specific to B-cell malignancies. This method uses fabricated gold nanoparticle probes to amplify inelastic light scattering in a process referred to as surface-enhanced Raman scattering. These gold nanoparticle probes were conjugated to antibodies for specific and targeted molecular binding. The spectrum of the amplified inelastic light scattering was detected using a spectrometer and a detector. To detect the light scattering signal from the gold nanoparticle probes, several commercial Raman spectrometer instruments were evaluated. Initial results from these evaluations are presented in this thesis. After system evaluation, a custom Raman microscope system was designed, built, and tested. This system was used for the development of a surface-enhanced Raman spectroscopy-based immunoassay. The development of this assay confirms the successful design of gold nanoparticle probes for the specific targeting and detection of immunoglobulins. The immunoassay also shows promise for the simultaneous detection of multiple biomarkers specific to B-cell malignancies.

(132 pages)

PUBLIC ABSTRACT

Surface-Enhanced Raman Spectroscopy-Based Biomarker Detection for B-cell Malignancies

Nathan Israelsen

B-cells are responsible for the production of antibodies and the recognition of dangerous pathogens. When B-cells become cancerous, they no longer perform these vital functions. This reduced B-cell activity results in greater susceptibility to opportunistic infections and increasing health risks. To effectively care for different cancer subtypes, targeted diagnosis and treatment is required. To determine the specific B-cell cancer type, up to twenty different cancer biomarkers on the cell surface need to be detected at the same time. Traditional methods are not capable of detecting such a large number of biomarkers simultaneously. This paper presents the design of a system for biomarker detection, which could be applied to the quantification of multiple B-cell biomarkers. This system uses a near-infrared laser to excite gold nanoparticles bound to the biomarkers. The system then detects light scattered off the particles to determine the concentration of biomarkers in the sample. With this method, it is possible to detect multiple biomarkers simultaneously. This method has the potential to increase the accuracy of B-cell cancer diagnosis and improve cancer prognosis through targeted cancer treatment.

ACKNOWLEDGMENTS

I would like to thank my advisor, Dr. Elizabeth Vargis, for her mentorship and encouragement through the process of completing this research. She has been a great resource and has helped me to develop myself as a professional engineer. She has encouraged personal problem solving skills, responsibility for results, and professional competence. I have learned a lot about leadership, effective communication, and educational development from her. I would also like to thank Dr. David Britt and Dr. Vincent Wickwar for serving on my graduate committee and for being open to answering questions and helping me with my research objectives.

I would like to acknowledge all of the other students in Dr. Vargis' lab. I would especially like to recognize Cindy Hanson for the many hours she has spent reading through and editing my research proposals, abstracts, and papers. I also need to acknowledge Cindy for the contribution she made to my research. Cindy and I worked together on the design of a Raman microscope system (Chapter 4 in this thesis) as it was part of both of our projects. Additionally, we collaborated on a research paper that was published in March 2015, and have worked together on various other projects in the past year and a half. I am grateful for the opportunity to learn from her and to collaborate with her on these different projects. I would also like to acknowledge Donald Wooley and Peter Haight for the many hours of help they have given in running research experiments.

I need to acknowledge the support and help of all of my family members. My parents, David and Michelle Israelsen, have provided guidance, support, and encouragement. I could not have made it this far without their help. I am grateful for the many hours of help they have given in watching my daughters and helping when they were also going through very busy years. I

would also like to acknowledge my in-laws, Rob and Marival Tanner, who have encouraged me and have given much of their time to help with watching my daughters so that I could do extra research when needed. I am thankful for my daughters, Addison and Lydia, who have been patient with their dad as he has had to go into work early and come back late.

Most of all, I am grateful for my wife, Kristie Israelsen, for her patience and her sacrifice to get me through graduate school. She has been there to help me through the ups and downs of the research process while working and a registered nurse and a mom. I truly admire her for her courage, the way she has kept going, and the way she has supported me. She has inspired me with the confidence and strength to continue working hard and to give my best effort every day. I can truly say that I would never have gotten to this point without her courage, strength, and constant help.

Finally, I need to acknowledge the hand of God in helping me to become a better person through these years of graduate school. I truly believe that he has directed me over the past year-and-a-half and I am thankful for his guidance, support, and the peace that he has brought to my life.

-Nathan Israelsen

CONTENTS

LIST OF TABLES

LIST OF FIGURES

LIST OF ABBREVIATIONS

NHL= Non Hodgkin Lymphoma

SERS = Surface-Enhanced Raman Scattering

PEG = Polyethylene Glycol

SPR = Surface Plasmon Resonance

LSPR = Localized Surface Plasmon Resonance

NIR = Near-Infrared

CCD = Charge-Coupled Device

CD = Cluster of Differentiation

CSM = Cell Surface Marker

CLL = Chronic Lymphocytic Leukemia

SLL = Small Lymphocytic Lymphoma

MCL = Mantle Cell Lymphoma

B-PLL = B-Cell Prolymphocytic Leukemia

HCL = Hairy Cell Leukemia

LPL = Lymphoplasmacytic Lymphoma

SMZL =Splenic Marginal Zone Lymphoma

NMZBL = Nodal Marginal Zone B-Cell Lymphoma

MALT = MALT Lymphoma (Extranodal Marginal Zone B-cell Lymphoma)

FCL = Follicular Cell Lymphoma

DLBCL = Diffuse Large B-Cell Lymphoma

BL = Burkitt Lymphoma

BLL = Burkitt-Like Lymphoma

PCM = Plasma Cell Meyloma

FITC = Fluorescein Isothiocyanate

TRITC = Tetramethylrhodamin Isothiocyanate

FWHM = Full-Width Half-Maximum

HOMO = Highest Occupied Molecular Orbital

LUMO = Lowest Unoccupied Molecular Orbital

SNR = Signal-to-Noise Ratio

4-ATP = 4-Aminothiophenol

4-MBA = 4-Mercaptobenzoic Acid

DTTC = (3,3')-diethylthiatricarbocyanine

EtOH = Ethanol

MeOH = Methanol

IPA = Isopropyl Alcohol

LED = Light Emitting Diode

DLS = Dynamic Light Scattering

UV/Vis = Ultraviolet/Visible Absorbance Spectroscopy

AFM = Atomic Force Microscopy

SEM = Scanning Electron Microscopy

STEM = Scanning Transmission Electron Microscopy

PBS = Phosphate Buffered Saline

TBS = Tris Buffered Saline

TBST = Tris Buffered Saline with Tween

PEG-NHS = Polyethylene Glycol-N-Hydroxysuccinimide

SH-PEG = Thiol-Polyethylene Glycol

OPSS-PEG-SVA = Orthopyridyldisulfide-Polyethylene Glycol-Succinimidyl Valerate

MWCO = Molecular Weight Cutoff

SDS-PAGE = Sodium Dodecyl Sulfate - Polyacrylamide Gel Electrophoresis

ELISA = Enzyme Linked Immunosorbent Assay

GST = Glutathione S-transferases

GSH = Glutathione

CHAPTER 1

INTRODUCTION

1.1 Motivation and Scope

B-cell malignancies include cancers such as leukemia, lymphoma, myeloma, and other lymphoproliferative disorders. B-cell cancer is particularly devastating because it causes uncontrolled cell growth and metastasis, and compromises the humoral immune system. This immunodeficiency can reduce the body's response to the cancer and promote opportunistic infections [1]. B-cell non-Hodgkin lymphoma (NHL) is one of the most prevalent cancer types in the United States comprising 4% of all new cancer cases from the years of 2007-2011 [2]. The age-adjusted incidence rate for NHL has been rising on average 0.5% each year from 2002-2011 [2]. Survival rates and prognosis can vary widely depending on the malignancy classification. For example, one study showed that the five-year survival rate for aggressive NHL ranged from 26% to 73% depending on the NHL subtype [3]. With such variability in prognosis, an effective method for targeted diagnosis and treatment of B-cell malignancies is needed.

One factor that makes the treatment of NHL and other B-cell malignancies difficult is the great diversity manifest in the disease pathology. B-cell malignancies are categorized into a variety of subtypes, and in many cases, each subtype must be treated using a different method for a successful outcome [4]. To determine the specific subtype, antibodies with fluorescent labels (fluorescent probes) are used to identify cell biomarkers. By using a variety of different probes, multiple biomarkers can be assayed simultaneously (multiplexed). This multiplex biomarker profile provides the necessary information for pathologists to subclassify the cells

and recommend an appropriate treatment. Due to the limited number of fluorescent probes that can be assayed simultaneously, this process is often difficult and time-consuming.

This research seeks to increase the number of biomarkers that can be assayed simultaneously to improve the efficiency and effectiveness of B-cell malignancy classification and biomarker targeting. To do this a new class of optical probe was used, referred to as surface-enhanced Raman scattering (SERS) probes. SERS probes can be efficiently used for multiplex biomarker classification because they have very narrow spectral profiles and they rely on a light scattering process rather than on fluorescence.

SERS probes are composed of nanoscale gold or silver particles that have reporter molecules, encased in a protective polymer, attached to their surface. As light interacts with the probe, the reporter molecules on the surface are promoted to a higher vibrational state. The vibrational changes, which occur within the molecules, cause a portion of the light to shift wavelengths as it is scattered. This process is referred to as Raman scattering. Raman scattering by these gold or silver nanoparticles can be used for very sensitive optical measurements. In fact, nanoparticle-based SERS has been used for single molecule detection [5–10].

The polymer on the surface of the nanoparticle prevents particle aggregation and enables a stable optical response, even in solutions with high ionic strength or extreme pH [11]. A commonly used polymer for protecting the nanoparticle surface is polyethylene glycol (PEG) [11–16]. PEG is biocompatible [12, 17, 18] and resists non-specific protein adsorption [19, 20]. Because of this, PEG coated SERS probes have been used for *in vivo* imaging and detection [21, 22]. Additionally, PEG can be easily conjugated to antibodies to enable specific multiplex biomarker targeting. Figure 1.1 shows an illustration of a SERS probe nanoparticle in comparison to traditional fluorescent probes.

The use of SERS probes, as opposed to the more traditional fluorescent probes, provides several advantages. First, the spectral profile of SERS probes is narrow (see Figure 1.1), enabling more probes to be assayed simultaneously [23]. Second, fluorescent probes require a specific laser wavelength, filter set, and detector. In comparison, SERS probes can be excited with a variety of laser wavelengths and require only one detector [24]. Third, SERS probes are stable in solutions of extreme pH and high ionic strength [25]. This stability enables *in vivo* cancer targeting and the detection of antigen molecules in their native environment using current methods [21, 22]. Fourth, SERS probes are more resistant to photobleaching than traditional fluorescent probes [26]. Finally, SERS probes can be optimized to produce enormous Raman scattering enhancement [27].

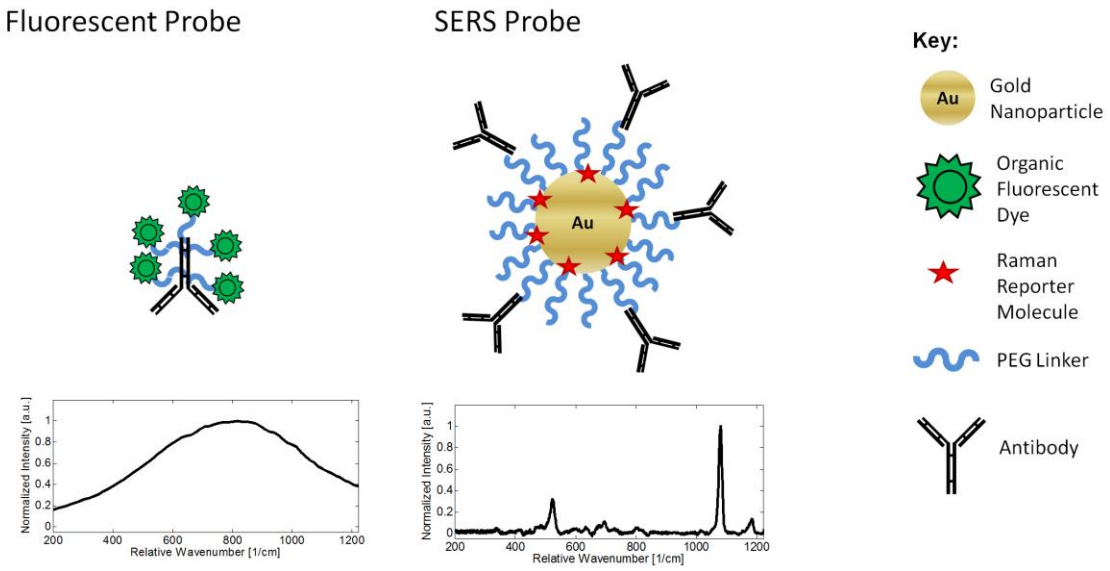

Figure 1.1 Fluorescent Probes and SERS Probes Used For Targeted Biomarker Detection. SERS probes, although much larger than traditional fluorescent probes, have several advantages including, reduced photobleaching, use with multiple excitation sources, narrow spectral profile, increased stability, and high sensitivity.

1.2 Organization

This thesis describes methods for the development and detection of SERS probes for the targeting of biomarkers, with potential applications for the detection of multiple B-cell biomarkers. **Chapter 2** provides a background and literature review of material related to B-cell malignancies, multiple biomarker analysis, and Raman spectroscopy. It also discusses the unique light scattering properties of nanoparticles and how this is helpful for Raman scattering enhancement.

Chapter 3 covers the evaluation and selection of a Raman microscope system for SERS-based measurements. Several commercial Raman systems were evaluated and compared. In the process of evaluating these systems, important factors affecting Raman system performance were compared and initial Raman experiments were run.

Chapter 4 presents the design of a Raman microscope system with near infrared (NIR) excitation. This Raman microscope system was designed using an inverted microscope base, laser, laser entry port, optical filters, spectrometer, and charge-coupled device (CCD) detector. This chapter also discusses alignment and calibration procedures for the Raman system. The acquisition of both enhanced and unenhanced Raman signals, demonstrated throughout this thesis, highlights the successful design and implementation of this Raman microscope system.

In **chapter 5**, the design and testing of SERS probe nanoparticles for the specific detection of molecular biomarkers is presented. Preliminary results and step-by-step characterization techniques that were vital for the development of optimized near infrared (NIR) SERS probes are described. Initially, SERS probes were fabricated without antibody conjugation. After the successful development of a protocol for unconjugated SERS probe fabrication, antibody conjugated SERS probe nanoparticles were developed. Conditions for the optimization

of conjugation reactions are discussed with a focus on step-by-step characterization during the multi-step conjugation process. This chapter also describes methods for the development of an immunoassay based on the light scattering properties of SERS probes.

Chapter 6 presents a summary of the important research findings detailed in this thesis and discusses the engineering significances of this work. In addition, this chapter provides recommendations for future research.

CHAPTER 2

BACKGROUND AND LITERATURE REVIEW

2.1 Overview

The development of SERS probes for the detection of B-cell malignancies requires an in-depth knowledge of both the biological and physical properties that accompany these cells during growth, maturation, and pathology. **Section 2.2** of this chapter introduces the reader to concepts related to B-cell development and characterization. This section also discusses traditional methods for the detection of cell surface markers and some limitations associated with these methods. In this section, the novelty and importance of using Raman spectroscopy as a method for B-cell malignancy detection is addressed.

The development of a SERS-based method for the classification of B-cell malignancies requires an understanding of Raman spectroscopy. **Section 2.3** discusses the theory of Raman spectroscopy and the optics and physics concepts related to this unique form of vibrational spectroscopy. This section discusses both the classical and quantum mechanics theories of Raman scattering. Additionally, the practical application of these theories for chemical detection is discussed.

In **Section 2.4**, the optical properties of nanoparticles for use in surface-enhanced Raman spectroscopy (SERS) are discussed. This section makes particular mention of the plasmonic properties of gold and silver nanoparticles and how these properties will affect Raman scattering measurements. In this section, the Mie scattering theory for nanoparticles is introduced with applications related to localized surface plasmon resonance. Finally, the applications and configurations of SERS biosensors are mentioned.

2.2 B-Cell Malignancies

B-lymphocytes (commonly called B-cells), are immune cells that develop in the bone marrow. B-cells are responsible for recognizing foreign antigens and producing antibodies for current and future targeted immune responses. The treatment of B-cell malignancies such as leukemia, lymphoma, and myeloma is a significant clinical challenge. This treatment challenge is caused by the inherent genetic variation associated with cell maturation. As B-cells mature and differentiate, they express multiple different cell surface biomarkers, including antibodies. To produce a variety of antibodies specific to foreign antigens, B-cells will undergo somatic hypermutation. In somatic hypermutation, genes that code for the antigen recognition sites on B-cell antibodies experience a high rate of mutation. This increased mutation rate results in newly developed antibodies specific to foreign antigens, and is essential to the development of humoral adaptive immunity. Many researchers have proposed that the DNA translocations, strand breaks, insertions, and deletions, which occur during somatic hypermutation, can cause the development of different B-cell cancer subtypes [28–30].

As B-cells mature, they migrate from the bone marrow to the peripheral lymphoid tissues. While there, they can become activated, either by direct antigen exposure or by T-cell mediated activation [31]. B-cell activation will result in cell division and differentiation. The B-cell will differentiate into either plasma cells or memory B-cells. The function of the plasma cell is to secrete antibodies to combat the foreign antigen. Plasma cells only live for a few days, but in that time, they produce a large amount of antibodies. It has been estimated that a single plasma cell secretes hundreds to thousands of antibodies per second [32]. The function of the memory B-cell is to preserve a copy of the specific antibody that was formed against the foreign antigen. In the case of future exposure, a memory B-cell recognizes the antigen and implements

an accelerated immune response by activating both the humoral and cell-mediated immune systems. Memory B-cells live for an extended period — for years or even decades after the initial antigen exposure [33]. B-cell malignancies are classified based on the stage of development at which genetic mutation and oncogene expression occur. Because there are many steps in B-cell maturation and differentiation, there are multiple different types of B-cell cancers that have been classified. Figure 2.1 illustrates B-cell malignancy subtypes, the developmental stage at which they are expressed, and specific genetic mutations associated with their development [34].

2.2.1 B-Cell Immunophenotyping

Throughout their maturation process, B-cells produce a variety of biomarkers, which can be useful in the identification of cell type, cell maturation, and cell pathology. Prominent biomarkers used for B-cell cancer classification are genetic lesions [35], epigenetic modifications [36], microRNA expression [37, 38], and cell surface marker (CSM) expression [39]. Due to the relative ease and consistency of identifying CSMs, a profile of CSMs is commonly used for B-cell classification [40]. For example, initial lymphocyte classification is traditionally based on the characterization of three CSMs referred to as CD20, CD3, and CD45. The CD prefix stands for cluster of differentiation, and is a classification system used primarily for CSMs [41]. A common single CD marker used to identify B-cells is CD20. The presence of CD3 is found predominantly on T-cells. CD45 (also referred to as the leukocyte common antigen) is present on both B -and T-cells. As a result, the presence of B-cells can be confirmed by a CSM profile with CD3-, CD20+, and CD45+ where - and + indicate absence and presence of the markers respectively. T-cells are identified by a profile of CD3+, CD20-, and CD45+ [42]. This type of cell surface profiling is referred to as immunophenotyping.

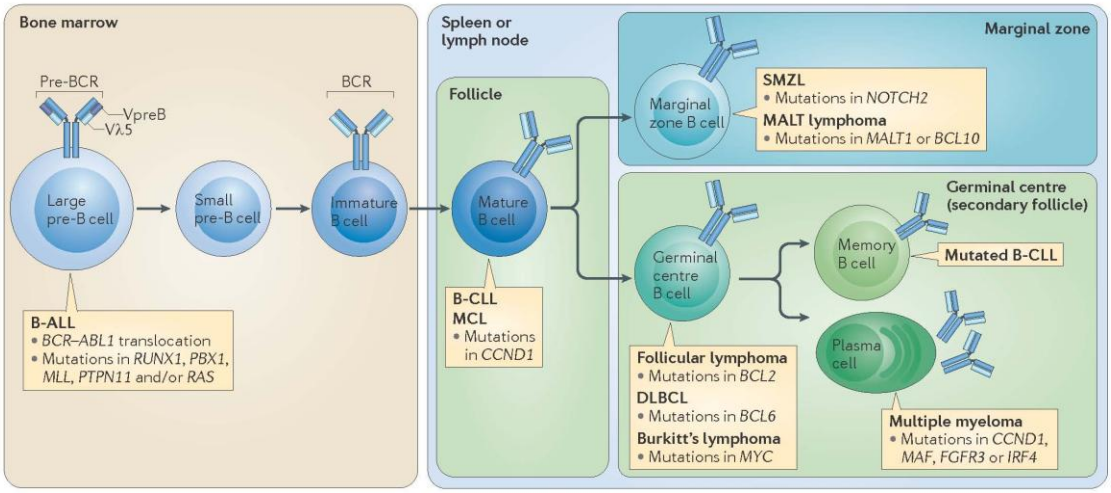

Figure 2.1: B-Cell Neoplasm's Arise At Different Stages Of B-Cell Differentiation. B-Cell malignancies have been associated with distinct stages of B-Cell development. Chromosomal translocations and gene mutations are frequently involved in these B-Cell neoplasms, and additional genetic aberrations such as hyperploidy and aneuploidy are important contributors to the disease (not shown). Reprinted by permission from Macmillan Publishers Ltd: [Nature Reviews Immunology] (R. C. Rickert, "New insights into pre-BCR and BCR signaling with relevance to B-Cell malignancies," Nat. Rev. Immunol., vol. 13, no. 8, pp. 578–591, Aug. 2013.) copyright (2013)

Immunophenotyping is essential for the diagnosis and treatment of lymphocytic leukemias, lymphomas, and other lymphoproliferative disorders [43]. In a clinical setting, initial morphological examination of peripheral blood smears or tissue sections provides enough information for the pathologist to make a general oncological classification. A more detailed classification is made by immunophenotyping. Immunophenotyping uses antibodies to detect specific CSMs and to classify the cell type, maturation stage, and cell characteristics. Through immunophenotyping, the specific cancer subtype can be identified. This is important for the effective treatment of the cancer since research has shown that the nature of the cancers genetic mutation will affect its response to cytotoxic drugs [44–46]. These examples illustrate the importance of obtaining an accurate immunophenotype before clinical treatment begins.

Table 2.1 Immunophenotypic Biomarkers For B-Cell Malignancies [40, 47–61].

	SIg	CD5	CD10	CD11c	CD19	CD20	CD22	CD23	CD43	CD103
B-CLL/SLL	w +	+	-	-	+	w +	-	+	+	-
MCL	+	+	-	-	+	+	+	(-/+)	+	-
B-PLL	+	(-/+)	-	+	+	+	+	(+/-)	+	+
HCL	+	-	-	+	+	+	+	-	+	-
LPL	+	-	-	-	+	+	+	-	(-/+)	-
SMZL	+	-	-	+	+	+	+	-	-	-
NMZBL	+	-	-	-	+	+	+	w (-/+)	(-/+)	N/A
MALT	+	-	-	-	+	+	+	-	(-/+)	+
FCL	+	-	+	-	+	+	+	(-/+)	-	-
DLBCL	(+/-)	(-/+)	(-/+)	(-/+)	+	+	+	-	-	-
BL/BLL	+	-	+	-	+	+	+	-	+	-
PCM	(-/+)	-	-	-	-	(-/+)	-	(-/+)	+	-

Notes: (+) = > 90% Expression in the cell population; (+/-) = >50% Expression in the cell population; (-/+) = <50% Expression in the cell population; (-) = <10% Expression in the cell population; (w) = weak fluorescent expression‡; SIg = Surface Immunoglobulin; N/A = Data not available; ‡marker expression not indicated as weak is expressed strongly.

B-CLL/SLL = B-Cell Chronic Lymphocytic Leukemia / Small Lymphocytic Lymphoma; MCL = Mantle Cell Lymphoma; B-PLL = B-Cell Prolymphocytic Leukemia; HCL = Hairy Cell Leukemia; LPL = Lymphoplasmacytic Lymphoma; SMZL =Splenic Marginal Zone Lymphoma; NMZBL = Nodal Marginal Zone B-Cell Lymphoma; MALT = MALT Lymphoma (Extranodal Marginal Zone B-cell Lymphoma); FCL = Follicular Cell Lymphoma; DLBCL = Diffuse Large B Cell Lymphoma; BL/BLL = Burkitt Lymphoma/ Burkitt-Like Lymphoma; PCM = Plasma Cell Meyloma

Due to the variation in cell maturation and genetics, some CSMs are expressed in only a portion of the cancer cell population. In addition, CSM expression can be observed as either weak or strong. Weak expression means that there is only a small amount of that specific CSM on the cell surface while strong expression indicates that there is a large amount of CSM on the cell surface. This is further complicated by the fact that cell autofluorescence and background staining can interfere with the fluorescent expression of labeled CSMs resulting in inaccurate and misleading CSM profiles [62]. To simplify and standardize the large amount of data used for identifying and immunophenotyping of B-cell cancers, multiple efforts have been made to

compile a list of standard B-cell immnophenotypic markers. Table 2.1 shows CSMs used to identify common B-cell malignancy variants.

2.2.2 Traditional Immunophenotyping Methods

After morphological examination, B-cell malignancies are traditionally classified using immunostaining and flow cytometry. Immunostaining is particularly useful in B-cell classification because it reveals morphological information and the location of cell specific components [63]. In B-cell immunostaining, cells are stained with antibodies and then examined under a microscope to locate diagnostic and prognostic CSMs. Detection methods used with immunostaining include fluorescent, colorimetric, chemiluminescent, enzyme-based, or nanoparticle-based methods. The selection of an appropriate detection method is critical for multiple staining procedures (when multiple CSMs are detected at the same time). To perform multiple staining, spectrally unique antibody probes are used. Using fluorescent multiple staining, up to four separate CSMs can be detected simultaneously [64].

In flow cytometry, CSMs are labeled with multiple fluorescent antibodies and then passed through a single cell channel. Each cell is excited with a laser as it passes through the channel. Following laser excitation, light scattering and fluorescence will occur. This scattered light is detected by both a side scatter detector and a forward scatter detector. The forward scatter detector is used to determine the size of the cells, and the side scatter detector determines cell roughness, and surface characteristics. When the laser source excites the fluorescent antibodies on the cell surface, the light that they emitted is detected using a series of side scattering detectors as illustrated in Figure 2.2. To separate the signals from the different fluorophores, the light is filtered into different fluorescent channels. Each channel is setup to detect only a specific range of wavelengths corresponding to a single CSM.

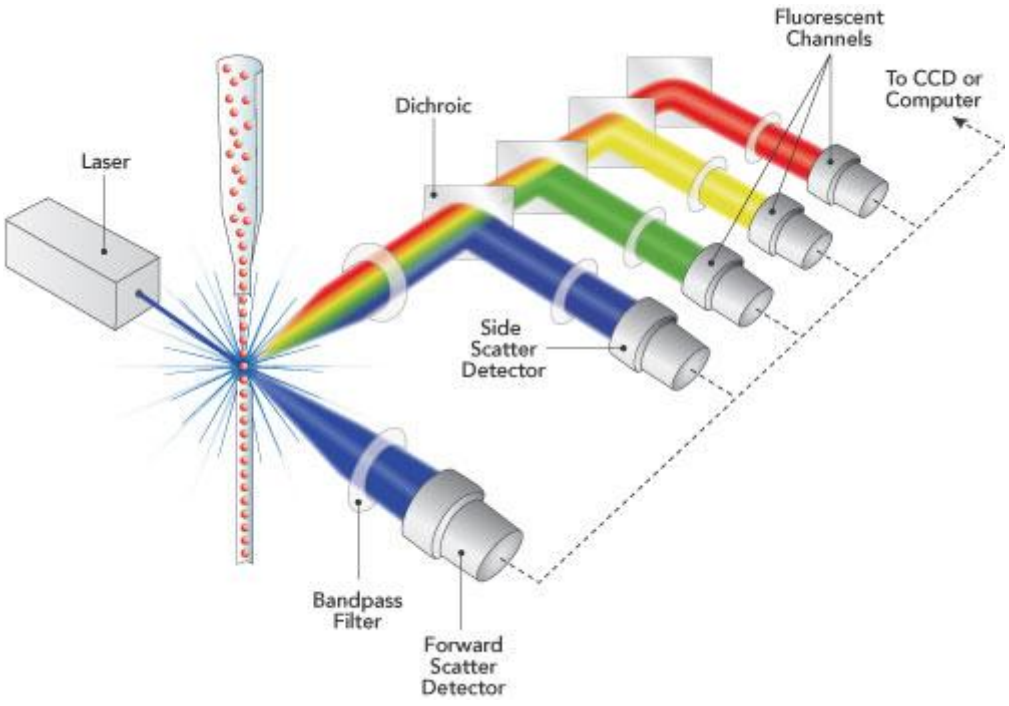

Figure 2.2 Diagram of a Multichannel Flow Cytometer. A flow cytometer can be used to detect multiple CSMs at the same time by separating the fluorescent signal into multiple fluorescent channels. Reprinted with permission of Semrock, Inc. [65].

As with immunostaining, multiplex analysis of CSMs in flow cytometry is challenging because the spectral profile of fluorescent antibodies is broad, and the tail regions of these probes overlap into the range of neighboring probes. This spectral overlap results in fluorescence cross-talk, where the emission profiles of two fluorophores overlap. In this overlapping region, signal from the first probe leaks into the fluorescent channel designated for the second probe. This cross-talk between channels results in a false signal generated in the detector. Figure 2.3 shows fluorescent spectral overlap and cross-talk that can occurs with two common fluorophores FITC and TRITC. Using both forward and side scattering data, multiple excitation lasers, and carefully designed gating strategies, flow cytometry has been used for the analysis of 10-13 different CSMs and that same time [66].

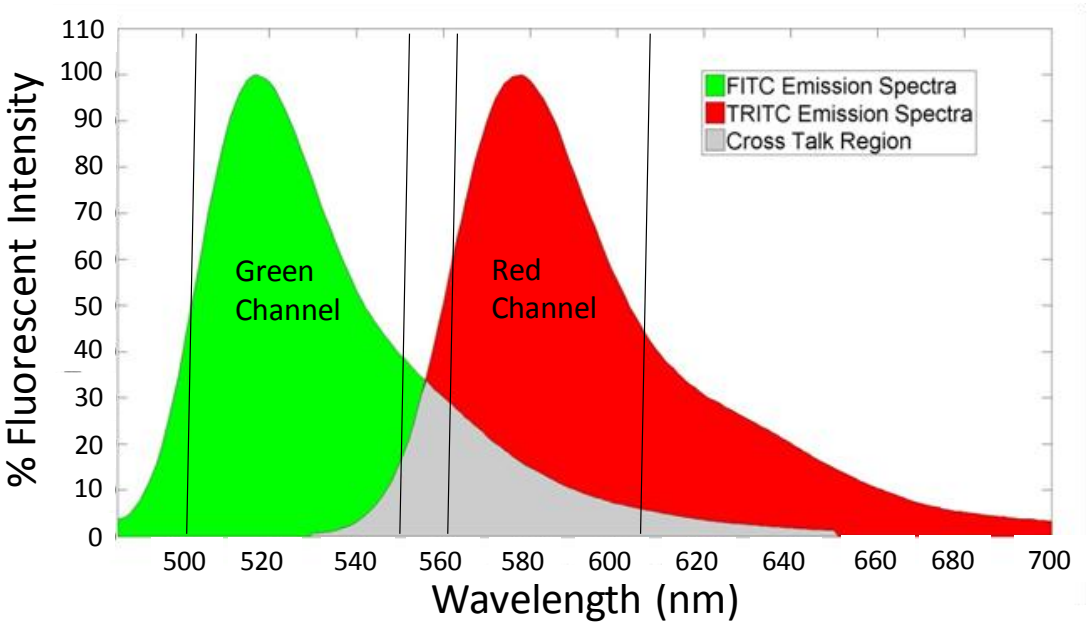

Figure 2.3 Spectral Overlap of FITC and TRITC Fluorescence Probes. Spectral overlap of FITC and TRITC spectral profiles result in significant fluorescence cross-talk. Spectral data for this figure was obtained using the LifeTechnologies™ fluorescent spectral viewer [67].

2.2.3 Quantum Dots

Nanoparticle-based optical probes have played an important role in multiplex CSM analysis. One recent development in the field of nanoparticle-based optical probes is the discovery of quantum dots [68]. Quantum dots are semiconductor nanoparticles that have a band gap that is tuned to produce fluorescence when excited with UV light. The fluorescence emission maximum of quantum dots can be turned over a large range by varying the size of the particles. Quantum dots typically range from a size of 2 - 50nm, with corresponding emission wavelengths spanning the visible and near-infrared spectrum [69–71]. Due to their symmetric spectral profile and their very narrow spectral width, quantum dots have been useful in

multiplexing applications [72, 73]. Figure 2.4 shows commercially available quantum dots and their fluorescent excitation and emission profiles.

The spectral width of an optical probe can be described by its full-width half-maximum (FWHM). The FWHM is a metric describing the peak width at half the maximum peak height. Quantum dots have a FWHM of 20-50 nm, which is smaller than many organic fluorophores, providing greater multiplexing capabilities. Another benefit of quantum dots is that all sizes can be excited with the same UV source. The biggest downside to using quantum dots for multiplex analysis is their inherent toxicity. To produce quantum dots, heavy metal ions such as selenium, cadmium, and lead are used [74, 75]. Quantum dots created with these metals have been shown to be toxic in cell culture [75], and the long-term effects of quantum dots during *in vivo* studies need further evaluation [76].

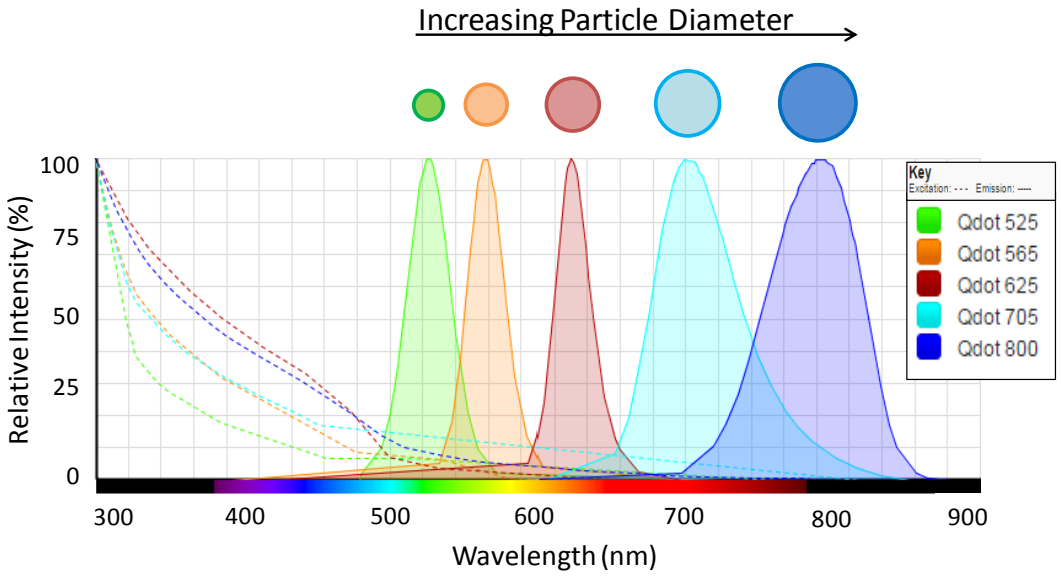

Figure 2.4 Commercially Available Quantum Dots. Due to their narrow spectral width and symmetric emission profile, quantum dots provide increased multiplexing capabilities when compared to organic fluorochrome dyes. Quantum dot spectral data was obtained using the LifeTechnologies™ fluorescent spectral viewer [67].

2.2.4 Spectral Multiplexing Methods

Colorimetric and fluorescence-based probes have produced significant advancement in the field of protein multiplexing, but alternative optical techniques such as Raman spectroscopy can provide even greater multiplexing abilities. Raman spectroscopy is a vibrational spectroscopy technique that is commonly used for chemical identification. Due to the narrow emission peaks produced in Raman spectroscopy, much greater multiplexing can be achieved. Unfortunately, standard Raman spectroscopy has limited application in multiplexing due to its low light scattering signal and sensitivity. Using surface-enhanced Raman spectroscopy (SERS), highly sensitive multiplexing probes can be created. These probes are an attractive alternative to traditional fluorescent antibodies. The multiplexing capacity of optical probe systems can be compared by examining the FWHM of the probes peak spectra. Narrow FWHMs, significantly increases multiplexing capacity. Table 2.2 shows the different methods available for CSM multiplexing, their theoretical multiplexing capabilities, and probe FWHM.

In addition to their unique multiplexing capabilities, SERS nanoparticles are resistant to photobleaching [77, 78] and are stable in a variety of environmental conditions [25, 79]. These properties have enabled researchers to develop unique labeling profiles that have not been realized before, such as highly sensitive in vivo molecular imaging using Raman spectroscopy [80]. The development of SERS probes has also promoted research directed towards theranostic applications, where both diagnosis and treatment capabilities are combined in a single agent. SERS is particularly suited for theranostic applications since it can easily be added to currently existing treatment technologies. Examples of theranostic SERS probe applications combine sensitive molecular detection with photothermal [81], photodynamic [82], or monoclonal antibody therapy [83, 84].

Table 2.2 A Comparison of Biochemical Spectral Multiplexing Methods. The multiplexing capacity describes the maximum number of probes that can be assayed simultaneously. To achieve greater multiplexing capabilities nanoparticle-based probes such as quantum dots and SERS probes are used.

Label	Detection Method	FWHM	Multiplexing Capacity (400 – 700nm)	Reference
Bio/Chemilumenscence Expression	Luminometer	60-90 nm	1-3	[77–79]
Fluorescent Dyes	Fluorescence Spectroscopy	40-70 nm	1-4	[80–82]
Quantum Dots	Fluorescence Spectroscopy	20-50 nm	3-10	[81][83]
SERS Probes	Raman Spectroscopy	3-5 nm	10-100	[81][84]

2.3 Raman Spectroscopy

Raman scattering is a type of secondary radiation that occurs when light interacts with and is scattered by molecules. This light scattering phenomenon was first discovered in 1928 by Chandrasekhara Venkata Raman [85]. Raman's observations were influenced by the early work of Lord Rayleigh, who had reported on elastic light scattering in the atmosphere in 1871 [86]. In Raman's early experiments, he used a series of lenses to concentrate sunlight onto liquid or vapor samples and observed light scattering off those samples. He observed shifts in the wavelength of the light scattered off samples, and that the extent of the wavelength shift depended on the sample type [85]. The light scattering discoveries of Rayleigh and Raman are now referred to by the names of these scientists. Rayleigh (or elastic) scattering is the dominant light scattering effect and results when light is scattered off molecules with no energy shift. Raman (or inelastic) light scattering is a comparatively weak scattering phenomenon that occurs

because of bond vibrations. In Raman scattering, photon energy is transferred as it interacts with the molecules, causing a shift in the wavelength of the scattered light. Both Rayleigh and Raman light scattering theories are now widely used to describe how light interacts with and is scattered by molecules.

2.3.1 Classical Scattering Theory

As electrons move around the surface of a molecule, they will oscillate at a natural frequency (ω). This electron oscillation can be modeled as a one-dimensional harmonic oscillator with spring constant (k) described below:

$$\omega = \sqrt{\frac{k}{M}} \qquad \text{(Equation 2.1)}$$

where ω is the natural frequency, k is the average spring constant associated with the electron oscillation, and M is the effective mass of the molecule [87]. As light interacts with the molecule, energy will be absorbed for a short period. When the incoming energy matches the natural frequency of the system (ω), the electrons will be promoted to a higher molecular orbital in the process of absorption. On the other hand, when the incoming energy does not match the system natural frequency, the electrons in the outer-most orbital of the molecule will begin to oscillate at the same frequency as the incoming light waves. This oscillation of the electron cloud results in charge separation and an induced dipole moment [88]. This induced dipole will cause the electromagnetic waves to be remitted (or scattered) in a random direction. By using this simple model, predictions can be made about the absorption and scattering properties of molecules. Figure 2.5 illustrates the classical theory of Rayleigh scattering as described above, where the energy of the incident light is labeled as E_{vo} and the scattered light is labeled as E_s.

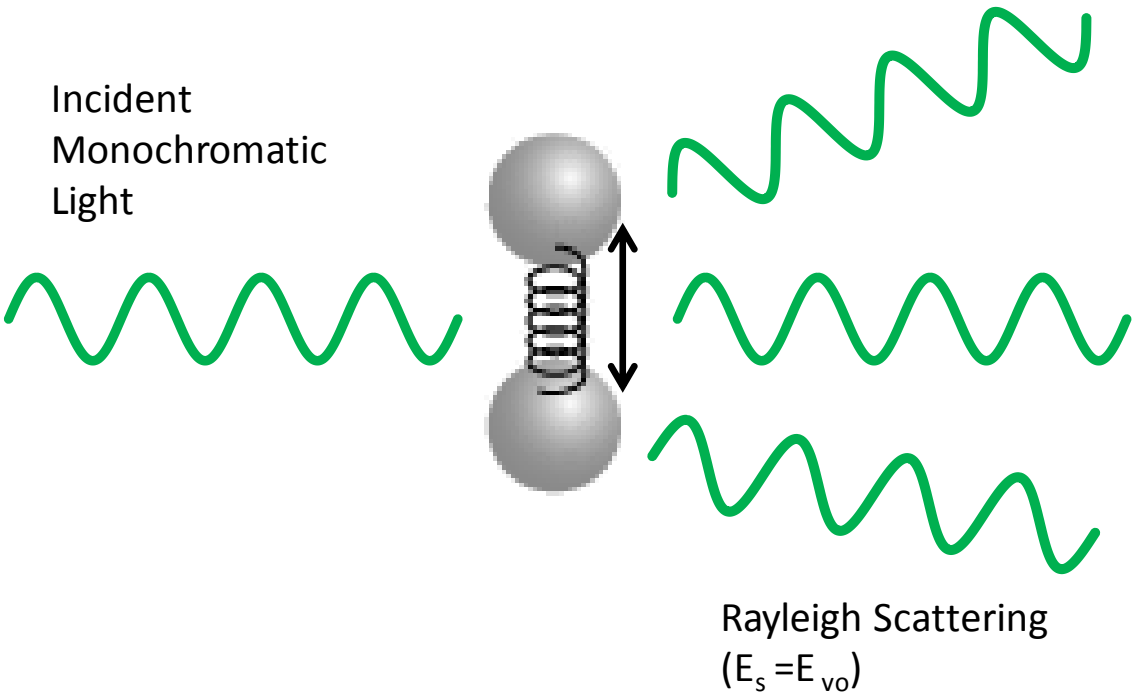

Figure 2.5 The Classical Description of Rayleigh Scattering. As incident, monochromatic light hits a molecule, an induced molecular dipole is formed resulting in elastic light scattering.

The extent to which a molecule's electron cloud can be influenced by an electromagnetic field is described using the term molecular polarizability (α). In fact, the induced dipole moment will be linearly proportional to the electric field applied to the molecules (E) and the molecular polarizability α, and can be described by the equation

$$\mu_{\mathrm{ind}}(\mathrm{t}) = \alpha(\mathrm{t})\mathrm{E}(\mathrm{t}) \qquad \text{(Equation 2.2)}$$

where $\mu_{ind}(t)$ is the time-varying induced dipole moment, $\alpha\ (t)$ is the time-varying molecular polarizability, and $E(t)$ is the time-varying applied electrical field [89]. Molecules with a large polarizability will experience a large induced dipole moment when exposed to electromagnetic radiation, while molecules with a small polarizability will only experience a small induced dipole

moment. The molecular polarizability will also be modulated by bond rotations and vibrations. In fact, when bond vibrations and rotations occur at a frequency ω_{int}, the polarizability will vary between α_{max} and α_{min} . The change in molecular polarizabilty can be expressed as $\Delta\alpha = \alpha_{max} - \alpha_{min}$. Using this terminology, the induced dipole moment can be expressed by the following equation [90]:

$$\mu_{ind}(t) = 2\left(\alpha + \frac{1}{2}\Delta\alpha\cos(\omega_{int}t)\right)E_0\cos(\omega t) \qquad \text{(Equation 2.3)}$$

In this expression, α is the mean molecular polarizability, and E_0 is the time-independent component of the electric field. Using trigonometric identities the final expression is expanded to the form seen below [90]:

$$\mu_{ind}(t) = \underbrace{2\alpha E_0\cos(\omega t)}_{\text{Rayleigh Component}} + \underbrace{\frac{1}{2}\Delta\alpha E_0\cos(\omega + \omega_{int})t}_{\text{Anti- Stokes Raman Component}} + \underbrace{\frac{1}{2}\Delta\alpha E_0\cos(\omega - \omega_{int})t}_{\text{Stokes Raman Component}} \qquad \text{(Equation 2.4)}$$

It is significant to note that in this form the time-varying induced dipole moment is made up of three components. These components are referred to as the Rayleigh, the Stokes Raman, and the anti-Stokes Raman components. The Stokes and anti-Stokes Raman components of the induced dipole result from energy exchange due to molecular vibrations and rotations. The Stokes Raman induced dipole moment results in light scattering that has a longer wavelength and lower energy than the incident light. On the other hand, the anti-Stokes induced dipole results in light scattering with shorter wavelengths and higher energy than the incident light. Figure 2.6 illustrates the three components of light scattering. In this diagram, the energy of the incident light is labeled at E_{vo} and the energy of the scattered light is labeled as E_s.

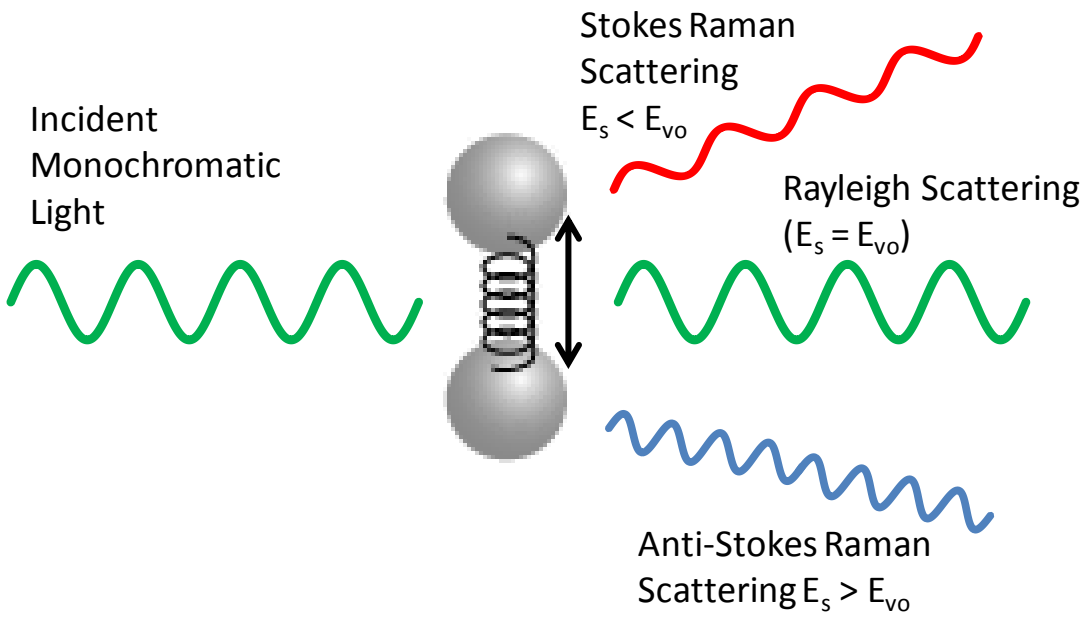

Figure 2.6 The Classical Description of Raman Scattering. As incident, monochromatic light hits a molecule, it results in an induced molecular dipole. Additionally, molecular vibration and rotation will occur within the molecule resulting in subsequent inelastic light scattering.

When light scattering occurs, it will be primarily composed of Rayleigh scattered light. However, a small portion of the light is Stokes Raman scattering, and an even smaller portion of the light is anti-Stokes Raman scattering. The varying scattering intensities are due to the low probability of Raman scattering events. Approximately 10^6-10^8 scattering events are required to generate one Raman scattered photon [91]. For Rayleigh scattering to occur, the incident photon must interact with the molecules' electrons causing electron distortion. On the other hand, Raman scattering occurs when the incident photon passes the electron cloud and hit the nucleus. The nuclear motion caused by this event induces bond vibrations and rotations, and changes in the photon energy during scattering [91]. Because the likelihood of a photon passing though the electron cloud undisturbed is very low, Raman scattering is by nature a rare occurrence. With such infrequent Raman scattering events, it is important that Raman systems

are very sensitive and are efficient at removing the dominant Rayleigh component so that the weak Raman signal can be acquired.

2.3.2 Raman Spectrum and Vibrational Modes

A typical Raman spectrum will contain multiple Raman peaks with each peak corresponding to a specific vibrational or rotational mode. Depending on the Raman setup, these peaks can be either Stokes Raman peaks or anti-Stokes Raman peaks. The Stokes Raman peaks are red shifted from the laser line, meaning they have longer wavelengths and less energy. On the other hand, anti-Stokes Raman peaks are blue shifted from the laser line. The intensities of the anti-Stokes peaks are smaller than those for the Stokes peaks. Figure 2.7 shows that the relative position of the Stokes and anti-Stokes lines remain the same while the intensity of the lines are different.

The number of peaks in a Raman spectrum will depend on the number of vibrational modes for the molecule. All vibrational modes are not necessarily seen in the Raman spectrum because some of the modes are degenerate (they have the same energy level) and because some of the modes are not Raman active. The number of vibrational modes for a molecule can be calculated based on the number of atoms contained within that molecule. Due to their symmetry about the molecular axis, the number of modes expressed by linear molecules is

$$\nu_n = 3n - 5 \qquad \text{(Equation 2.5)}$$

while the number of modes expressed by non-linear molecules is:

$$\nu_n = 3n - 6 \qquad \text{(Equation 2.6)}$$

where ν_n is the number of vibrational modes, and n is the number of atoms contained within the molecule [92]. Some vibrational modes will be Raman active and others will not. For a

vibrational mode to be Raman active there must be a net change in the polarizability of the molecule. Using a technique referred to as group theory, Raman active modes of a molecule can be determined. Group theory is a mathematical method used to model molecular symmetry and the constraints on molecule rotation and vibration [93]. Figure 2.8 shows a list of common Raman peaks and their associated molecular movements that has been compiled based on group theory calculations and experimental results found in scientific literature [94].

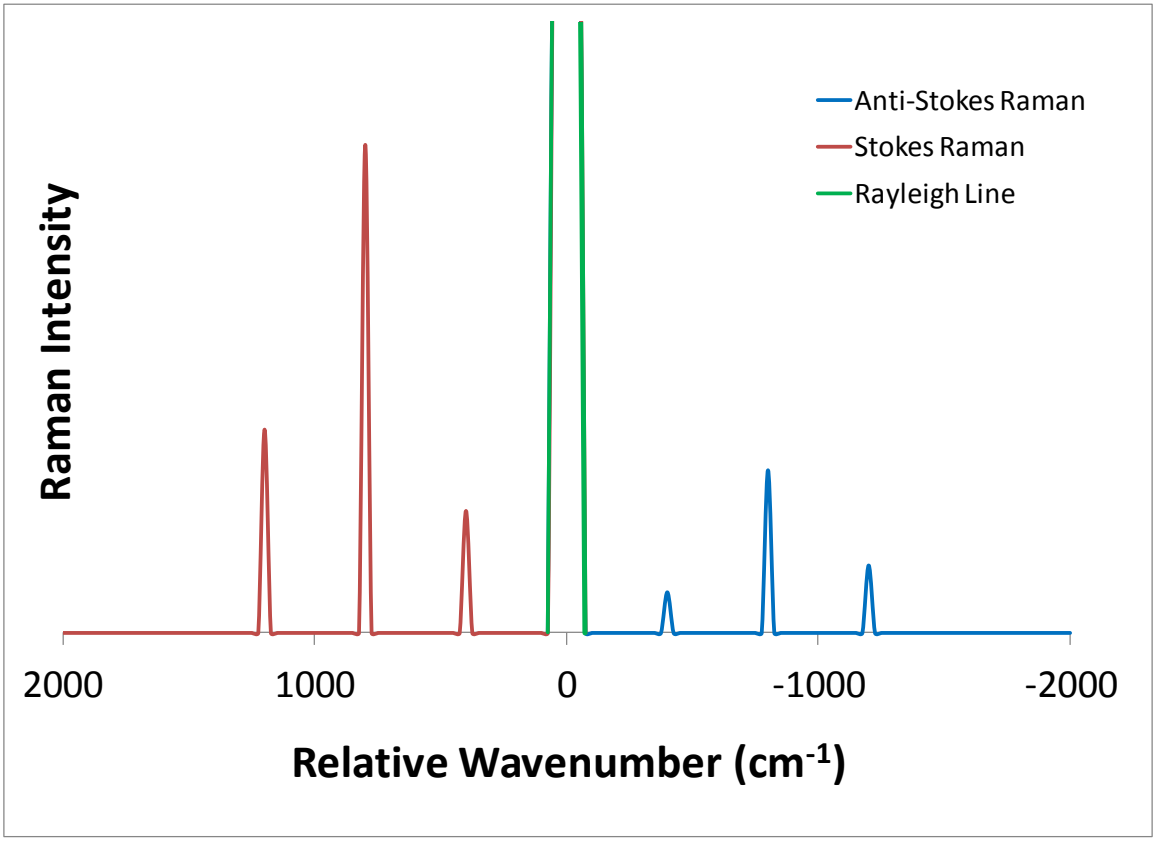

Figure 2.7 An Example Raman Spectrum. A typical Raman spectrum has multiple peaks corresponding to specific vibrational modes. Both the Stokes and anti-Stokes Raman bands are observed as well as the strong Rayleigh scattering component. The Stokes bands are stronger than the anti-Stokes bands due to the decreased likelihood of photon upconversion.

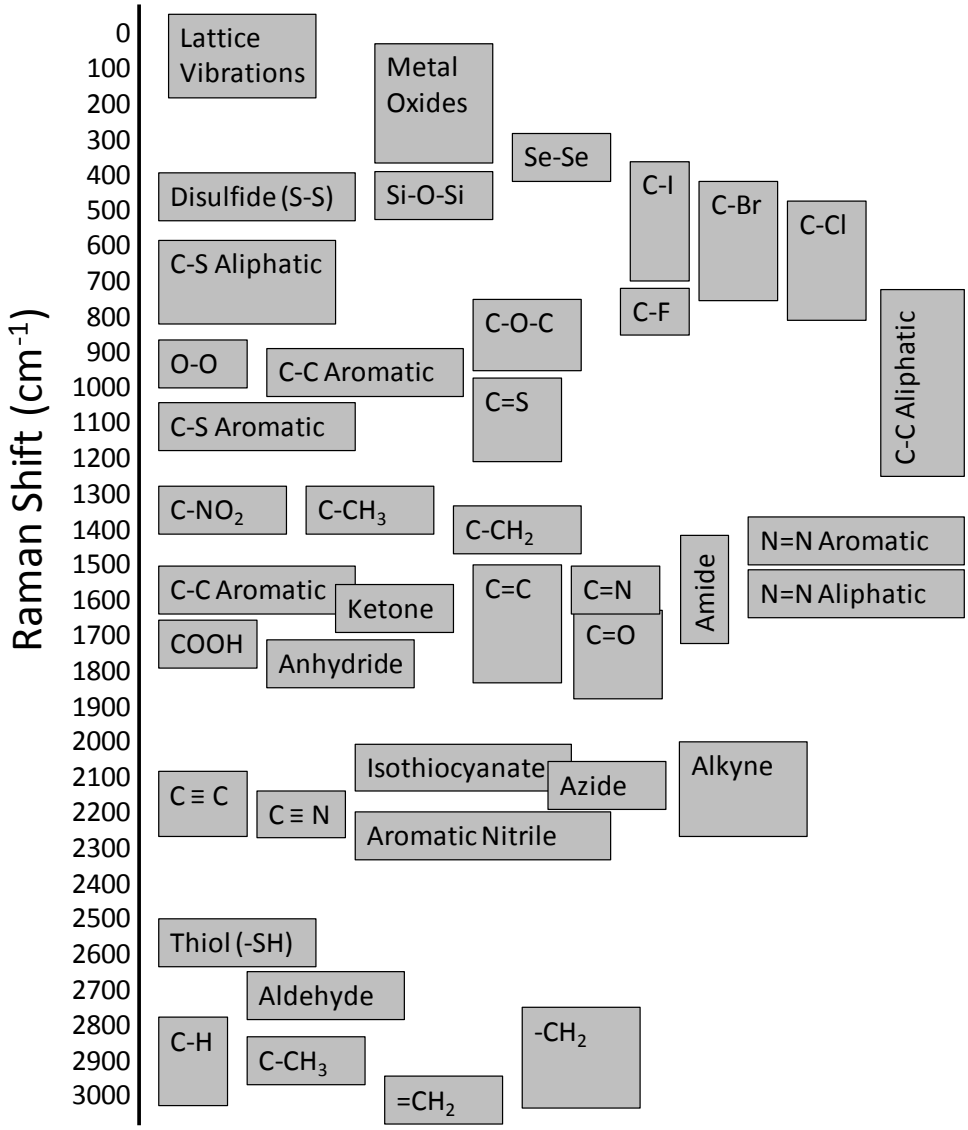

Figure 2.8 Raman Active Modes of Common Function Groups. Functional groups can be identified in a Raman spectrum based on their position relative to the excitation wavelength. Functional groups have been identified with the wavenumber range in which they are most commonly observed [93, 94].

2.3.3 Quantum Scattering Theory

To offer a deeper description of the Raman scattering process, a quantum mechanics approach is often taken. Using quantum mechanics, the interactions of photons and molecules can be described with specific quantized energy levels. Electrons will transition between these energy levels in response to photon excitation. When the frequency of the incident light matches the natural frequency of electron oscillation in the molecule, it will induce a transition of electrons from highest occupied molecular orbital (HOMO) to the lowest unoccupied molecular orbital (LUMO). This process is illustrated in Figure 2.9.

This electron state transition is referred to as optical absorption, and is the phenomenon that is traditionally used in chemical and biological sciences for the detection of molecules with conjugate bonds. Through photon absorption, the molecule transitions from its ground state to a highly energized excited state. Either energy from this excited state can be dissipated as heat, or addition energy conversion processes can take place, such as fluorescence or phosphorescence. Electron absorption and molecular vibrations are different processes, which result in a transition from the molecules ground state to an excited state. In electron absorption, an electron transitions to a higher orbital. On the other hand, in the process of molecular vibration potential energy is stored in the molecular bonds and is dissipated by the release of energy in the form of heat, light, or other forms of kinetic energy.

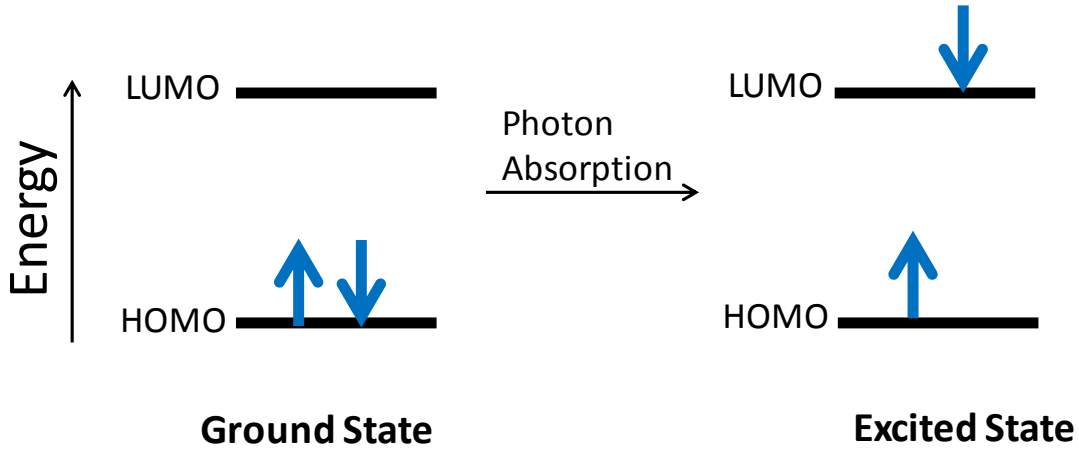

Figure 2.9 The Process of Photon Absorption. During photon absorption electrons in the highest occupied molecular orbital (HOMO) are excited by a photon and are promoted to the lowest unoccupied molecular orbital (LUMO).

The quantum mechanics description of Raman and Rayleigh scattering can be best illustrated by a comparison to the process of fluorescence. The Jablonski diagram presented in Figure 2.10 shows the process of fluorescence, Rayleigh scattering, Stokes-Raman scattering, and anti-Stokes Raman scattering. In fluorescence, a molecule is excited by a light source that matches the molecules resonance frequency. At this point, an electronic transition occurs and the molecule enters a singlet excited state (S_1) where some energy is lost due to internal conversion. After the fluorescence lifetime is completed, the electrons in the singlet excited state (S_1) fall back down to the ground state (S_0). As this occurs, an additional photon is emitted. Because the energy difference between the excited state (S_1) and the ground state (S_0) is smaller than the initial absorption energy, the photon that is emitted now has less energy than the incident photon.

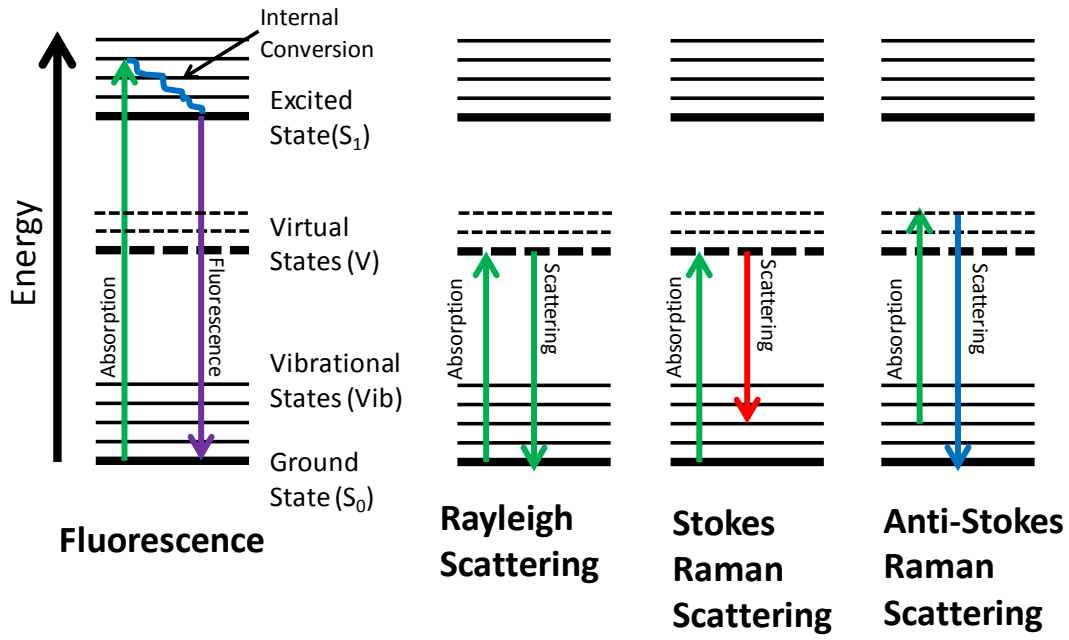

Figure 2.10 Jablonski Diagram of the Fluorescence and Scattering Processes. Fluorescence and scattering are fundamentally different processes. Fluorescence involves photon absorption followed by internal conversion. The remaining energy is remitted as a photon in the process of fluorescence relaxation. Scattering, on the other hand, results from the promotion of high-energy electrons to a virtual state and the random remission of the photon during molecular relaxation.

Light scattering processes such as Rayleigh and Raman scattering do not rely on electronic transitions, such as with absorption and fluorescence. In light scattering, the molecule will be excited to a virtual energy state (V) which is an intermediate state between the ground state (S_0) and the excited state (S_1). The promotion of the molecule to a virtual state occurs when light does not match the quantized energy level of the molecule. When this occurs, the energy is briefly captured by the molecule as an induced dipole moment. This elevated energy level or virtual energy state (V) is dissipated through light scattering. The amount of time that a molecule remains in the virtual energy state (V) is much smaller than the amount of time that it remains in the excited state. The scattering lifetime for Raman ranges from 10^{-13} to 10^{-11} seconds, while the fluorescence lifetime ranges from 10^{-9} to 10^{-7} seconds [95]. The reduced

amount of time spent in the virtual excited state is one reason that SERS probes experience reduced photobleaching [96–98].

The processes of both Stokes and anti-Stokes Raman scattering can be described by their virtual energy level transitions. In Stokes Raman scattering, light excitation promotes the molecule to a virtual state (V). After the scattering lifetime is completed, the molecule returns to a vibrational state (Vib) rather than going to the ground state (S_0). This vibrational state (Vib) results from vibrational and rotation movement caused by the incident light. The vibrational state (Vib) is near the ground state, and as a result, the energy difference between these two states is very small. As the electrons fall from the virtual excited state (V) to the vibrational state (Vib), a photon is emitted, which is red-shifted from the incident beam. By studying the spectrum of red shifted light, the vibrational and rotational bond movements can be characterized.

In anti-Stokes Raman scattering, a small portion of the molecules are already in a high-energy vibrational state (Vib), because at room temperature all molecules will experience some bond movements. As incident light hits the surface of the molecules, they are excited to a virtual state (V). After the scattering lifetime, the molecules return to the ground state (S_0), resulting in the emission of a photon that is blue shifted from the incident beam. Because it is less likely for molecules at room temperature to be in a vibrationally excited state, anti-Stokes Raman scattering occurs less frequently than Stokes Raman scattering. Additionally, the resulting anti-Stokes Raman intensity is smaller than the Stokes Raman intensity. The reduced intensity of anti-Stokes Raman scattering is not explained by classical theory, but it is effectively illustrated using quantum scattering theory [99].

2.3.4 Raman Spectroscopy in Practice

The theoretical foundation of classical and quantum mechanics theories describing Raman scattering provide a good starting point for the development of Raman spectroscopy-based applications. To implement effective Raman scattering experiments, an understanding of the practical requirements of the Raman system is also important. In Raman spectroscopy, it is important to consider the factors that will influence the Raman scattering intensity. The Raman scattering intensity will normally be directly proportional to the concentration of the molecule being evaluated. The equation below is a typical expression for the Raman scattering intensity [100].

$$I_R = I_0 \sigma_R C L k \qquad \text{(Equation 2.7)}$$

where I_R is the Raman scattering intensity, I_0 is the intensity of the incident light, σ_R is the Raman scattering cross-section of the molecule, L is the Raman system focal length, k is the instrument throughput, and C is the concentration of the molecular species.

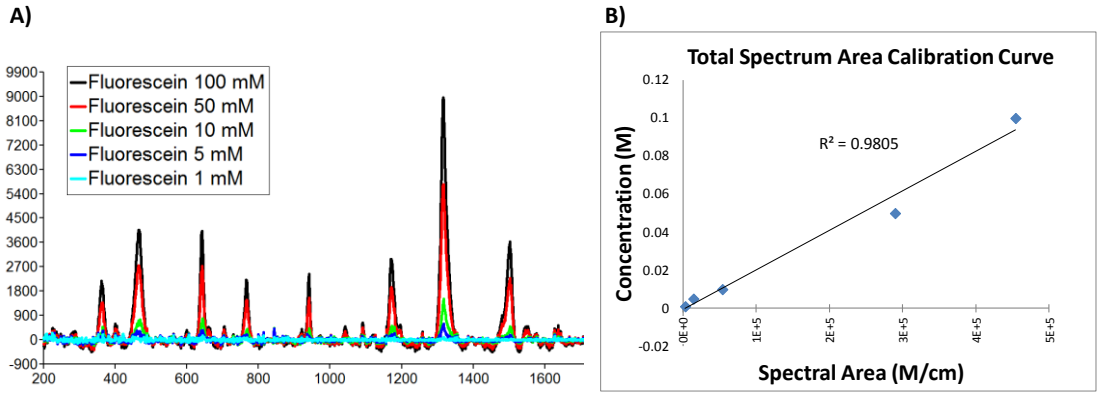

Figure 2.11 Spectral Calibration Curve and Raman System Sensitivity. The Raman spectrum of fluorescein at concentrations ranging from 1 - 100mM was detected and plotted in Figure 2.11A. The Raman band intensity is proportional to the concentration of the analyte and a calibration curve can be developed as shown in Figure 2.11B. Quantitative analysis using Raman spectroscopy is limited by the low sensitivity of the system.

Since the Raman scattering intensity is linearly proportional to the concentration, a trendline can be established for a specific Raman-active molecule. The terms for focal length (L), incident intensity (I_0), Raman cross-section (σ_R), and instrument throughput (k) must remain constant for this relationship to hold. When these factors remain constant, the Raman Spectrum can be used for quantitative chemical evaluation. Figure 2.11A and Figure 2.11B show the Raman spectrum of fluorescein (a Raman active dye), and a Raman spectral area calibration curve, respectively. From the graph, it can be seen that the lower detection limit of this particular system is approximately 1mM. These results highlight one of the problems associated with Raman spectroscopy. Since Raman scattering is rare, its sensitivity is very low and it is difficult to acquire the Raman spectra of chemicals in small concentrations. A common technique to increase system sensitivity is to increase the spectral acquisition time. A longer acquisition time will result in a greater likelihood that Raman-scattered photons will hit the detector. One disadvantage of increasing the acquisition time is that it also increases the susceptibility of the system to extraneous light sources and fluorescence.

Table 2.3 Typical Cross-Sections for Various Photonics Processes. The cross-section for scattering is typically much smaller than fluorescence and absorption. Surface-enhanced Raman scattering increases the scattering cross-section so that it is comparable to fluorescence and absorption, this greatly increases Raman spectroscopy sensitivity.

Photonics Process	Typical Cross-section (cm^2)	Reference
Absorption	**$1E^{-18}$-$1E^{-16}$**	[104]
Fluorescence	**$1E^{-18}$-$1E^{-16}$**	[105]
Surface-enhanced Raman Scattering	**1 E^{-17}-1 E^{-16}**	[106]
Rayleigh Scattering	**1 E^{-30}-1 E^{-27}**	[107]
Raman Scattering	**1 E^{-30}-1 E^{-25}**	[107]

Another option for increasing Raman scattering intensity is to increase the Raman scattering cross-section (σ_R). The cross-section is a calculated quantity, which expresses the likelihood of photon-to-particle interactions such as absorption, fluorescence, and scattering. The units of cross-section are in centimeters squared, because the cross-section expresses the hypothetical area available for particle interaction. Because the cross-section of Raman scattering is so small, it is challenging to make sensitive measurements using this technique. To increase the Raman scattering sensitivity, several techniques have been employed including stimulated Raman scattering [101], coherent anti-stokes Raman scattering [102], and surface-enhanced Raman scattering (SERS) [103]. SERS is of particular interest because the setup of the Raman system does not need to be altered for effective signal enhancement. Using SERS, the Raman scattering cross-section is enhanced to match the cross-section of fluorescence, which enables SERS to be used in applications requiring highly sensitive measurements. Table 2.3 shows the average cross-sections for several photonics processes.

2.4 Surface Enhanced Raman Spectroscopy

Surface-enhanced Raman spectroscopy (SERS) was discovered in 1974 by three scientists (Fleischmann, Hendra, and McQuillan) at Southampton University [108]. In their initial experiments, they discovered that the Raman spectrum of pyridine on a silver electrode showed an unusually strong Raman intensity [108]. Experimental investigation from multiple research groups showed that there are two underling mechanisms behind this Raman enhancement (chemical and the electromagnetic enhancement). Both mechanisms produce enhancement by causing a net change in the induced dipole moment. As stated previously in this chapter, the strength of the induced dipole moment for a Raman active molecule is given by $\mu_{\mathrm{ind}} = \alpha \mathrm{E}$, where α is the molecular polarizabity and E is the electric field strength. The first enhancement

mechanism is electromagnetic enhancement and results from a change in the electric field strength E. Electromagnetic enhancement is the dominant effect and occurs due to the enhancement of the electromagnetic field near the molecule of interest. This electromagnetic enhancement is caused by the interaction between the electromagnetic field and a nearby metallic substrate. The second form of enhancement is referred to as chemical enhancement and is a result of a change in polarizability (α) induced by charge transfer and bond formation between the metallic substrate and the molecule of interest [109].

2.4.1 Surface Plasmon Resonance

To understand these two mechanisms of SERS, it is important to first discuss the interaction of light with metallic surfaces. As incident light hits a metal surface, free electrons in the conduction band begin to oscillate [110]. As the electrons oscillate the bulk electron charge is redistributed across the surface, and an electronic dipole is produced in the metallic lattice [110]. This surface electron oscillation has discrete energy levels referred to as plasmons. When the incident light frequency matches the plasmon oscillation frequency, a resonance state is achieved, referred to as surface plasmon resonance (SPR). At this resonance state, the magnitude of the surface plasmons is maximized and incoming light intensity is amplified and remitted. When the dimensions of the metallic structure are less than the wavelength of incident light, the SPR is highly dependent on the geometry, size, proximity, and composition of the nanostructures [111]. When plasmon excitation occurs at the nanoscale, the electron density of the entire structure will oscillate (Figure 2.12). This overall surface electron oscillation is referred to as localized surface plasmon resonance (LSPR). LSPR results in an amplified electrical field near the particle surface and increased light scattering and absorption [112].

LSPR can be used to explain the size-dependent light scattering and absorption properties of gold and silver nanoparticles. By changing just the size of the nanoparticle, the LSPR peak position can be shifted dramatically, which will affect the observed color of the particle and the Raman scattering properties of these metallic nanoparticles. The LSPR peak position is the wavelength at which maximum absorption and scattering are observed for metallic nanoparticles. Greater electromagnetic enhancement and light scattering will occur when the excitation wavelength is near the LSPR peak. It is important to optimize SERS particles for a specific excitation wavelength. This optimization can be done by designing nanoparticles with dimensions that produce an LSPR peak at the excitation wavelength.

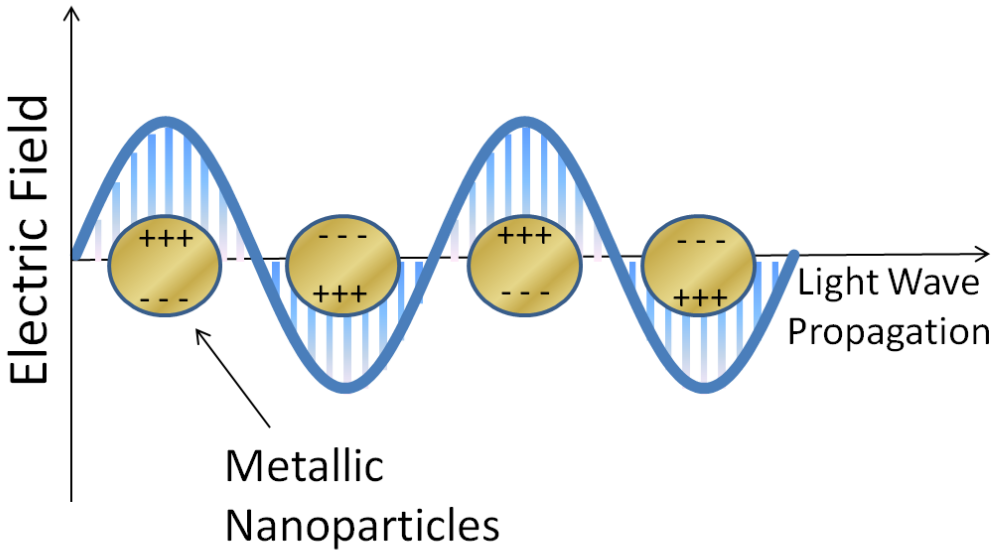

Figure 2.12: Localized Surface Plasmon Resonance. Localized Surface Plasmon Resonance (LSPR) is produced when electromagnetic radiation interacts with metallic nanoparticles. As light interacts with these particles, it creates electric dipoles on the particle surface, which oscillate back and forth in response to the incoming waves. Because the size of these structures is smaller than the wavelength of light, these oscillating surface plasmons dominate the electromagnetic response, producing increased light scattering and a greatly enhanced electric field near the particle surface.

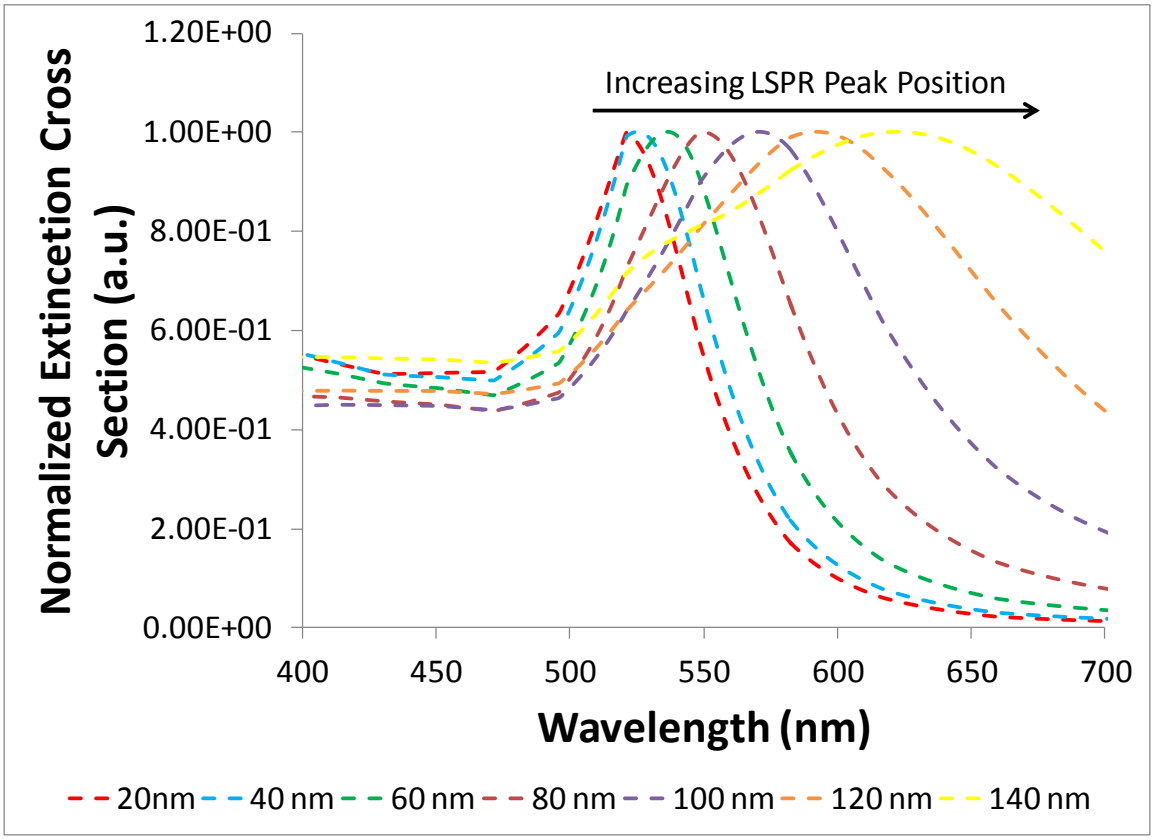

Figure 2.13 LSPR and Nanoparticle Extinction Cross-Section. Theoretically predicted normalized extinction cross-section of gold nanoparticles ranging from 20nm – 140nm were generated using Mie theory calculations. This plot shows the increasing SPR peak location as particle size increases. Data for this plot was generated using the program MiePlot [113][114].

Theoretical predictions of the LSPR peak location can be performed using Mie Scattering theory. Mie scattering theory is a method for applying Maxwell's equations for electromagnetic propagation to homogenous isotropic spherical particles [114]. The result of this application can be used to predict LSPR peak locations for various nanoparticle sizes, shapes, and dielectric properties. The following equation is derived using Mie scattering theory and can be used to estimate the wavelength dependent extinction properties of a nanoparticle that is electrostatically dipole-limited [115, 116].

$$E(\lambda) = \frac{24\pi N_a a^3 {\varepsilon_m}^{3/2}}{\lambda \ln(10)} \left[\frac{\varepsilon_i}{(\varepsilon_r + X\varepsilon_m)^2 + {\varepsilon_i}^2}\right] \quad \text{(Equation 2.8)}$$

In this equation $E(\lambda)$ represents the wavelength dependent light extinction, which is a sum of absorption and scattering. N_a is the area density of the nanoparticles, a is the radius of the nanoparticles, ε_m is the dielectric constant of the medium surrounding the nanoparticle, ε_r and ε_i are the real and imaginary portions of the nanoparticles dielectric function, and X is the particle shape factor. The particle shape factor X can be adjusted for Mie Theory simulations of particles with varying aspect ratios and shapes [115, 116]. Figure 2.13 shows the theoretical extinction spectrum of spherical gold nanoparticles of increasing sizes.

2.4.2 SERS-Based Biosensor Applications

SERS biosensors can be fabricated on planar substrates or can be created using nanoparticles in solution. When fabricated on a substrate, these biosensors are referred to as SERS substrates, while the use of nanoparticles for SERS enhancement has been termed nanoparticle SERS. Both methods have been used for a variety of biosensing applications including unknown chemical identification [117], bacterial [118] and viral [119] sensing, cancer detection [120], and tissue characterization [121].

2.4.2.1 SERS Substrates

SERS substrates are composed of a planar surface with metallic (usually gold or silver) nanoscale features. These metallic features produce enormous electric field enhancement and thereby cause increased light scattering. SERS substrates are useful for the analysis of chemical unknowns [122], trace level detection of contaminants [123], authentication [124], and in studies of biomolecular structure and function [125, 126]. When developing SERS substrates a

compromise must be made between high sensitivity and repeatability. This effect is due to the "SERS uncertainty principle" [127, 128] which states that high signal enhancement is the result of electromagnetic hot spots, which form at junctions between adjacent nanostructures. Hot spot formation is difficult to control, visualize, and predict, and as a result, repeatability suffers. The size, shape, density, and composition of the metallic nanostructures on the substrate surface will determine the enhancement effect and the optimal excitation wavelength. Often SERS substrates must be constructed for a specific excitation wavelength, but there are also broad range SERS substrates that can be used with a variety of wavelengths [129]. Some disadvantages of SERS substrates are that they are rarely selective [130], are susceptible to molecular interference [131], and are designed for single use applications [132]. One promising advantage of SERS substrates is that they can be constructed easily and are inexpensive [117, 133, 134].

2.4.2.2 Nanoparticle-Based SERS

Nanoparticle-based SERS is a highly flexible method for the development of SERS-based biosensors. In nanoparticle-based SERS, molecules of interest are bound to the nanoparticle surface and Raman measurements are acquired. Nanoparticle-based SERS measurements can be either intrinsic or extrinsic. Intrinsic SERS refers to the direct measurement of a target molecule. In this configuration, the molecules specific Raman signature can be observed. In extrinsic SERS, the presence of a molecule is detected indirectly using Raman reporter molecules that are bound to the nanoparticle surface. After addition of the Raman reporter molecule, the particle is functionalized with a protective coating and then antibodies, or other affinity ligands, are conjugated to the surface. An advantage of extrinsic SERS particles is that they can be extremely robust, allowing targeted detection in environments of high ionic strength and extreme pH.

Additionally, extrinsic SERS particles can be coated with biocompatible materials for use *in vivo* [21]. Although extrinsic SERS nanoparticles cannot be used to detect the unique spectral signature of their target molecule, they can be used as a very sensitive method for indirect detection. Figure 2.14 shows an illustration of intrinsic and extrinsic SERS nanoparticles, and the advantages and disadvantages associated with each method.

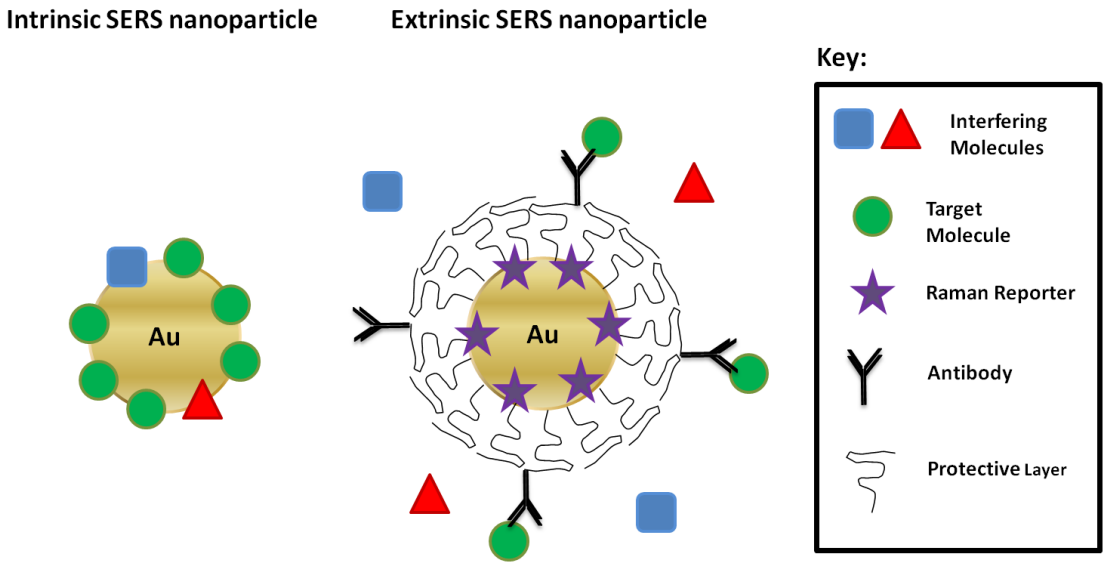

Advantages
- Direct sensing of target
- Raman signature of target
- Simple and inexpensive

Disadvantages
- Molecular Interference
- Potentially weak Raman signal
- Susceptible to aggregation

Advantages
- Robust and repeatable signal
- Not susceptible to molecular interference
- Not susceptible to aggregation
- Strong consistent Raman enhancement

Disadvantages
- Raman signature of target not observed
- More difficult to synthesis

Figure 2.14 Intrinsic and Extrinsic SERS Nanoparticles. A comparison of intrinsic and extrinsic SERS nanoparticles with the advantages and disadvantages of each method listed.

2.5 Conclusion

This chapter has focused on the theoretical aspects of SERS and its application to the detection and targeting of B-cell malignancies. Initially, the pathology of B-cell malignancies and immunophenotyping methods used to detect different B-cell malignancies were presented. The need for a sensitive multiplexing platform for B-cell malignancy classification was also discussed. Due to their large multiplexing capacity and their robust signal, Extrinsic SERS nanoparticles (or SERS probes), are an appropriate platform for the targeting of multiple biomarkers, and could be used to fill this clinical need.

Traditional methods such as fluorescence and chemiluminescent cannot be used for the simultaneous quantification of a large number of biomarkers because of their large spectral width. To provide increased detection and multiplexing capabilities, SERS probes with spectrally unique reporter molecules can be used. When excited with a light source, these probes produce inelastic light scattering, which can be detected using Raman spectroscopy. This chapter has discussed the classical and quantum mechanics theories of light scattering and how these theoretical concepts may affect the way in which SERS probes are fabricated and analyzed. Practical considerations associated with Raman spectroscopy where also discussed to provide context for experimental considerations presented in subsequent chapters of this thesis.

Finally, this chapter has discussed the details of SERS enhancement and the effects of localized surface plasmon resonance on metallic nanoparticles. The inelastic light scattering signal from SERS probe nanoparticles is enhanced through the plasmonic properties of the gold nanoparticle core. By taking advantage of the electromagnetic and chemical enhancement provided by localized surface plasmon resonance, extremely sensitive multiplex detection can

be achieved. This type of sensitive multiplex detection has potential for use in the quantification, classification, and treatment of B-cell malignancies.

CHAPTER 3

CHARACTERIZATION OF COMMERCIAL RAMAN SYSTEMS

3.1 Introduction

When developing chemical biosensors based on SERS, it is important to select a Raman system that will promote highly sensitive chemical detection and accurate chemical recognition. To make the appropriate selection, the specifications of the Raman system must be carefully evaluated and multiple factors must be compared. For bulk chemical evaluation, a simple bench top Raman system will be a cheap and yet effective choice. Bench top Raman systems can only be used for samples that have relatively large dimensions and are homogeneous. If non-uniform samples are evaluated using a bench top system, the Raman intensities will vary significantly across the sample field, and measurement repeatability will decrease.

A Raman microscope system is required when working with non-uniform sample fields where the ability to focus on a single object is important. Raman microscope systems are also critical for the development of Raman point mapping applications. Raman microscope systems will be more expensive than bench top units, but will also provide greater flexibility and higher resolution. The choice of a Raman system will be one factor that determines the sensitivity of SERS-based biosensors and should be carefully evaluated.

In this chapter, the selection of a Raman microscope system is discussed. Initially, several commercial Raman instruments were evaluated and a variety of experiments were conducted. These initial experiments proved to be valuable for the future development of SERS probes and provided a knowledge base for the development of a custom Raman microscope system. After the evaluation of these various systems, the decision was made to purchase a

commercial Raman microscope system and to build a custom Raman microscope system, which could be used for experiments requiring greater flexibility.

3.2 Factors to Consider when Selecting a Raman System

There are many different Raman systems currently on the market and comparison of the systems takes considerable effort and knowledge. To make an accurate comparison, the following factors should be considered: excitation wavelength (Section 3.2.1), spectral resolution (Section 3.2.2), spectral range (Section 3.2.3), and system sensitivity (Section 3.2.4). When using a Raman microscope for point mapping applications, additional specifications must be considered, such as laser spot size [135], spatial resolution [136], acquisition time per spectrum [137], and sample temperature control [138].To facilitate a discussion of the factors that must be considered when selecting a Raman system, first a brief description of the design of a Raman system will be presented.

In Raman spectroscopy, laser light is focused onto the sample and light scattering occurs. This scattered light is collected, often using the same optics to both focus the incident light and collect the scattered light. The collected light is predominantly Rayleigh scattered light, but a small portion is Raman scattered light. To visualize the weak Raman signal the Rayleigh component is filtered using a long-pass dichroic mirror. The dichroic mirror transmits the Raman component, while reflecting the Rayleigh component. The Raman component is then focused onto the spectrometer entrance slit. Once the light has entered the spectrometer, it hits the diffraction grating and is dispersed. Finally, the dispersed light is directed towards the CCD detector and can be visualized. Figure 3.1 illustrates a simplified Raman setup.

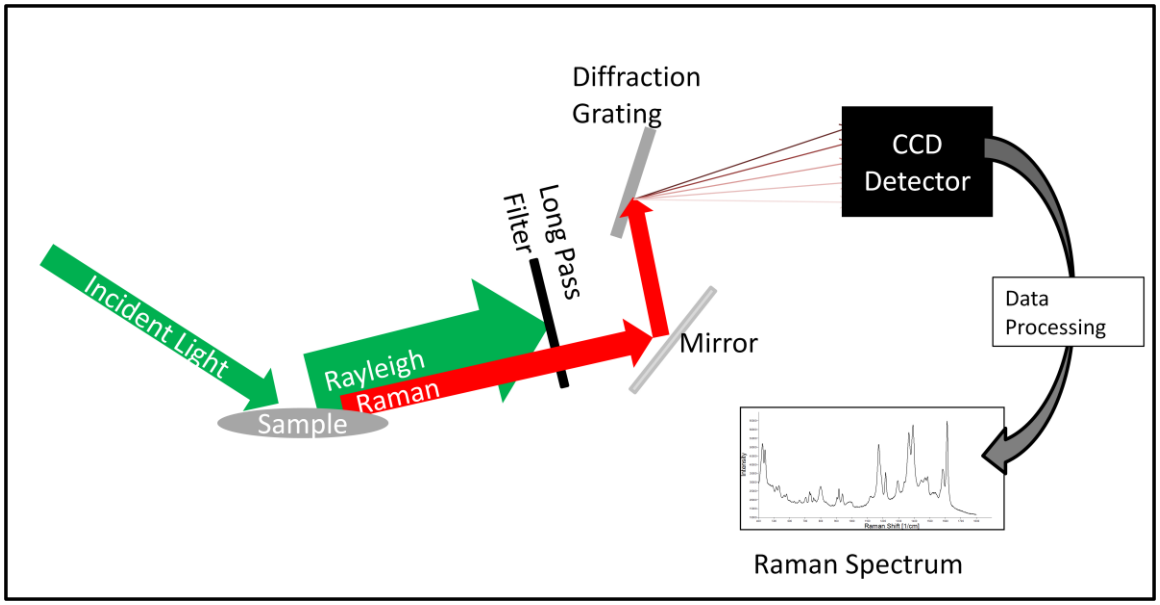

Figure 3.1: Raman System Schematic. A diagram of the basic components of a Raman system, including a long-pass filter, diffraction grating, and detector.

The long-pass dichroic mirror is critical in Raman system design, since the Rayleigh scattering component will typically be six to eight orders of magnitude greater than the Raman component [91]. If Rayleigh scattering is not filtered out, the resulting Raman component will be overshadowed by strong Rayleigh scattering, making observation of the Raman signal difficult. Additionally, the strong Rayleigh component can saturate the sensitive detector and potentially cause overexposure and detector damage. Another critical component is the diffraction grating, which uses nanoscale reflective features to produce diffraction of the incoming light waves. This diffraction pattern is imaged by the detector. The diffraction grating is designed to have optimal efficiency within a particular wavelength range. As a result, the grating efficiency and excitation wavelength must be matched for the best signal enhancement.

3.2.1 Excitation Wavelength

A Raman system is designed to maximize the collection of scattered light. To detect the weak Raman scattering phenomenon, a laser source is used to excite the sample. The required laser power depends on the scatter efficiency of the laser (I_s) expressed as:

$$I_s = I_0 \frac{8\pi\alpha^2 N}{\lambda^4 R^2} \sin^2(\theta) \qquad \text{(Equation 3.1)}$$

where I_0 is the incident light intensity, α is the polarizbility of the molecular scatters, N is the number of scatters, R is the distance between the scatters and the observer, θ is the scattering angle, and λ is the wavelength of the incident light [88]. The wavelength of the excitation light is of particular importance, as its contribution to the intensity is significant. Shorter wavelengths are more efficient at scattering, and require less power for Raman scattering measurements than do lasers with longer wavelengths. The graph below shows the wavelength dependent scattering relationship. As shown in Figure 3.2, the scattering intensity is proportional to 1/ λ^4, making the wavelength contribution to scattering its most significant factor.

There are additional factors to consider when selecting a laser wavelength, such as sample autofluorescence and laser penetration depth. Both of these factors can influence sample measurements, especially when working with biological samples. NIR lasers will experience reduced autofluorescence and increased sample penetration. Additionally, the laser wavelength will influence the spatial resolution of the Raman system, because the diffraction limited beam diameter of a focused laser beam will be directly related to the wavelength of the excitation source. These factors are especially important for Raman microscope applications and point mapping, where a small laser spot size and high spatial resolution are required for site-specific Raman detection.

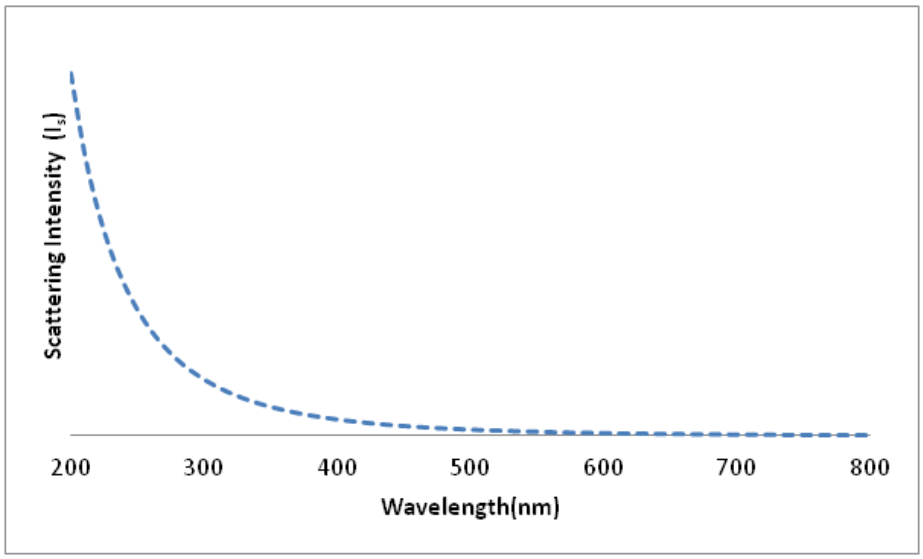

Figure 3.2: Wavelength Dependence of Light Scattering. The light scattering intensity is dependent on the wavelength of the incident light. Higher scattering intensity will be experienced with higher energy light sources [88].

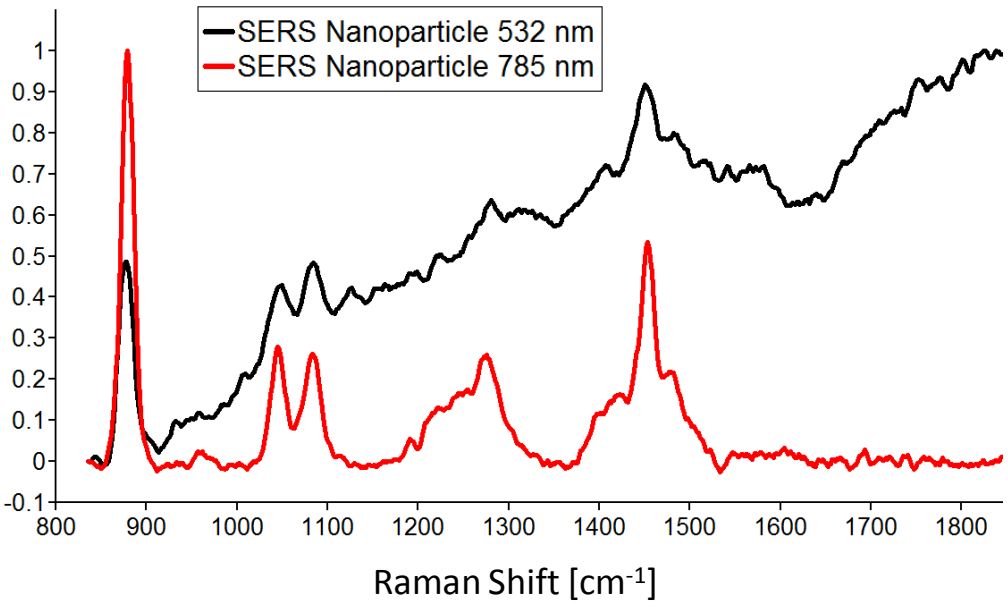

Figure 3.3 Fluorescence Baseline and Excitation Wavelength. The optical response of SERS probe nanoparticles labeled with 4-aminothiolphenol (4-ATP) were evaluated with two different excitation sources (532nm and 785nm). The spectrum acquired at 532nm shows an increasing fluorescence baseline while the spectrum acquired with 785 nm excitation shows very little fluorescence.

When acquiring Raman spectra of cells and tissues, NIR lasers are typically used for sample excitation. NIR lasers are favored because sample auto-fluorescence occurs more readily when visible light is used to excite the sample. Fluorescence is an electron absorption process that competes with Raman scattering. As a result, increased Raman scattering will typically occur when NIR excitation is used because fluorescence is decreased. Figure 3.3 illustrates the decrease in Raman scattering intensity that occurs due to fluorescence. This figure shows the Raman spectrum of SERS probe nanoparticles acquired at both 785 and 532 nm excitation. The spectrum acquired with 532 nm excitation shows significant fluorescence as seen by the steadily increasing baseline, while the spectrum acquired at 785 nm shows a much smaller fluorescence baseline and increased Raman scattering. In some cases, the effects of fluorescence can also be reduced using SERS. SERS substrates and nanoparticles often produce the highest enhancement at specific excitation wavelengths. This effect can be used to overcome the diminished Raman scattering caused by fluorescence.

3.2.2 Spectral Resolution

The spectral resolution of a Raman system defines the minimum distance between two Raman peaks at which those peaks can both be distinctly observed. Systems with high spectral resolution can distinguish Raman peaks that are very close together. This ability is important for Raman studies involving hydrogen bonding [139], protein folding [140], molecular polymorphism [141], stress and strain measurements [142], and shock-induced structural and chemical changes [143, 144]. Figure 3.4 shows the spectrum of polystyrene acquired with different spectrometer slit widths (A 2000µm, B 1500µm, C 1000µm, D 500µm, and E 50µm slit width). The spectral resolution is directly related to the slit width. Notice that the two characteristic polystyrene peaks at 851nm and 854nm are no longer differentiable once the slit

width reaches 2000 µm. Other factors that influence the spectral resolution include the spectrometer focal length, the grating groove density, the laser wavelength, and the detector pixel size.

3.2.3 Spectral Range

Spectrometers with a high spectral resolution normally have a very small spectral range over which the Raman signal can be acquired. This is because a diffraction grating capable of high spectral resolution will disperse the light widely across the detector. When this occurs, only a small portion of the entire spectrum can be visualized at once. To obtain a Raman spectrum over a large range with a high spectral resolution grating, multiple spectra are acquired at different center wavelengths. The center wavelength is the wavelength that falls onto the center of the detector after grating dispersion. By sequentially adjusting the grating angle (and as a result the center wavelength), a large spectral range can be achieved with high spectral resolution.

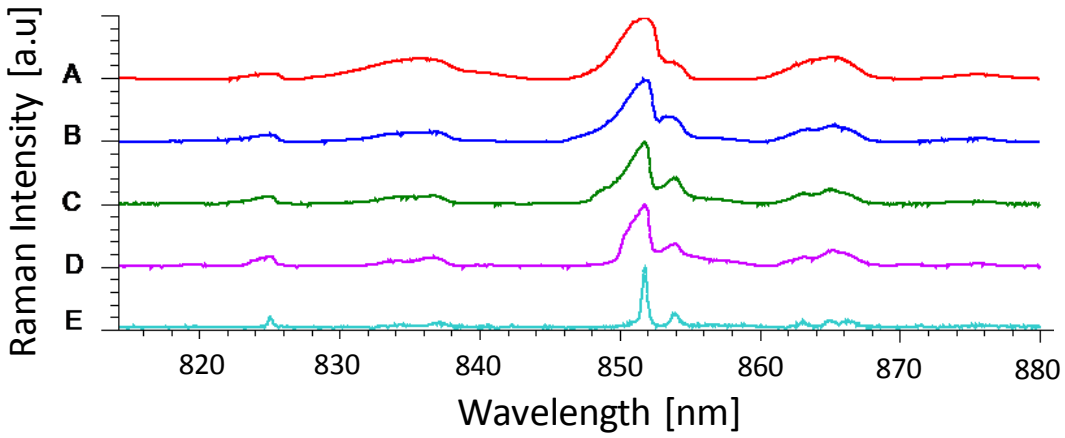

Figure 3.4 Spectral Resolution as a Function of Slit Width. The spectral resolution of a spectrometer is a function of the spectrometer slit width. Increased slit width results in decreased spectral resolution and inability to distinguish spectral peaks (A 2000µm, B 1500µm, C 1000µm, D 500µm, and E 50µm slit widths).

3.2.4 System Sensitivity

The system sensitivity is dependent on the spectral throughput of the spectrometer, the detector sensitivity, and the Raman activity of the specific molecule being evaluated. The spectral throughput of the system describes the number of photons that can pass through the system and hit the detector at a given exposure time. Figure 3.5 shows that as the spectrometer slit width increases the spectral throughput also increases. Note that while the exposure time remains the same, the total photon count increases and spectral resolution decreases with increasing slit width. Additionally, the spectral throughput depends on the quantum efficiency of the grating. The quantum efficiency describes the probability that an electron will be generated in response to an incident photon. The spectrometer gratings are designed to have optimal quantum efficiency at a specified wavelength, so a grating that has an optimal quantum efficiency in the range of interest should be selected [145].

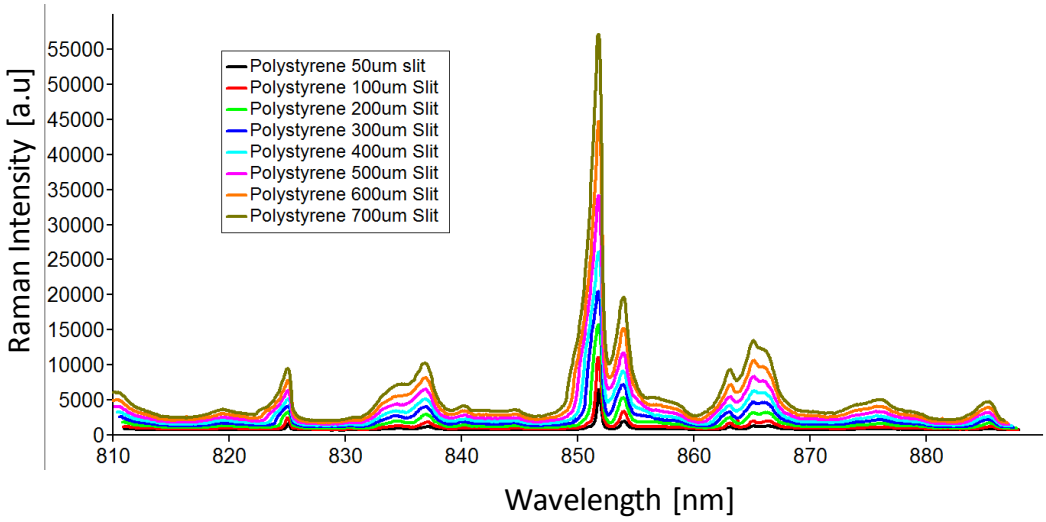

Figure 3.5 Spectral Throughput Increases With Increasing Spectrometer Slit Width. The increasing slit width will result in an increase in the spectral throughput of the system at the expense of spectral resolution.

The sensitivity of the detector is also an important parameter to consider. Detector sensitivity is determined by the detector quantum efficiency and the signal-to-noise ratio (SNR) [145]. Detector quantum efficiency is generally wavelength dependent so it is important to select a detector that is sensitive to the specific wavelength range of interest [145]. Additionally, the detector quantum efficiency can be improved by the addition of an anti-reflection coating on the detector surface [145]. Raman signals are often weak and can be difficult to distinguish from the background noise. To increase Raman system sensitivity it is also important to increase the SNR. The SNR can be improved by cooling the detector to remove dark noise caused by thermally generated current [146, 147].

The final parameter that determines system sensitivity is the Raman activity of the molecules being evaluated. For a molecule to be Raman active, it must have vibrational and rotation modes that cause a change in its molecular polarizability. Raman-active molecules experience a net change in the molecular polarizability in response to monochromatic excitation. This net change in molecular polarizability will result in vibrational activity of the molecule and in subsequent inelastic light scattering. Because the Raman intensity will vary for different molecules, it is best to determine how Raman-active a molecule is by testing its Raman response. To gauge the system sensitivity, a serial dilution of the Raman active molecule can be tested. An estimate of the lower detection limit of the system can be made by determining the lowest concentration of samples can be detected. This procedure can be done for molecules with no extra Raman enhancement or can be done using enhancement techniques such as SERS or resonance Raman. In the following paragraphs, initial experiments to determine system sensitivity for a variety of molecules with and without enhancement techniques are mentioned.

Table 3.1: Commercial Raman System Specifications. The Raman systems listed here were investigated to determine the most appropriate system for surface-enhanced Raman experiments. Note: Systems indicated with * were evaluated as demo units from the listed companies or samples were sent for evaluation.

Raman System	Producer	Laser Wavelength	Maximum Laser Power	Spectral Resolution (cm-1)	Spectral Range (cm-1)	Price	Notes
PeakSeeker Pro	Algitron	785 nm	300 mW	6	200-2000	$	Benchtop System
Advantage 785*	SciApps	785 nm	120 mW	3-5	100-2500	$	Benchtop System
Inspector 785*	SciApps	785 nm	300 mW	6-8	175-2875	$	Handheld System
Agility 785*	BaySpec	785 nm	450 mW	6-9	100-2300	$	Benchtop System
DXR Smart*	Thermofisher	780 nm	150 mW	3-5	50 - 3500	$$	Benchtop System
Examiner 785*	SciApps	785 nm	120 mW	5	200-2000	$$	Microscope System
Normadic 785*	BaySpec	785 nm	100 mW	4-5	100-3200	$$	Microscope System
inVia Raman Microscope*	Renishaw	785 nm	100 mW	0.5	100-3600	$$$	Microscope System
DXR Smart Microscope	Thermofisher	780 nm	150 mW	3-5	50 - 3500	$$$	Microscope System

3.3 Raman System Evaluation and Initial Experiments

In the process of comparing Raman sensitivity, several commercial Raman systems were evaluated. Each system was compared based on the factors mentioned above (fluorescence rejection, spectral resolution, spectral range, and sensitivity) and on practical factors such as the user interface, laser safety, and system flexibility. Table 3.1 shows a list of manufacturer specifications for several commercially available Raman systems that were investigated for this thesis.

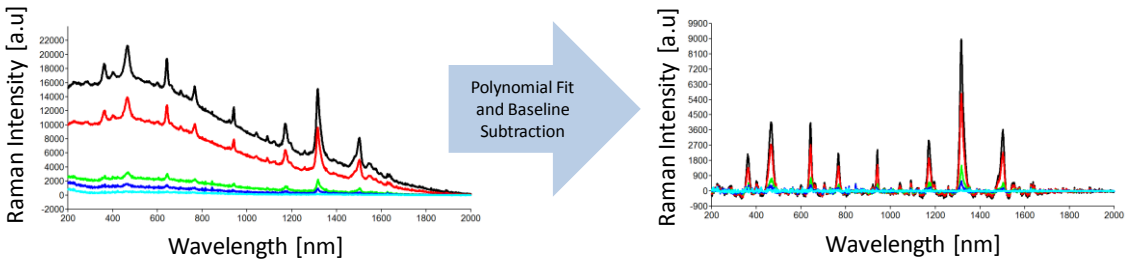

Figure 3.6 System Sensitivity and Fluorescence Baseline Subtraction. The intensities of fluorescein Raman peaks were compared after baseline subtraction to determine Raman system sensitivity.

3.3.1 System Sensitivity and Fluorescence Rejection

As a measure of system sensitivity and fluorescence rejection, fluorescein, a molecular chromophore, was evaluated on several of the systems presented above. Dyes such as fluorescein are often used in SERS due to their ability to produce strong resonance enhancement. Resonance Raman enhancement occurs when the electronic transition of the chromophore matches the excitation wavelength producing excited state scattering. Fluorescein was also chosen because of its tendency to produce fluorescence during excitation. It is advantageous to determine how effective the system is at fluorescence rejection by comparing the peak heights and fluorescent background produced by each system. Figure 3.6 shows sensitivity measurements acquired with the SciApps Advantage^{TM} Raman spectrometer. The results show that the fluorescence background and Raman peak heights are proportional to the concentration of the dye. After acquisition of the spectrum, the fluorescent baseline was removed using a polynomial fit and subtraction algorithm so that peak highs could be compared.

A similar procedure was repeated for each of the systems that were evaluated and a lower detection limit was determined for each system. The lower detection limit for the systems ranged from 1mM to 100uM. Each system showed strong fluorescence and baseline subtraction was required in the data processing of the resulting spectra.

3.3.2 SERS Substrate Fabrication and Enhancement Effect

To evaluate the response of each system to SERS conditions, silver SERS substrates were fabricated through galvanic displacement of silver nitrate onto copper. The SERS substrates showed significant signal enhancement and fluorescence rejection. The procedure for development of these substrates is an adaptation from the paper by Nie and Fang written in 2002 [148].

The following materials were used for the development of these SERS substrates: silver nitrate 99.9% (Alfa Aesar), copper(II) nitrate trihydrate 99.9% (Acros Organics), sulfuric acid, and 5 mil copper foil samples (Storm Copper Components). Copper foil samples were cut into 1x1 cm squares and dipped in 1M sulfuric acid to chemically clean the surface. The samples were then rinsed with DI water and dried with N_2 gas. The samples were baked for 2 hours at 80˚C to create a uniform oxide layer on the surface and were stored in a desiccator until use. A solution of 0.1M silver nitrate with trace copper ions ($6x10^{-4}$ M) was created in DI water. After mixing, the solution was applied to the copper surface and a reaction occurred for 60 seconds. During the course of the reaction, a thin silver film formed on the copper surface. This film was removed by washing the substrate in DI water followed by drying with N_2 gas. At this point, the substrates were either used immediately or stored in a desiccator for future use. Figure 3.7 shows the copper substrate surface before and after galvanic displacement.

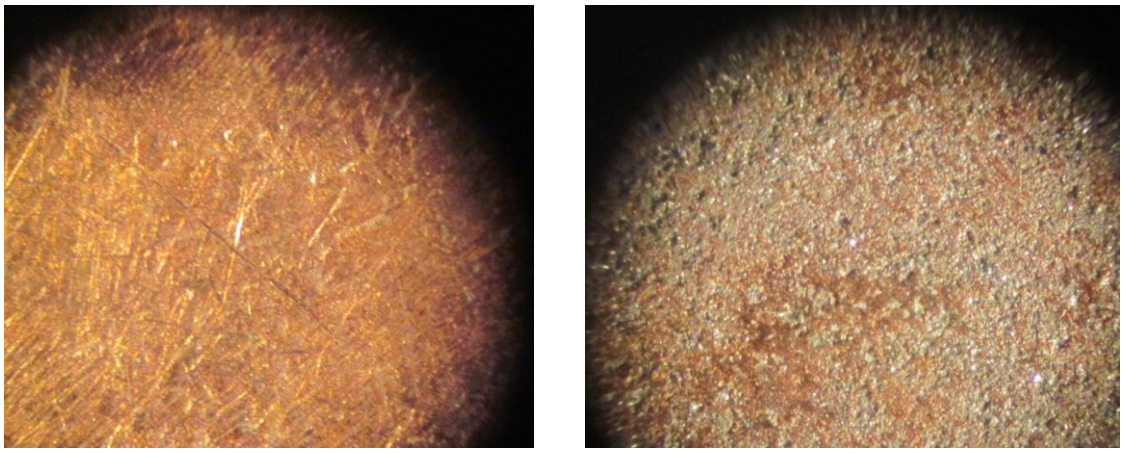

Figure 3.7 Silver Nitrate SERS Substrates Created by Galvanic Displacement. Using galvanic displacement silver nitrate SERS substrates were created and used to study the SERS spectrum of reporter molecules on their surface.

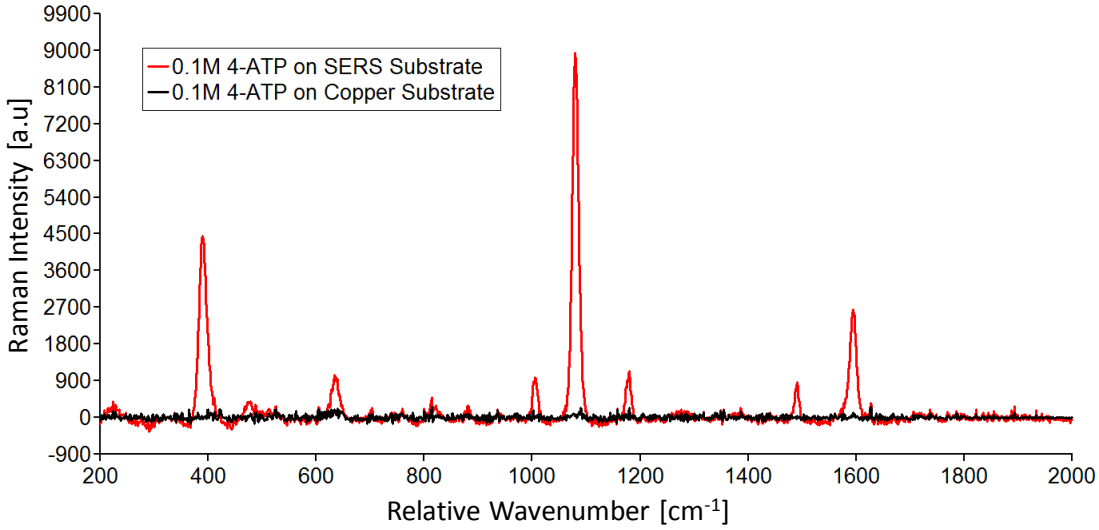

Figure 3.8 Raman Spectrum of 4-ATP on a Silver Nitrate SERS substrate. Significant Raman signal enhancement was demonstrated using the fabricated silver nitrate SERS substrates. A reporter molecule, 4-ATP, was added to the substrate surface and Raman measurements were acquired with one second acquisition time.

The reporter molecule, 4-aminothiolphenol (4-ATP), was applied to the substrate surface at a concentration of 0.1M, and the Raman spectrum was acquired with one-second acquisition time and ten accumulations. As a control, the Raman spectrum of 0.1M 4-ATP on a plain copper substrate was acquired. The resulting spectra shown in Figure 3.8 illustrate the significant enhancement that can occur when using SERS. The silver nitrate SERS substrates produced greatly increased Raman signal enhancement and very little fluorescence.

3.3.3 Multiplexing with Raman Spectroscopy

Another important parameter that was evaluated using the Raman systems mentioned above was multiplexing capacity. The ability to quantify multiple chemicals at the same time (multiplexing) is a significant benefit of Raman spectroscopy. When a Raman spectrum of a mixture of chemicals is acquired, it will be a composite spectrum with Raman peaks from the different constituents of the mixture. The intensity of peaks in the composite spectrum is

dependent on the concentration and Raman activity of each constituent. A composite Raman spectrum will ideally be a linear combination of its parts. As a result, a composite spectrum can be separated using a technique referred to as classical least-square deconvolution [149, 150]. Classical least-square deconvolution is a spectral unmixing algorithm that uses a known Raman spectrum of several pure substances to unmix a composite spectrum. Alternatively, if reporter molecules are chosen so that there are no overlapping peaks, then each reporter can be identified by its peak with the largest intensity. This method reduces the complexity of spectral unmixing and is resistant to problems associated with mathematical methods such a classical least-squares deconvolution which tend to amplify system noise [151].

To evaluate the multiplexing potential of each Raman system, a series of miscible solvents were used. The Raman spectra of these solvents were acquired both alone and in mixtures. After the Raman spectra were acquired, the individual components of a composite spectrum were identified and the relative concentration of each component was compared. Figure 3.9A shows a multiplex analysis of ethanol (EtOH), methanol (MeOH), and isopropyl alcohol (IPA). When compared to the emission peak of fluorescence (Figure 3.9B), the Raman peaks associated with the vibrational modes of EtOH, MeOH, and IPA are much narrower (Figure 3.9A). The narrow Raman scattering peaks can be used for the concurrent analysis of multiple compounds without spectral overlap. These results illustrate the multiplexing advantage of Raman spectroscopy. Within a range of 800 cm^{-1} to 1100 cm^{-1} (equivalent to 837.6 nm to 859.2 nm), three different molecules were detected simultaneously. Such multiplexing capabilities would not be possible using fluorescence, since the spectral profile of a fluorescent molecule, such as the fluorescent antibody AlexaFluor 790 shown above, is much wider than the Raman peaks.

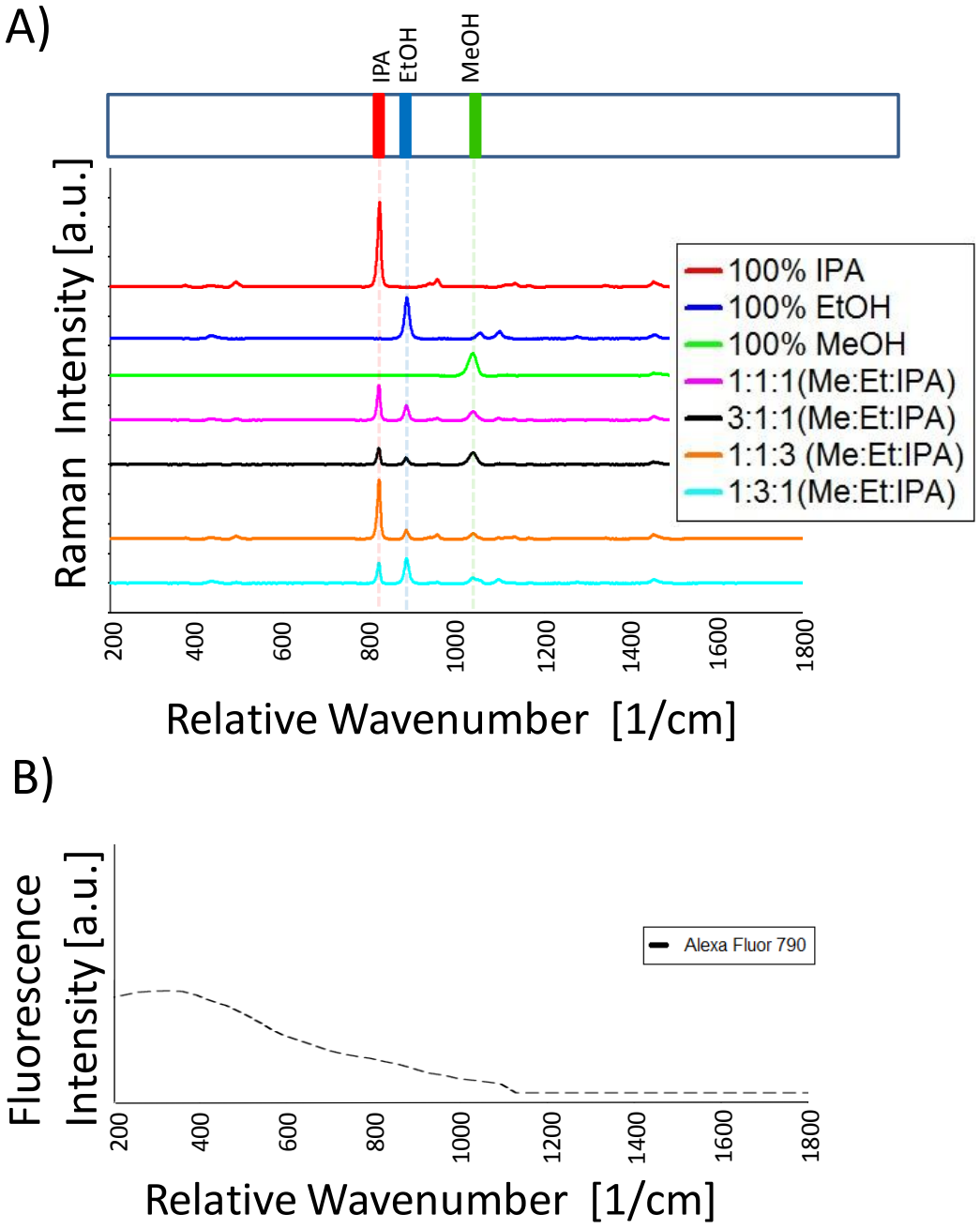

Figure 3.9 Demonstration of Raman Multiplexing Capacity. The multiplexing capacity of Raman spectroscopy was demonstrated with mixtures of three separate solvents, ethanol, methanol, and isopropyl alcohol (A). Raman peaks seen in these mixtures are significantly narrower than Alexafluor 790, a near infrared fluorescent dye (B).

3.4 Conclusion

Several Raman system were compared based on excitation wavelength (Section 3.2.1), spectral resolution (Section 3.2.2), spectral range (Section 3.2.3), and system sensitivity (Section 3.2.4). Using these Raman systems, initial experiments with SERS, and Raman-based multiplexing were conducted. It was decided that two Raman microscope systems would be needed for the work in our lab, see Figure 3.10. After comparison of commercial Raman systems, it was determined that the Renishaw inVia Raman microscope system would provide the best results and would fit a variety of research needs in the lab, see Figure 3.10A. The decision was also made to construct a custom Raman microscope system, see Figure 3.10B. This decision was made based on the expected need for customization in future lab projects. Additionally, this approach resulted in significant cost savings and enabled the lab to obtain two separate Raman microscope systems. The first system was a 633nm Renishaw InVia Raman microscope and the second system was a custom designed Raman microscope system with 785nm excitation. The design of this custom system will be discussed in the next chapter.

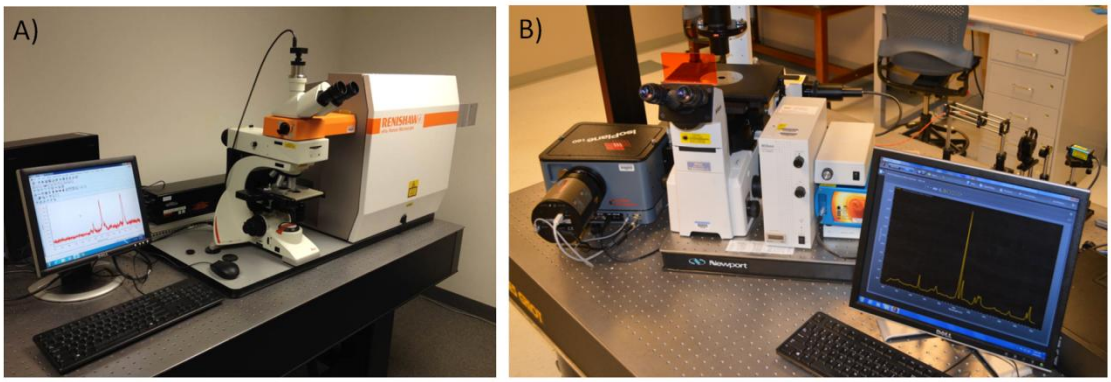

Figure 3.10 Two Separate Raman Microscope Systems. After evaluation of several Raman microscope system the decision was made to purchase a Renishaw inVia Raman microscope system (Figure 3.10A). In addition, a custom Raman microscope system was designed and built, and will be discussed in chapter 4 (Figure 3.10B).

CHAPTER 4

DESIGN OF A NEAR-INFRARED RAMAN MICROSCOPE SYSTEM

4.1 Introduction

As an alternative to purchasing a commercial Raman instrument, a cheap and effective choice was to design a custom system. There were several advantages to using a custom-built system including the ability to adjust the optics based on experimental need. If required, the system could be modified to incorporate different excitation wavelengths or a custom microfluidics flow cell for high-throughput applications. In addition, the custom instrument could be used for dual-modality imaging such as fluorescence or dark field in addition to its Raman spectroscopy function. Finally, because the custom system was designed using an inverted microscope base and extra-long working distance objective lenses, it could be used for imaging and Raman spectrum acquisition of cell culture flasks. To avoid cell and tissue autofluorescence, the Raman system was designed for NIR wavelength excitation. To optimize the system, the detector, grating, and filters were carefully chosen to match the excitation wavelength. The selection of a custom system provided added flexibility and proved to be a viable, low cost alternative to purchasing a commercial instrument.

The custom system was designed using a Nikon TE2000-S inverted microscope. The microscope was adapted by adding a fiber optic laser entry port, which was used to direct the 785 nm laser beam to the objective lens and scatter light off the sample. The scattered light was recollected through the objective lens and passed to the microscope system. Within the microscope system, scattered laser light was filtered to remove the Rayleigh scattering component. The remaining Raman scattered light was dispersed by the grating mirror found

within the spectrometer. Finally, the dispersed light was detected using a thermoelectrically cooled CCD detector. The final design provided a spectral resolution of 1.6 cm^{-1} and a spectral range of 300 - 3000 cm^{-1}, and is shown in Figure 4.1. This custom Raman system was used for the fabrication SERS probes for biomarker targeting and detection (Chapter 5).

4.2 System Components

There were four critical components in the design of this Raman microscope system. These components will be discussed in the following sections: Section 4.2.1 Laser System and Entry Port, Section 4.2.2 Microscope and Filters, Section 4.2.3 Spectrometer and Diffraction Grating, and Section 4.2.4 Detector Data Processing.

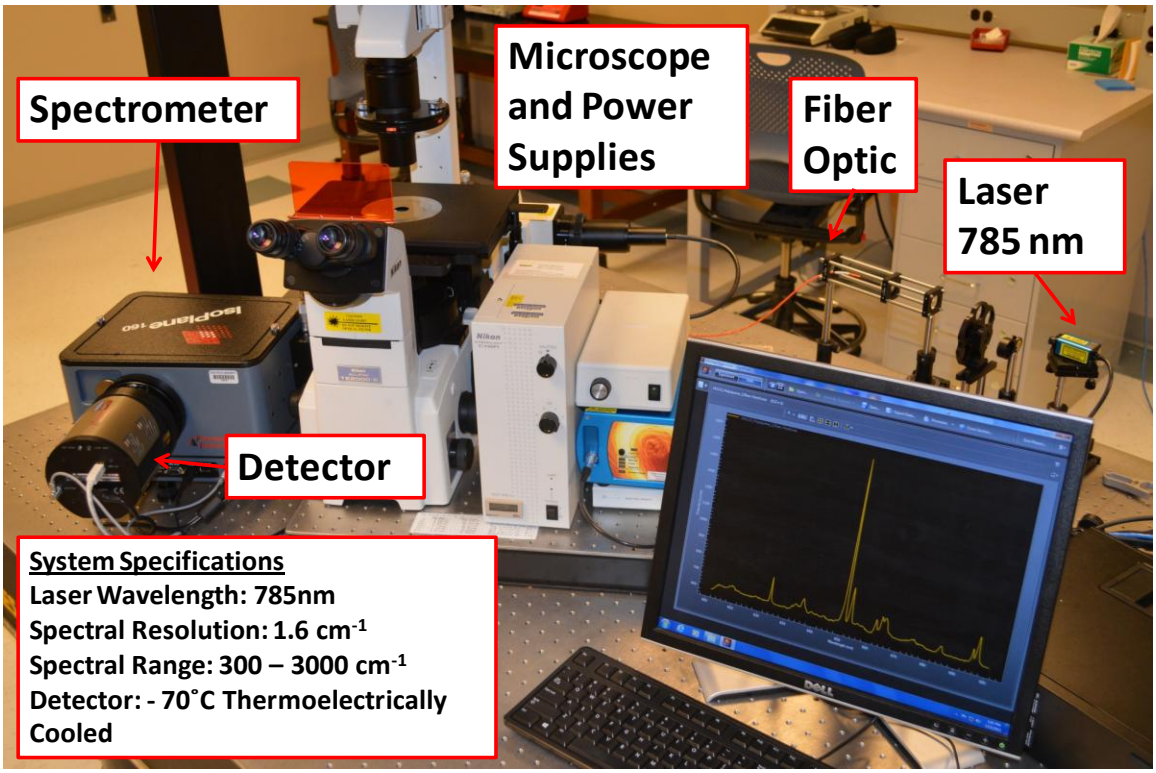

Figure 4.1: Custom 785nm Raman Microscope Setup. A custom Raman microscope was designed with a 785nm laser, an inverted microscope base, a spectrometer, and detector.

4.2.1 Laser System and Entry Port

A laser entry port was used to focus the laser onto the sample stage. To do this, a single mode 785nm laser with a beam diameter of 0.7mm and a beam divergence of 2mrad (Innovative Photonics Solutions) was coupled to a multimodal fiber optic cable (Thor Labs M74L01) with a numerical aperture of 0.39 and a core diameter of 400µm. The laser was focused onto the fiber optic cable using a plano-convex lens at a distance so that the focused beam diameter was smaller than the fiber core and the angle of entrance was less than the maximum acceptance angle of the fiber. This procedure increased the transmission efficiency because light was not lost through the fiber cladding or through destructive interference.

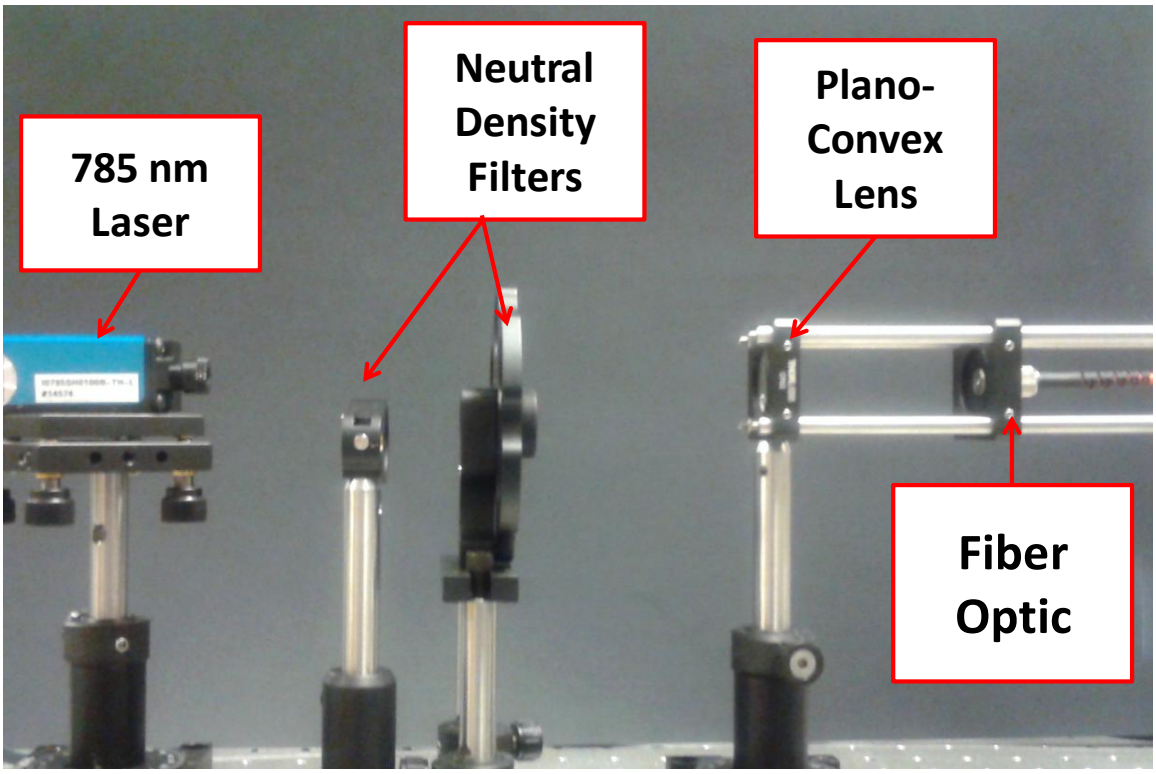

Figure 4.2 Focusing of the Laser onto a Fiber Optic Cable. Before laser light entered the microscope, through the laser entry port, it was first focused onto a fiber optic cable using a plano-convex lens.

A filter wheel, with neutral density filters ranging from optical densities of 1 to 6, was used to reduce the laser power for low power measurements, alignment, and to protect the sensitive CCD detector from damage. After the laser was focused onto the fiber optic (Figure 4.2), the light was transmitted into the microscope through the laser entry port. The laser entry port was positioned on the back of the microscope and was used to align and expand the laser beam for Raman spectroscopy. The laser entry port also has a secondary illumination path for a mercury lamp source used in fluorescence measurements. This dual function facilitates both Raman and fluorescence measurements for the same sample. Figure 4.3 shows the laser entry port positioned on the back of the microscope.

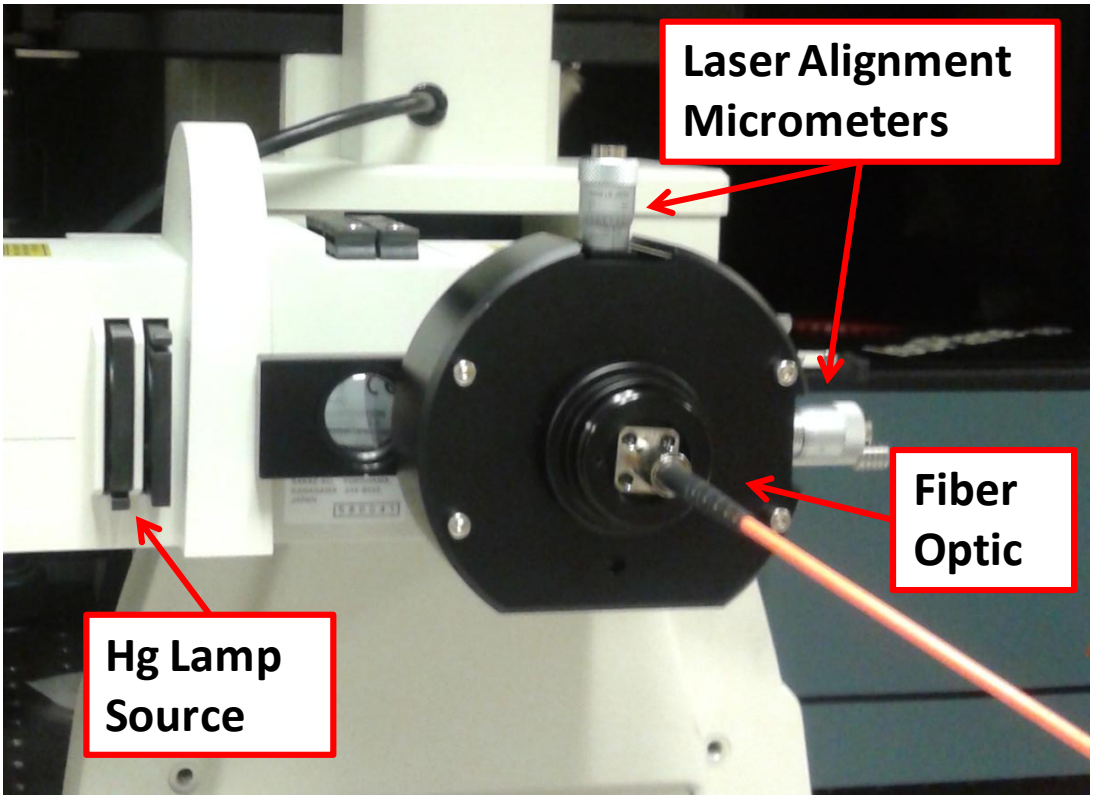

Figure 4.3 Laser Entry Port. The laser light was coupled to the microscope base using a laser entry port with an internal beam expander.

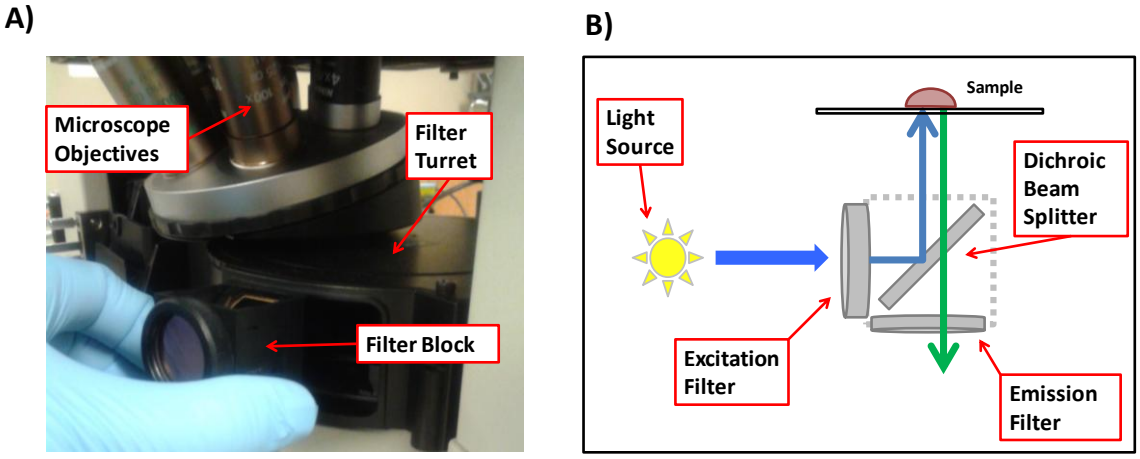

Figure 4.4 Filter Blocks and Microscope Filter Turret. Optical filter blocks housed the filters used for Raman spectroscopy. The blocks were placed in a filter turret (Figure 4.4A) so that they could be easily positioned in the optical path. The basic design of a filter block allows three filters to be used simultaneously (Figure 4.4B). The filter block image.

4.2.2 Microscope and Optical Filters

Once the laser beam enters the microscope through the laser entry port, it interacts with filters within the microscope filter turret. The filter turret is a rotatable tray on the microscope base that houses six different filter blocks. It can be rotated to place a new set of filters in the optical path. Each filter block can contain up to three different filters: an excitation filter, a dichroic beam splitter, and an emission filter [152]. The filter turret and filter blocks are illustrated in Figure 4.4A, and Figure 4.4B respectively.

To ensure that the sample is excited with monochromatic light at 785nm, the laser beam was first passed through a laser line filter (see A in Figure 4.5) which removed any resonance modes that are transmitted by the system and Raman scattering from the optical fiber [153]. After the laser line filter, the laser beam was transmitted to a long-pass dichroic mirror (see B in Figure 4.5). This mirror reflects light that is near the excitation wavelength and transmits light that is red-shifted from the excitation wavelength. Laser light was reflected off

the dichroic mirror and passed to the objective lens where it was focused on the sample. Light was scattered off the sample, and the scattered light was collected by the objective lens and transmitted to the dichroic mirror. The Rayleigh scattering component was reflected off the dichroic mirror, while the Raman component was transmitted through the dichroic mirror and imaged on the spectrometer entrance slit. To ensure that the Rayleigh component had been completely rejected, an additional long-pass filter was added to the base of the filter block. This filter, traditionally referred to as a Rayleigh filter (see C in Figure 4.5) removed any last traces of the Rayleigh component that was not eliminated by the dichroic mirror.

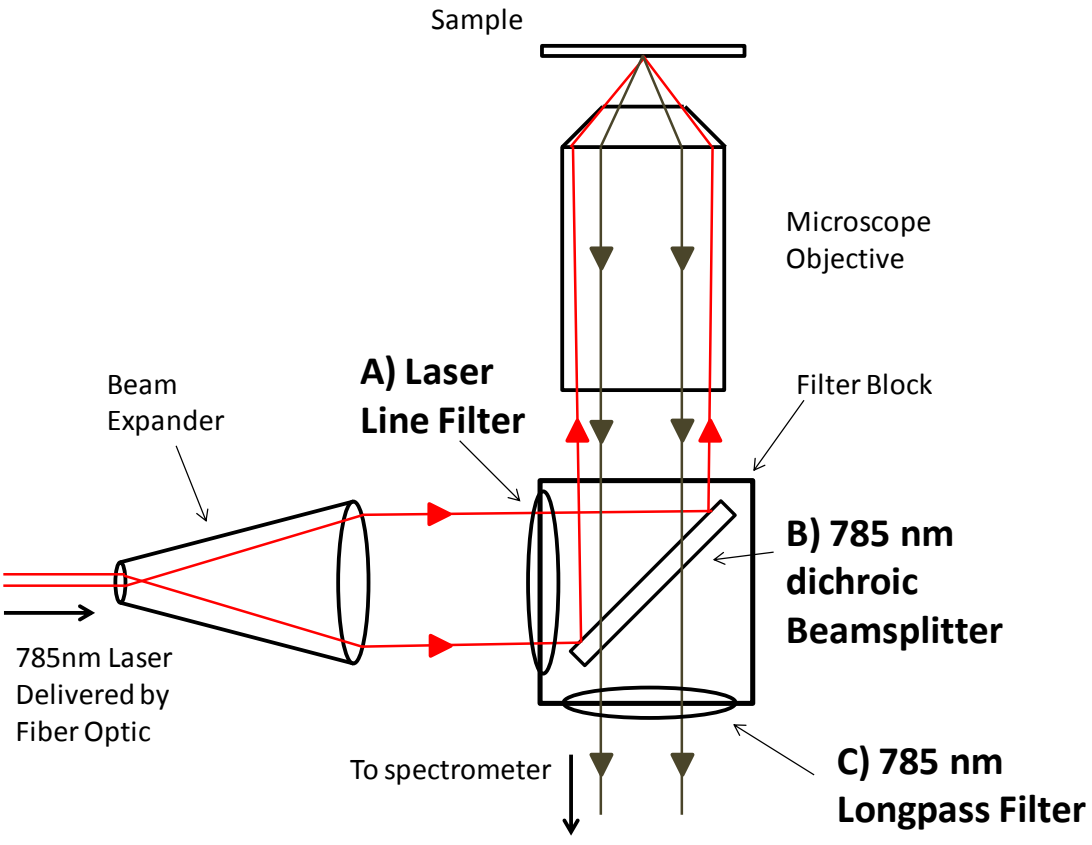

Figure 4.5 Optical Path and Raman Signal Filtering. Laser light is filtered using a series of optical elements housed in the filter block. These elements include (A) a laser line filter, (B) dichroic beamsplitter, (C) Rayleigh filter.

4.2.3 Spectrometer and Gratings

The spectrometer was attached to the microscope through a side port. As the scattered light exits the microscope, it was directed to the spectrometer entrance slit. The light then interacted with multiple mirrors within the spectrometer, including the diffraction grating. The diffraction grating is a nanopatterned mirror that is positioned on a motorized grating turret. This grating turret allows the user to select a grating that is optimal for the current experiment. When the incoming light interacts with the diffraction grating, it is dispersed and then projected to the detector for imaging. Figure 4.6 shows the optical light path in the spectrometer (Princeton Instruments IsoPlane 160) used in this setup.

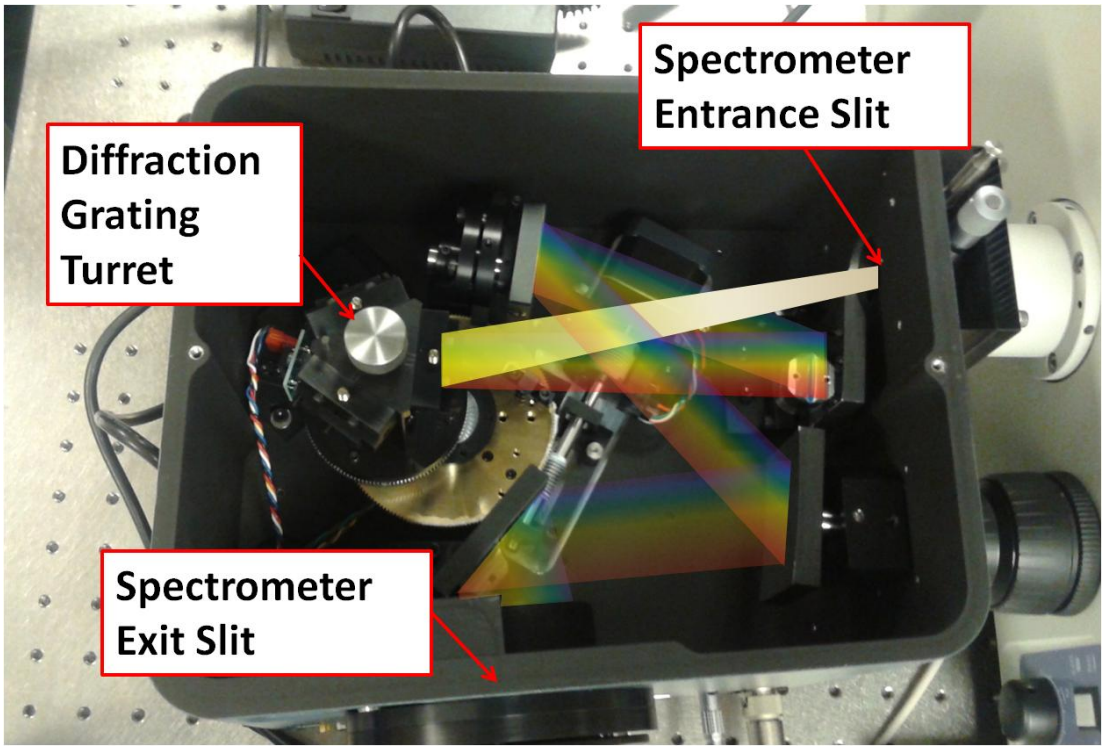

Figure 4.6 Light Path and Diffraction within the Spectrometer. Within the spectrometer, the light is dispersed by the grating mirror and then focused on the CCD detector.

The selection of an appropriate diffraction grating is an important step for optimizing the systems spectral resolution, spectral range, and quantum efficiency. Diffraction in a ruled grating will occur when light interacts with grooves on the grating surface. The constructive and destructive interference patterns that occur during this interaction produce diffraction patterns of different orders, shown in Figure 4.7 [154].The zero order (m = 0) diffraction pattern is a direct reflection, resulting in no dispersion [155]. The first order (m = ±1) diffraction bands result in dispersion and are typically the bands imaged by the detector [154]. Higher order dispersion bands (-2 ≥ m ≥ 2) are more difficult to use for spectroscopy because they tend to overlap, resulting in signal error [156]. In addition, higher order diffraction bands have less energy than the first order bands, which makes signal visualization difficult.

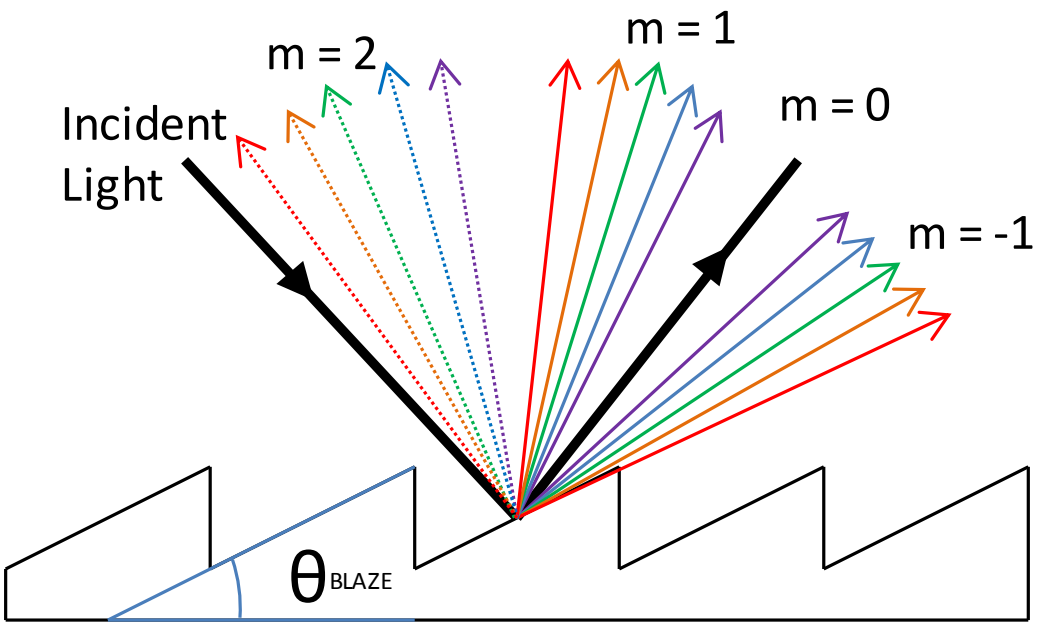

Figure 4.7 Dispersion Order and Blaze Angle of a Diffraction Grating. Multiple dispersion bands, or orders (m), are produced when light is dispersed by a diffraction grating. The wavelength for maximum grating efficiency is determined by the blaze angle of the grating (θ_{BLAZE}).

To increase the quantum efficiency of the spectrometer, the grating is designed with a specific blaze angle (θ_{BLAZE}). The blaze angle is the angle between the grating surface and the triangular ruled lines that produce diffraction patterns. By selecting a grating with a groove density and blaze angle that matches the Raman excitation source, high spectrometer quantum efficiency can be achieved. In the case of this Raman microscope system, a grating with 1200 groves/mm and 750 nm blaze was chosen to optimize spectral resolution and system quantum efficiency in the NIR region. Refer to Figure A1 in the appendix for the quantum efficiency curve for this spectrometer system.

4.2.4 Detector and Data Processing

Dispersed light from the spectrometer was directed to the detector, a PIXIS 400™ low noise CCD detector from Princeton Instruments. The detector was thermoelectrically cooled to a temperature of -75˚C. Cooling of the detector increased system sensitivity by reducing the amount of dark current in the system. Dark current, is the amount of electrical current that passes through the CCD when there are no photons entering the array. Dark current is the main source of noise for the detector and can reduce the signal to noise ratio resulting in reduced Raman intensities. Lower temperatures reduce the dark current noise and increase the detector sensitivity [147].

The detector imaging area is a 1340 x 400 pixel CCD array with a 20µm pixel size. When a spectrum is first acquired, it is acquired as a spectral image. To convert the image into a traditional Raman spectrum the data must be binned. The binning process increases the signal-to-noise ratio (SNR) by averaging pixel charge over the rows of the CCD array. There are two methods for binning: software binning and hardware binning. Software binning allows the user to combine spectral image data after acquisition. This flexibility is important for the setup and

alignment of a spectrometer and for unique post processing of spectral image data. In software binning, the full spectral image is saved and then post processing is used to combine image pixels and increase SNR.

In hardware binning, the adjacent pixel charge is combined during readout time. This binning process occurs by sequentially shifting the charge down the array rows and combining the charge in the readout register (See Figure 4.8). Hardware binning combines the spectral image data into a single Raman spectrum. Hardware binning was the most common data processing method used when acquiring Raman spectra for this research. The advantage of hardware binning is that it occurs during readout time and results in decreased processing time, decreased memory requirements, and increased SNR when compared to software binning.

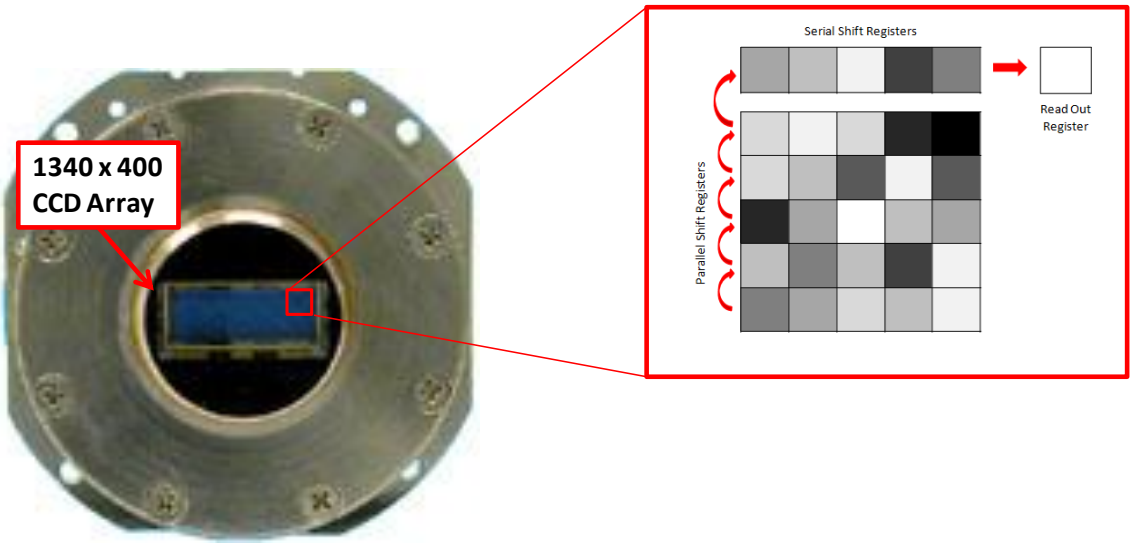

Figure 4.8 CCD Array and Hardware Binning. The detector has a 1340 x 400 pixel CCD array, which is used to detect the light dispersed by the spectrometer. Hardware binning was used to automatically combine adjacent pixel charge values to process a single Raman spectrum in the readout register [157].

4.3 System Calibration, Alignment, and Performance

Before operating the Raman microscope system, calibration and alignment were performed. System calibration will be discussed in Section 4.3.1, and alignment in Section 4.3.2. Once the system was aligned and calibrated, Raman spectrum were acquired and system performance was evaluated, Section 4.3.3.

4.3.1 Raman System Calibration

The Raman system was calibrated with Princeton Instruments IntelliCal ^{TM} calibration source lamps. The lamps were used to calibrate the system for both wavelength and intensity accuracy. The wavelength calibration source has a neon-argon bulb with several emission lines in the NIR region of the electromagnetic spectrum. To ensure that the system calibration would continue to be valid for future Raman measurements, the calibration source was placed on the microscope stage so that the calibration source light would travel the same optical path as the Raman scattering. The automatic calibration routine compared the peaks of the neon-argon source lamps to neon and argon emission lines from the National Institute of Standards and Technology (NIST) atomic spectral database [158, 159]. Through an algorithm based on Rietveld refinement [160], the calibration error was assessed and the wavelength assignment was adjusted accordingly [159].

Intensity calibration was performed using a thermally stable LED source with emission lines from 400 – 1100 nm [159]. The intensity calibration source was placed directly at the spectrometer entrance slit and the spectral intensity of this source lamp was compared to internal intensity standards stored in the device firmware [159]. After intensity comparison, the relative peak heights were adjusted accordingly. Intensity calibration was used to correct for

peak elongation and spectral stitching artifacts caused by the spectral response of optical elements in the Raman system [159].

4.3.2 Raman System Alignment

To acquire accurate Raman spectra, the laser was aligned and focused onto the spectrometer plane. Because the laser alignment process requires the direct visualization of laser scattering, the laser power at the sample was reduced to less than 1μW. Reduced laser power ensured that the optical damage threshold of the sensitive CCD detector was not exceeded. To visualize the laser spot scattering, the Rayleigh filter was removed from the filter block. By removing the Rayleigh filter, a small portion of the Rayleigh scattered laser light entered the spectrometer and hit the detector. The spectrometer grating was positioned so that the zero-order diffraction band was imaged by the detector. This positioning resulted in spectral reflection off the grating rather than dispersion, which was necessary for visualization of the laser spot. The spectrometer entrance slit was opened as wide as possible so that the position of the laser spot on the CCD detector could be determined.

After the sample was focused using the microscope focal knobs, the minimum laser spot size and scattering noise was observed (see Figure 4.9). It was important to first minimize the laser spot size so that laser alignment could be accurately performed. Laser spot alignment was achieved using the micrometer knobs on the laser entry port. After the laser spot was centered on the CCD array, the slit was closed to a point that the width of the laser spot was only 5-10 pixels (see Figure 4.9). This process ensured that the laser scattering would be focused on the spectrometer entrance slit, even when the slit has a 50μm slit width. Once laser alignment and focusing occurred, the system was finally ready for Raman spectrum acquisition.

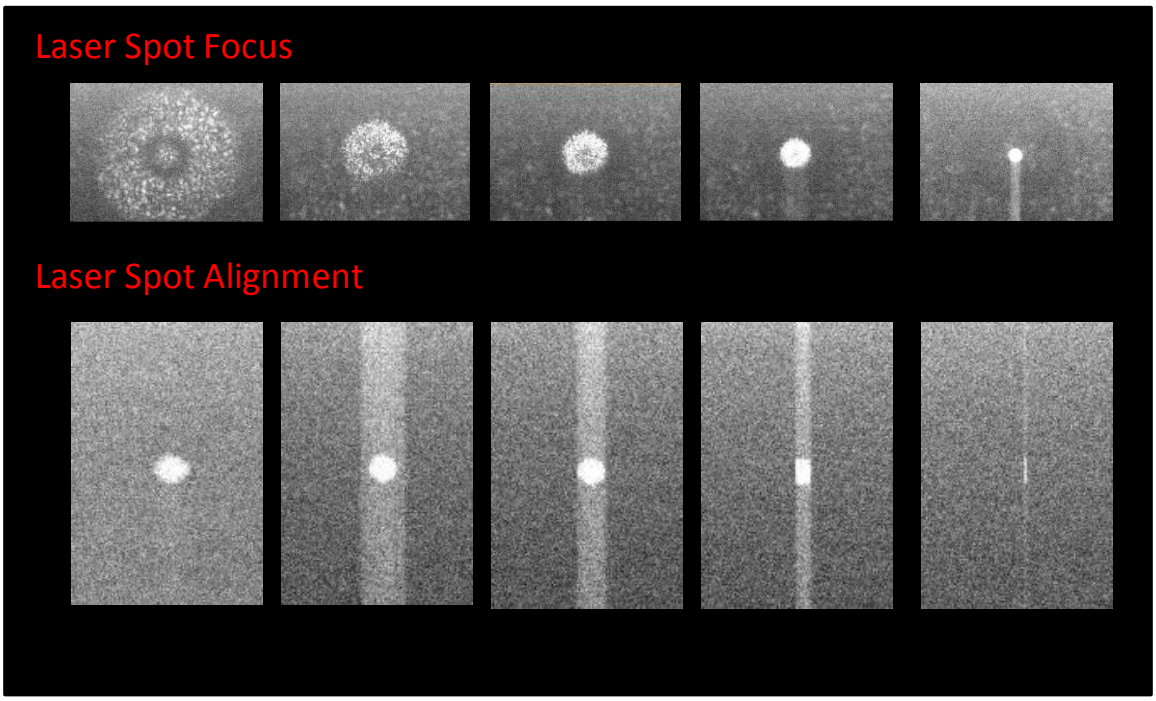

Figure 4.9 Laser Spot Focus and Alignment. The laser spot was imaged by the CCD detector and was then focused and aligned so that the spot was centered on the spectrometer entrance slit.

4.3.3 Raman System Performance

To collect a Raman spectrum, the grating position was changed so that the first order diffraction band was imaged by the detector. Specifically, the grating mirror was positioned so that the Stokes-Raman shift was within the detector range and the Rayleigh scattering was outside the detector range. To do this, the detector center wavelength was set to greater than 830nm. A center wavelength of 830nm resulted in a spectral range of approximately 790 nm to 870nm. Once the correct position of the grating mirror was determined, the Raman spectrum of polystyrene was acquired (Figure 4.10). The Raman spectrum was acquired as either a spectral image or a standard Raman spectrum. If a spectral image was acquired, it was converted to a standard Raman spectrum by software binning the image data as described in section 4.2.4.

The spectral image was segmented to increase peak contrast in the resulting standard Raman spectrum. Binning and segmentation helped increase the SNR by averaging pixel charge and by removing noise generated in the spectral image. To remove image noise, a region of interest was created around the Raman spectrum. The region of interest contained only the Raman scattering signal and excluded areas on the detector that did not contain Raman scattering information. After the region of interest was selected, the Raman spectral image was binned and a standard Raman spectrum produced (Figure 4.10). Through segmenting and binning, the weak Raman signal was separated from the background noise and Raman peaks were identified.

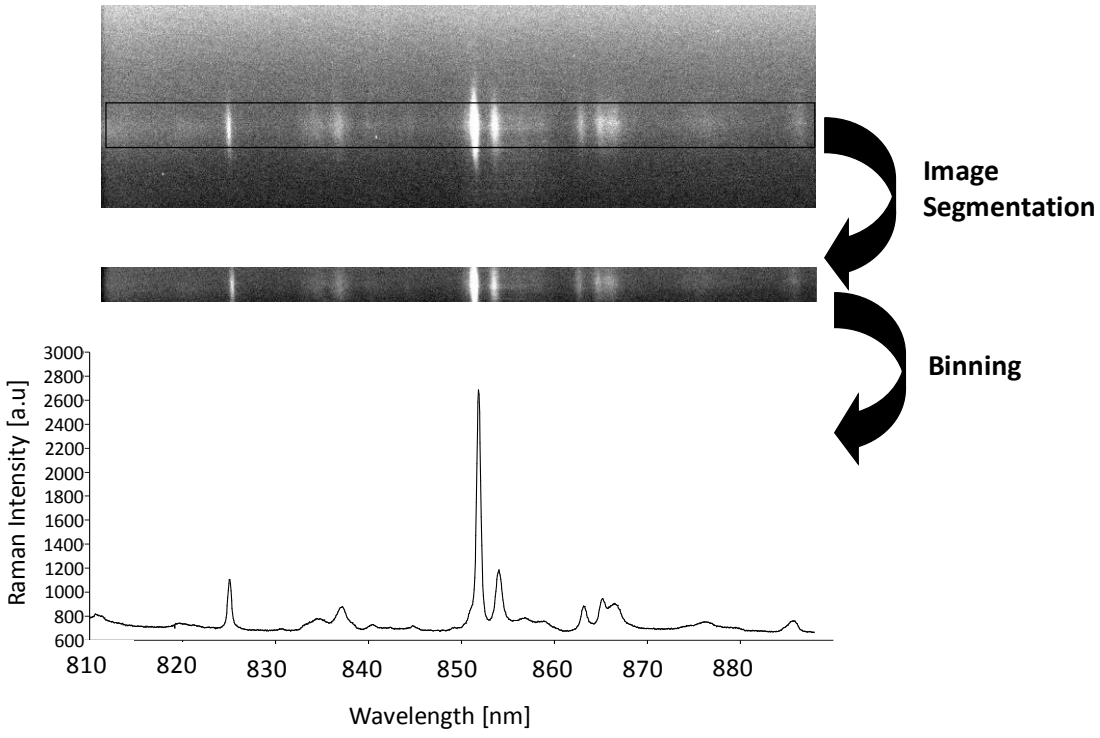

Figure 4.10 Raman Spectrum Acquisition and Post Processing. By segmenting the Raman spectral image and binning the data a standard Raman spectrum was produced.

4.4 Conclusion

The design of a NIR Raman microscope system was a challenging task that required attention to detail and a methodical approach. The basic concepts of geometric optics and light scattering theory were used to design a sensitive Raman microscope system that was used for standard Raman spectroscopy and can easily be modified for future applications. In this chapter, the four basic components of a Raman microscope system were discussed: the laser entry port, the microscope and filters, the spectrometer, and the detector. In addition, the calibration, alignment, and performance of this system were presented. In the next chapter, our Raman microscope system was used to characterize SERS probes designed for biomarker targeting.

CHAPTER 5

DESIGN OF NEAR-INFRARED SERS PROBES FOR BIOMARKER TARGETING

5.1 Introduction

The design and fabrication of SERS probes for biomarker targeting requires nanoscale characterization and optical uniformity. The optical characteristics of SERS probe nanoparticles are influenced by a several factors including contamination, fluorescence, aggregation state, and reporter density. During fabrication, each of these factors needs to be controlled so that a uniform optical response can be achieved. The schema presented in Figure 5.1 illustrates the method used for the fabrication of SERS probes. SERS probes were first fabricated without antibody conjugation (Route 1 in Figure 5.1). After method refinement, antibody-conjugated SERS probes were developed and tested (Route 2 in Figure 5.1) in an immunoassay format. The resulting SERS immunoassay shows promise for multiplex biomarker quantification and specific targeting and detection in a variety of environmental conditions.

5.1.1 Challenges of SERS Probe Synthesis

For these SERS-based studies, an important challenge that had to be addressed was the aggregation potential of the nanoparticles. In their native state, the gold nanoparticle surface is encased with a capping agent that prevents aggregation by charge neutralization or by steric hindrance. When a nanoparticle solution's ionic potential becomes too high, it can neutralize or disrupt the capping layer resulting in charge-induced aggregation of the nanoparticles [161]. The aggregation state of gold nanoparticles was determined by observing the color of the nanoparticle solution as seen in Figure 5.2. Nanoparticle aggregation causes a shift in the particles' LSPR peak and light scattering profile.

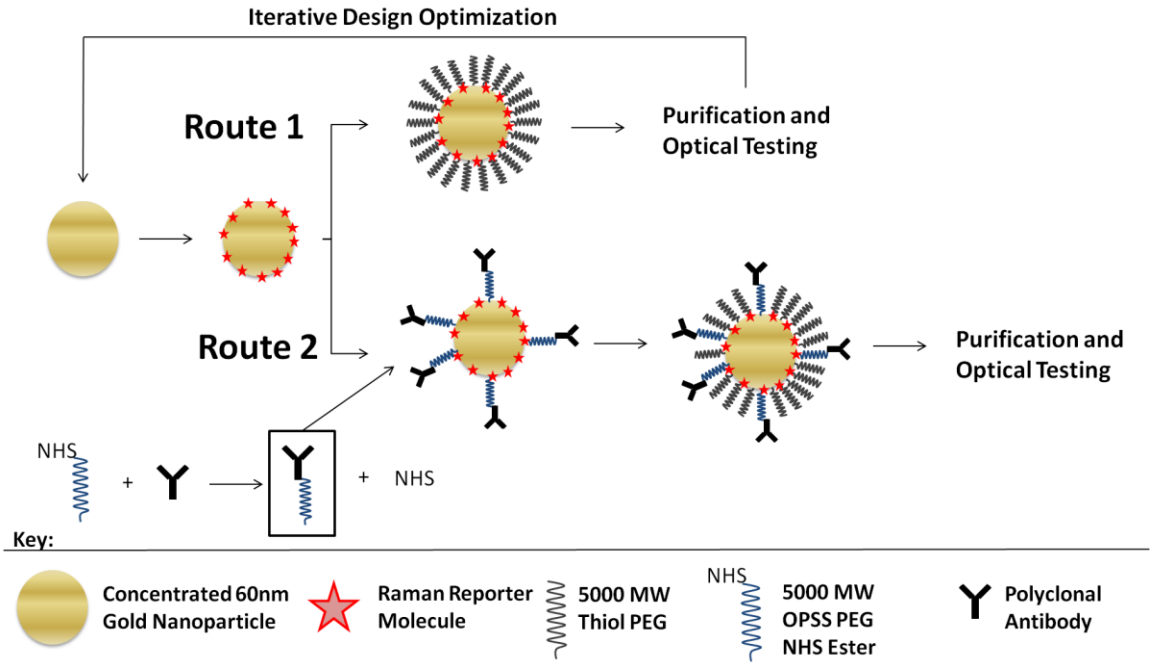

Figure 5.1 Schema for the Fabrication of SERS Probe Nanoparticles. SERS probe nanoparticles were first constructed without antibody conjugation (Route 1). After the successful production of unconjugated nanoparticles, antibody conjugation and testing of SERS probes was successfully conducted (Route 2).

The particle aggregation state is of particular importance for SERS nanoparticles because it will have a significant effect on the optical response of the probes. The particle's LSPR peak position is directly related to nanoparticle size and electromagnetic properties [162]. Depending on the LSPR peak position, aggregation can cause either a decrease in the SERS intensity [163] or an increase in the SERS intensity [164]. This phenomenon can be explained by considering the trade-off between increased SERS intensity caused by plasmon resonance enhancement and hot spot formation [165] verses the decreased SERS intensity caused by the excitation of non-radiative modes in large nanoparticle aggregates [166]. In the case of SERS probes development for biomarker targeting, aggregation was avoided, as it interfered with antibody binding.

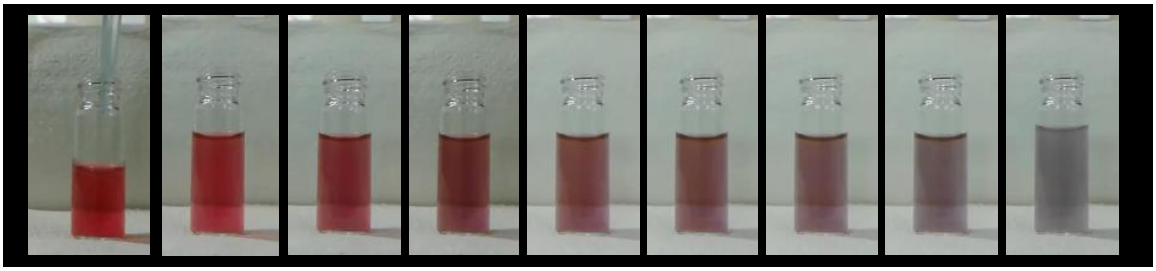

Figure 5.2 Aggregation of Gold Nanoparticles. These images show the change in nanoparticle color upon addition of a 0.15M solution of sodium chloride. The progressive change in color can be directly correlated to the formation of nanoparticle aggregates.

To avoid aggregation, it is important to use ultra pure water (18 MΩ-cm resistivity) when working with gold nanoparticles. Using ultra pure water minimizes the potential for aggregation and promotes consistent and repeatable results. However, the use of ultra pure water can have an adverse effect on the structural and functional properties of antibodies during conjugation. Ultra pure water will induce protein conformational changes and insolubility [167, 168]. Because of this tendency, the conjugation of proteins to the nanoparticle surface becomes a balancing act between aggregation potential and protein stability. The ionic strength of the gold nanoparticle solution during conjugation must remain high enough to promote protein stability without causing nanoparticle aggregation. Step-by-step characterization of the gold nanoparticles during fabrication was used to ensure that this balance between aggregation potential and protein stability was maintained.

5.1.2 Characterization Methods

Characterization methods during each synthesis step were critical for the development of effective and repeatable SERS probes. To develop reproducible SERS probes, the following characterization techniques were used: Raman spectroscopy (633 nm and 785 nm), dynamic

light scattering (DLS), UV/Vis spectroscopy, zeta potential, atomic force microscopy (AFM), scanning electron microscopy (SEM), scanning transmission electron microscopy (STEM), and gel electrophoresis. The following characterization techniques were used to provide information about the particle size and the particle's optical response: UV/Vis spectroscopy, DLS, and Raman spectroscopy.

UV/Vis spectroscopy is a technique that detects absorption of ultraviolet and visible light by molecules or nanoparticles. The absorption profile can be used to detect many molecular characteristics, including the presence of double bonds. UV/Vis spectroscopy is particularly useful for quantification of plasmonic nanoparticles because it can be used to detect their LSPR response. UV/Vis spectroscopy was used to assess the magnitude of the LSPR response and aggregation state of the gold nanoparticles after each step in the fabrication process. The LSPR response is characterized by a maximum absorption point (or LSPR peak) found in the range of 520 – 560 nm. The position of the LSPR peak can be used to estimate the relative size of the nanoparticles as well as their surface state. Additionally, the width, height, and position of the LSPR peak can be used to estimate the aggregation state of the nanoparticles. In Figure 5.3, the LSPR peak shape of 60nm gold nanoparticle is shown.

DLS was used to determine the size and monodispersity of gold nanoparticle solutions during the fabrication process. DLS characterizes a solution of particles based on light scattering variation caused by nanoparticle Brownian motion [169]. Due to Brownian motion, the scattering photons interact through constructive and destructive light interference [170]. These interference patterns can be correlated to the average hydrodynamic radius and particle size distribution [170]. DLS measurements were used for the characterization of particle size throughout the fabrication process. Particle size was also measured using AFM and SEM/STEM.

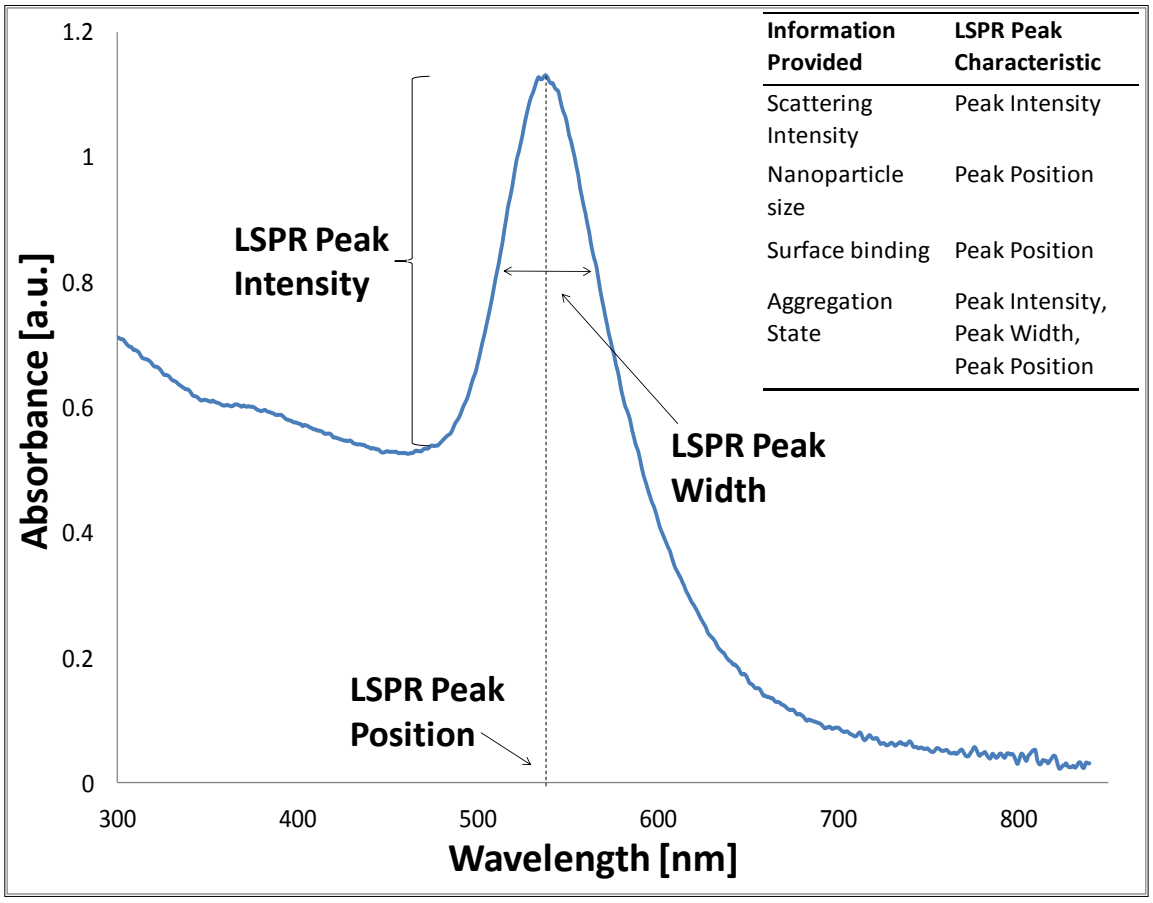

Figure 5.3 UV/Vis Characterization of Gold Nanoparticle LSPR Peak. The localized surface plasmon resonance (LSPR) peak response can be used to determine multiple characteristics of gold nanoparticles including their aggregation state.

Raman spectroscopy was used throughout the fabrication process to determine the optical response of the nanoparticles. Step-by-step characterization of the optical response was important for the development of a fabrication process that would prevent Raman reporter displacement or inactivation. Additionally, Raman spectroscopy was used for the selection of an appropriate Raman reporter molecule with reduced fluorescence, a strong Raman signal, and Raman peak positions unique from Raman peaks seen in polystyrene. Unique and non-

overlapping peaks were important because polystyrene substrates were used for protein binding and SERS immunoassay development.

5.2 Design and Characterization of SERS Probes without Antibody Conjugation

Before attempting to conjugate antibodies to the surface of SERS probe nanoparticles, the optical response of unconjugated SERS probes was assessed (see Route 1). Unconjugated SERS probes have been used for a variety of labeling, and multiplexing applications [80, 171, 172]. The development of unconjugated SERS probes was critical for future SERS probe antibody conjugation but also has potential for unique, label free biosensing.

5.2.1 Materials and Methods

In the preparation of unconjugated SERS probes the follow materials were obtained: citrate capped, 60nm gold nanoparticles (Ted Pella), 5000MW thiol polyethylene glycol (PEG) (from Laysan Bioscience), 4-aminothiolphenol (4-ATP), 4-mercabtobensoic acid (4-MBA), crystal violet, malachite green, (3,3')-diethylthiatricarbocyanine iodide (DTTC iodide), quartz microscope slides (Ted Pella).

To fabricate unconjugated SERS probes, the aggregation potential of each reporter molecule was first determined. Raman reporters such as 4-ATP and 4-MBA bind to the particle surface through the gold thiolate bond and stabilize the particle surface. Crystal violet, malachite green, and DTTC iodide bind to the surface through ionic interactions so reporter aggregation is more likely with these reporters. For each Raman reporter, a stable reporter-to-colloid ratio was determined and was used in subsequent experiments. For reproducible production of SERS probe nanoparticles, 60nm gold nanoparticles, at a concentration of 2.6×10^{10} nanoparticles per milliliter, were added to a clean glass vial and were rapidly stirred with a

magnetic stir bar. The reporter molecule was added dropwise to the stirring colloid solution at 1:6 volumetric ratio. This reporter addition procedure helped to create a uniform reporter distribution across the nanoparticle surface and reduced batch-to-batch variability. The reporter solution incubated with gold nanoparticles for 1 hour to promote surface binding. After incubation, a 10μM solution of 5000 molecular weight thiol polyethylene glycol (SH-PEG) was added to the solution and incubated for an additional hour. Finally, the particles were centrifuged at 1200xg for 30 minutes and the supernatant was removed. The particles were suspended in ultra pure water and stored at 4˚C until optical testing.

5.2.2 Raman Reporters and Aggregation Characteristics

The Raman spectrum of each reporter molecule was analyzed using either 633nm or 785nm excitation. The normalized reporter spectra are presented in Figure 5.4 with a spectral range of 400 – 1200 cm^{-1}. To determine the best reporter molecule for immunoassay development, the Raman spectrum of each reporter molecule was compared to the spectrum of polystyrene. Spectra with high SERS intensity and little or no polystyrene peak overlap were considered good candidates for the development of a SERS based immunoassay.

The aggregation potential of each reporter molecule was determined by adding the reporter to a solution of gold nanoparticles in varying concentrations ranging from 0 to 5000nM. UV/Vis spectroscopy was used to analysis the LSPR peak for each nanoparticle solution. An example of the LSPR peak profile of gold nanoparticles with the reporter molecule DTTC iodide is presented in Figure 5.5. In this figure, the increasing LSPR peak width and decreasing LSPR peak intensity indicated that particle aggregation had occurred. The cluster size of nanoparticle aggregates was estimated using DLS; DLS data is presented in the top right corner of Figure 5.5.

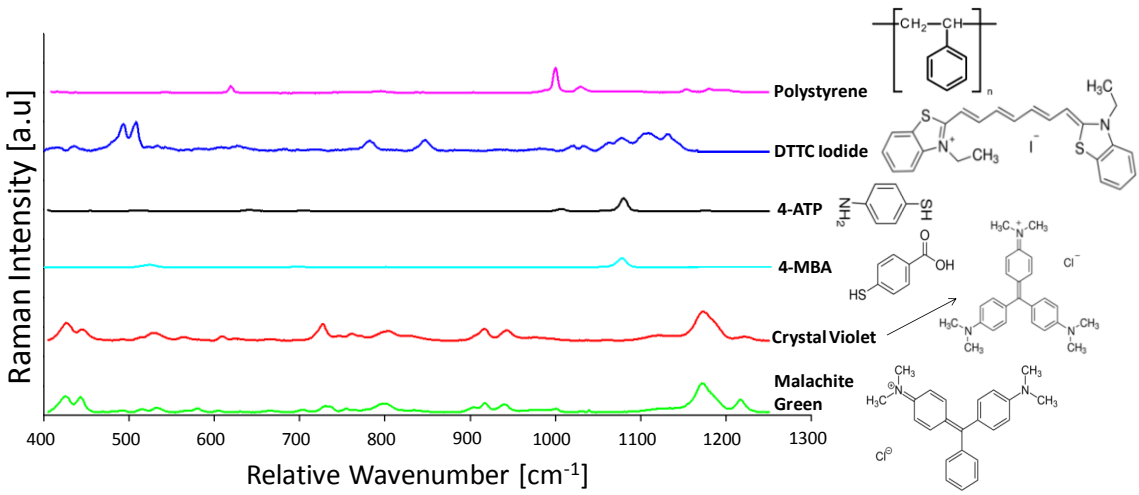

Figure 5.4 Raman Reporter Spectra. Five commonly used Raman reporters were tested to determine their Raman intensity and their aggregation potential.

The Raman intensity of each reporter is dependent on the reporter density, the SERS enhancement, the Raman instrument throughput, and the aggregation state of the nanoparticles. After experimenting with the five Raman reporter molecules, it was determined that DTTC iodide produced the strongest Raman enhancement with the shortest required acquisition time. A strong optical response with a short required acquisition time was an important factor for the eventual development of a SERS immunoassay. Reporter molecules that require a short acquisition time were beneficial because they resulted in reduced interference caused by the polystyrene substrate. The strong optical response of DTTC iodide can be explained when considering its maximum absorption point. DTTC iodide is a NIR dye with an absorption maximum at 765nm. Because DTTC iodide has a maximum absorption point near the laser excitation wavelength, Resonance Raman Enhancement will occur in addition to SERS. The Resonance Raman Effect results in increased Raman enhancement and reduced acquisition time.

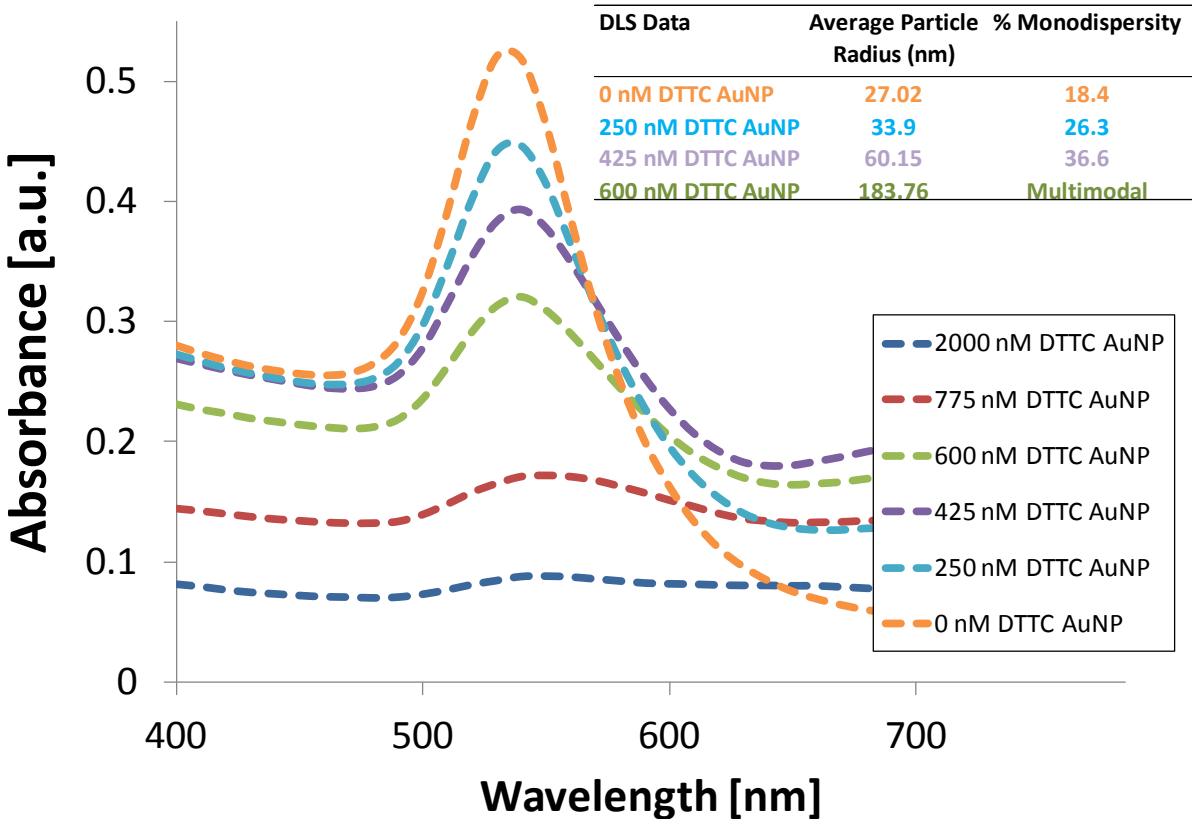

Figure 5.5 Aggregation of Gold Nanoparticles (AuNP) After the Addition of DTTC Iodide. The aggregation potential of 60nm gold nanoparticles was determined by adding DTTC iodide to the gold nanoparticle solution and observing the LSPR peak profile of the particles. DLS data shows that the particle size and percentage monodispersity increased as greater concentrations of DTTC iodide were added to the gold nanoparticle solution.

5.2.3 Thiol PEG Binding Density

After binding the Raman reporter to the gold nanoparticle surface, a 5000 molecular weight SH-PEG layer was added to surface. To test the gold nanoparticles ability to resist aggregation, a solution of 0.15 M sodium chloride was added to the SH-PEG nanoparticle mixture to promote aggregation of unprotected particles. The LSPR peak intensity was measured before and after addition of the sodium chloride. The resulting difference in the absorption at the LSPR peak position was measured to determine the SH-PEG concentration

required to stabilize the particles. A large difference in the LSPR peak intensity indicates that aggregation of the particles occurred. Figure 5.6 shows that the amount of SH-PEG required to effectively stabilize the particle surface is approximately 2uM. The PEG binding density was calculated using the concentration of gold nanoparticles in the solution and the concentration of SH-PEG required to stabilize the particles. The number of SH-PEG molecules required to stabilize the particle surface was approximately 20,000 SH-PEG molecules per nanoparticle. This value corresponds to a SH-PEG footprint (area occupied by the SH-PEG molecule on the nanoparticles surface) of 0.244 nm^2 which is consistent with the footprint value of 0.214 nm^2 reporter for thiol monolayer's on a gold surface [173, 174].

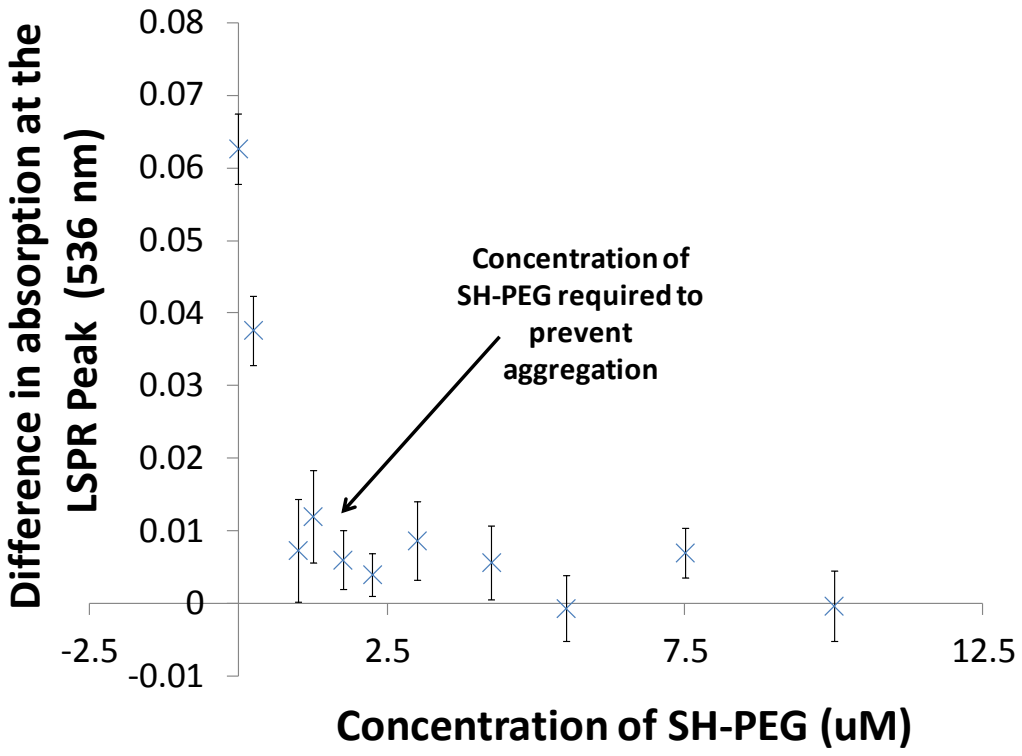

Figure 5.6 SH-PEG Nanoparticle Stabilization. The amount of SH-PEG required to stabilize the gold nanoparticle surface was measured by comparing the difference in absorption at the LSPR peak for PEG stabilized gold nanoparticles before and after the addition of 0.15 M sodium chloride.

As an additional confirmation of the successful addition of SH-PEG to the nanoparticle surface, the average hydrodynamic radius of the particles was measured before and after addition of SH-PEG using DLS and STEM. For STEM analysis, the PEG-coated gold nanoparticles were centrifuged at a speed of 1200xg for 30 minutes. After centrifugation, the supernatant was removed and the particles were redispersed in 100% ethanol. The resulting nanoparticle suspension was dried on a lacey carbon grid (Ted Pella), and imaged with the SEM microscope in transmission mode. Figure 5.7A is a STEM image showing a nanoparticle corona, suggesting a PEG layer has assembled around the particle. Due to concerns with SEM carbon contamination, which can also produce a corona like layer around conductive structures, DLS was used for the determination of PEG layer thickness (Figure 5.7B). Using DLS, the hydrodynamic radius of gold nanoparticles was measured before and after PEGylation. An average increase in the hydrodynamic radius of 16nm was observed resulting in a final radius of approximately 50nm.

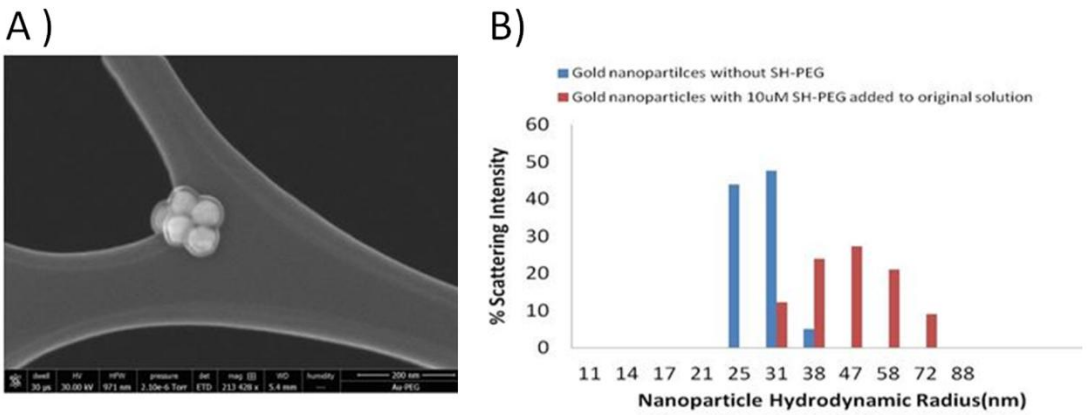

Figure 5.7 PEG Layer Thickness Determined by STEM and DLS. Both STEM and DLS were used to determine the thickness of the PEG layer on the gold nanoparticles surface. An average increase in the hydrodynamic radius of 13nm was observed after the addition of SH-PEG to the particles.

5.2.4 SERS Probe Stability and Signal Robustness

One issue that must be addressed during the fabrication of SERS probes is the possibility of Raman reporter displacement, as illustrated in Figure 5.8. Excess SH-PEG added to the particle surface could cause reporter displacement and a decrease in the SERS signal. Reporter displacement could also be mediated by a change in solvents, which could alter the PEG conformation and enable leaching of the reporter. To address these concerns, five replicates of DTTC iodide SERS probes were fabricated, excess SH-PEG was removed by centrifugation, and probes were stored at 4˚C for two weeks. Raman testing of these probes before and after addition of SH-PEG was conducted to determine if a decrease in the SERS signal would result. The resulting spectra, shown in Figure 5.9, have nearly identical peak heights suggesting that very little reporter displacement occurred due to the addition of SH-PEG and to SERS probe storage.

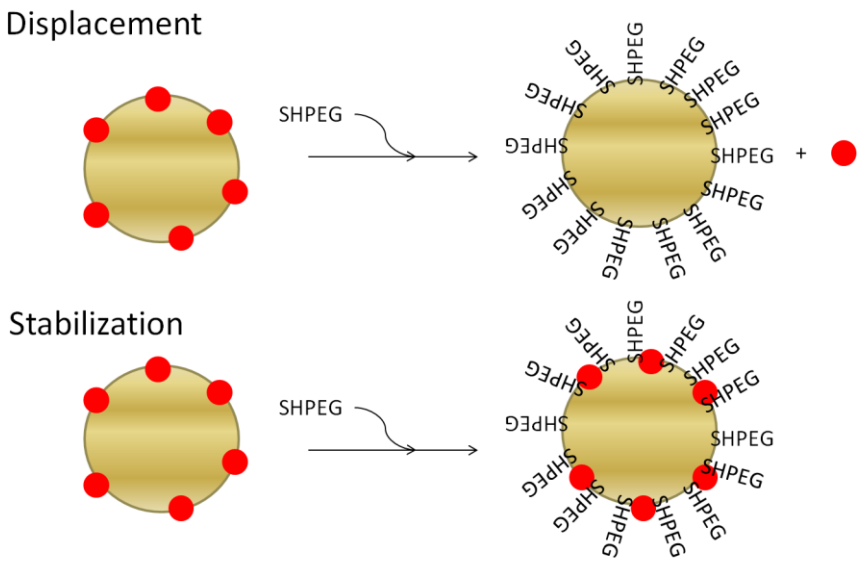

Figure 5.8 Raman Reporter Displacement. Raman reporter molecules can be competitively displaced during SERS probe synthesis. SERS probe stability testing is critical in the development of a fabrication protocol that avoids reporter displacement.

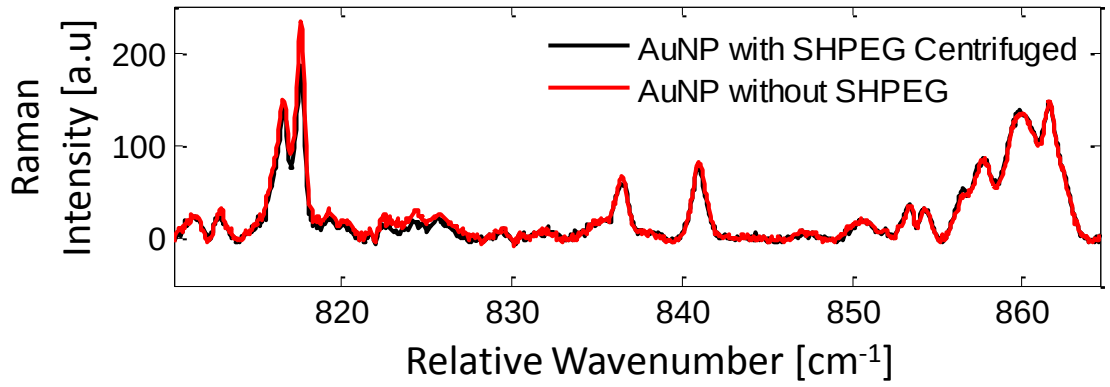

Figure 5.9 SERS Probe Raman Reporter Displacement. After DTTC Iodide SERS probe fabrication and storage, very little reporter displacement was observed. These results suggest that the protocol for SERS probe fabrication is effective at preserving the bound reporter molecule and stabilizing the reporter on the particle surface.

Similar results were obtained when probes were resuspended in a variety of different solvents commonly used with proteins, including; phosphate buffer saline (PBS), tris buffered saline (TBS), and tris buffer saline with 0.05% tween 20 (TBST). To test the ability of SERS probes to give a noticeable signal in extreme conditions, the probes were resuspended in solutions ranging from pH 1-14. The resulting spectra had similar spectral profiles and all gave a strong and noticeable signal.

5.2.5 Summary and Findings from the Fabrication of Unconjugated SERS Probes

Unconjugated SERS probes were fabricated as indicated in Route 1, Figure 5.1. These probes were tested to determine the optimal Raman reporter molecule and reporter concentration. Additionally, unconjugated SERS probes were evaluated to determine the optimal SH-PEG binding density. Unconjugated SERS probes fabricated using this method are robust and produce a consistent SERS response during probe development and over time. The

initial development and characterization of unconjugated SERS probes was an important step in the development of a SERS-based immunoassay for biomarker targeting and detection.

5.3 Design and Characterization of SERS probes with Antibody Conjugation

Antibody-conjugated SERS probes were created as illustrated in Route 2, Figure 5.1. To develop SERS probes for specific targeting and detection, antibodies were conjugated to active PEG molecules. Antibody-PEG conjugation was followed by the addition of the antibody to the gold nanoparticle at concentrations that result in stability of the antibody and reduced aggregation potential for the gold nanoparticles. Successful antibody conjugation was determined using a 96-well immunoassay format for detection of light scattering from gold nanoparticles bound to the plate through immunochemistry.

5.3.1 Materials and Methods

All reagents mentioned in section 5.2.1 were used during the fabrication of conjugated SERS probe nanoparticles. In addition, the following items were obtained for this portion of the project: An activated PEG-NHS-ester molecule referred to as Orthopyridyl-Disulfide-PEG-Succinimidyl Valerate (OPSS-PEG-SVA) [Laysan Bioscience], anti-human and anti-mouse IgG polyclonal antibodies (Pierce), human and mouse IgG control antibodies (Pierce), human serum albumin (Sigma Aldrich) , medium and high protein binding polystyrene microplates (Corning), AAA Superblock™ immunoassay blocking solution (ScyTek), 10K MWCO Zeba Spin buffer exchange columns (Pierce), sodium bicarbonate, barium chloride dihydrate, and 1 N iodine/iodide solution.

Before conjugation of OPSS-PEG to the antibody, the protein was first transferred to a buffer solution of 100mM sodium bicarbonate. After buffer exchange, OPSS-PEG-SVA was added

to the protein solution and the reaction proceeded overnight at 4˚C. Further information about the conjugation reaction can be found in Section 5.3.2. The conjugation effectiveness was determined by SDS-PAGE gel electrophoresis. Two separate stains were used to visualize the PEGylated proteins. The first stain used was a Coomassie blue protein stain to visualize the protein bands in the SDS-page gel. The second stain was a barium chloride-iodine stain, which selectively stains for the PEG molecules bound to the protein surface. See Section 5.3.3 for further information and results for SDS-PAGE of PEGylated proteins. Following protein PEG conjugation, the PEGylated antibodies were bound to the Raman reporter labeled gold nanoparticles. SH-PEG was used to stabilize the particle surface and the antibody-conjugated SERS probes were stored at 4˚C until use in the immunoassay. Section 5.3.4 covers the methods and results for the development of antibody-conjugated SERS probes used for a light scattering immunoassay.

5.3.2 NHS-Ester Chemistry for PEG Antibody Binding

The first step in the fabrication of conjugated SERS probe nanoparticles was the binding of PEG to a polyclonal antibody using an activated NHS-ester PEG molecule. This chemical reaction occurs spontaneously upon the addition of PEG-NHS to the protein solution. At the same time, the PEG-NHS molecule can be hydrolyzed which reduces conjugation efficiency (Figure 5.10). To reduce NHS-ester hydrolysis the PEG-NHS reagent should be immediately added to the protein solution after resuspension. During the conjugation reaction, the protein concentration should be greater than 1mg/ml to promote conjugation rather than hydrolysis. The conjugation reaction produces a covalent amide bond between the PEG molecule and primary amines on the protein surface. The reaction has a higher yield at a pH of approximately 8 – 9, so for most protein solutions the pH must be adjusted for optimal conjugation efficiency.

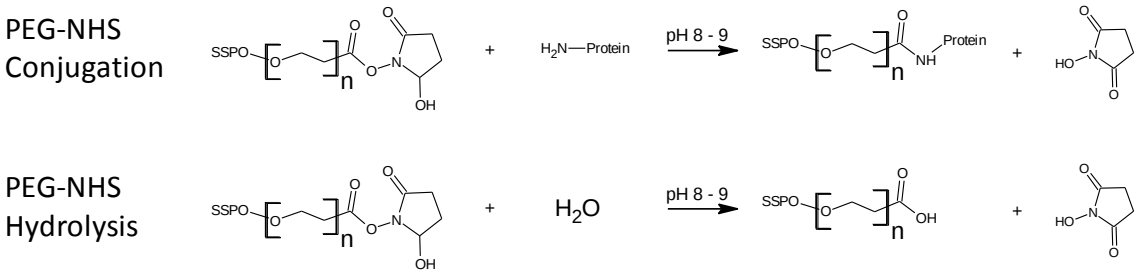

Figure 5.10 PEG-NHS Chemical Reaction. The addition of PEG-NHS to a highly concentrated protein solution results in the covalent binding of the PEG molecule to primary amines in the protein. Hydrolysis of the activated NHS-ester is a competing reaction that reduces the conjugation efficiency.

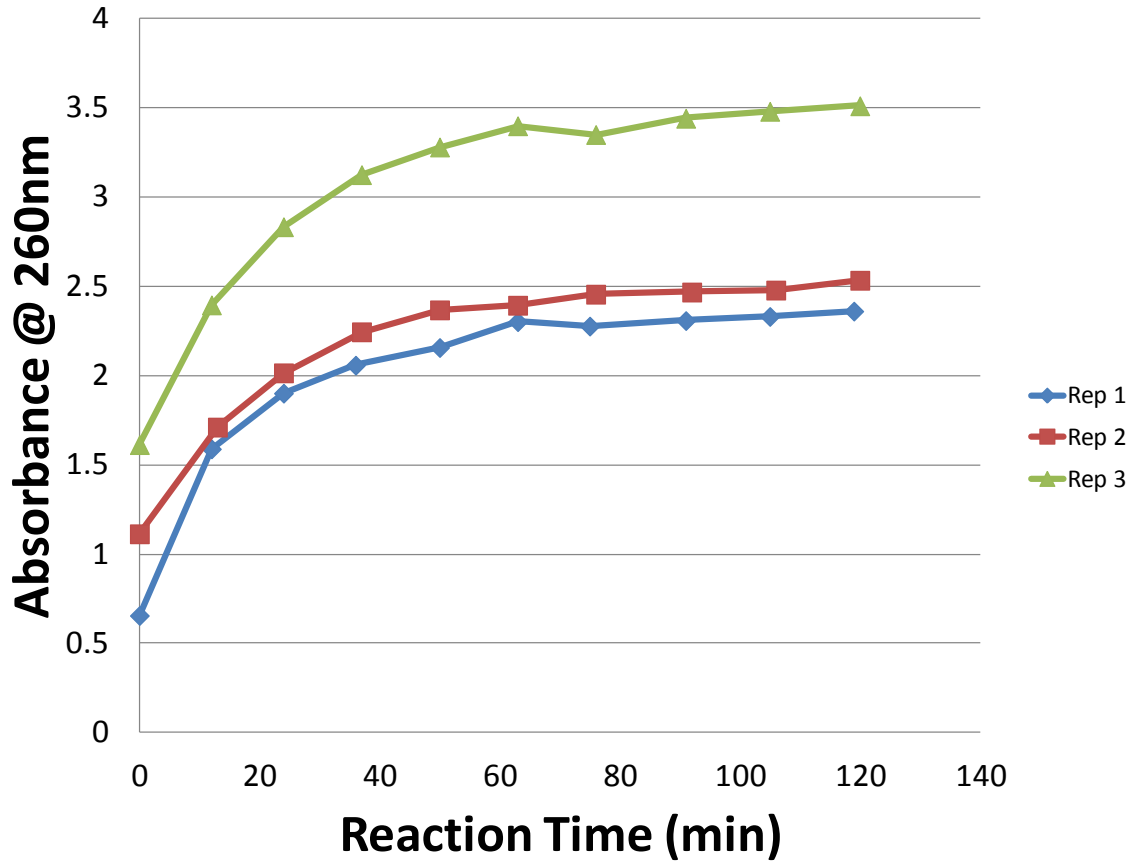

Figure 5.11 Hydrolysis Half-Life of OPSS-PEG-SVA. The hydrolysis half-life of OPSS-PEG-SVA was determined by measuring the absorbance at 260nm for a 2.5-hour period. A hydrolysis half-life of approximately 20 minutes was determined, which corresponds to the manufacturer's specifications.

Another important consideration for the antibody PEG conjugation reaction is the hydrolysis half-life of the activated PEG molecules. The hydrolysis half-life was measured by recording the absorbance of the NHS leaving group at 260nm. By measuring the hydrolysis half-life, the amount of time required for a complete reaction was determined. In Figure 5.11, the absorbance of the NHS leaving group at 260nm was measured to determine the hydrolysis half-life of OPSS-PEG-SVA. The resulting hydrolysis half-life was determined to be approximately 20 minutes, which corresponds to the manufacturer's specifications.

5.3.3 SDS-PAGE Gel Electrophoresis of PEGylated Proteins

SDS-PAGE gel electrophoresis separates proteins based on their molecular weight. When an electrical current is applied to the gel, proteins will migrate through the gel towards the electrode on the opposite side. Proteins with a larger molecular weight migrate a short distance while proteins with a smaller molecular weight travel a longer distance. PEGylation of the proteins produces a protein conjugate with a larger molecular weight, which can be observed in the migration pattern of the protein when run on a SDS-PAG gel.

To determine the conjugation efficiency, OPSS-PEG-SVA at a concentration of 10 mg/ml was added to a 2 mg/ml anti-Human IgG protein solution in molar conjugation ratios of 1:1, 2:1, 4:1, 6:1, 8:1, 10:1, and 15:1. The conjugation reaction proceeded overnight at 4˚C after which the PEGylated proteins were evaluated using SDS-PAGE gel electrophoresis. First, a 7.5% polyacrylamide gel was prepared using a BioRad TGX Fast Cast™ gel casing kit. The PEGylated proteins were prepared with non-reducing lithium dodecyl sulfate sample buffer (Pierce) and placed in a water bath at 100˚C. After cooling, the PEGylated proteins were loaded into the wells of the gel and the gel was run for 75 minutes at 150V using Tris-HEPES-SDS Running Buffer. After

75 minutes, the gel was stained using Coomassie Blue protein stain. Following protein staining, the gel was stained for PEG using 5% w/v barium chloride dissolved in 1N hydrochloric acid [175]. Following barium ion diffusion, the gel was placed in a 0.1M solution of iodine/iodide and incubated for 20 minutes to develop color [176], [175]. The resulting gel is shown in Figure 5.12. The blue/green bands are from protein staining while the brown bands are a result of PEG staining. The gel shows increasing molecular weight and increased PEG staining as a function of the increased conjugation ratio.

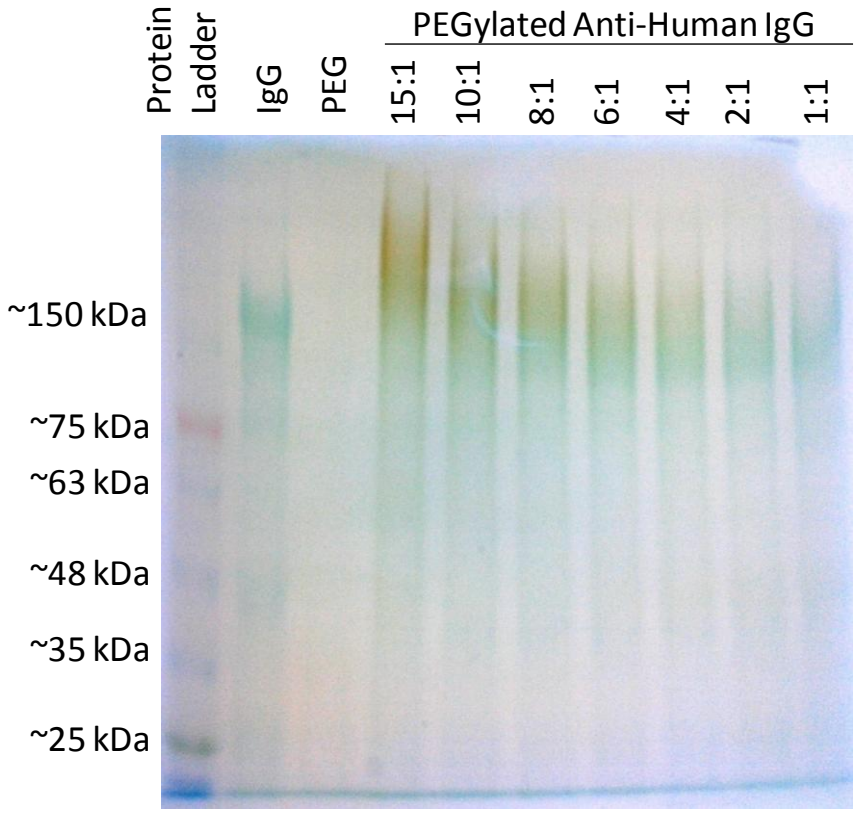

Figure 5.12 SDS-PAGE Gel of PEGylated Protein Conjugates. A SDS-PAGE Gel was stained for protein using Coomassie Blue and for PEG using a barium-chloride-iodine solution. The PEGylation reaction was run at varying PEG to protein ratios ranging from 15:1 – 1:1. The brown iodine stain and increasing molecular weight of the protein conjugates indicates successful PEGylation.

5.3.4 Development of a SERS Probe Light Scattering Immunoassay

A SERS probe immunoassay was developed using PEGylated proteins with the same conjugation ratio as those used for the SDS-PAGE gel. First, 60nm gold nanoparticles were concentrated by centrifugation to a final concentration of $2.6x10^{11}$ nanoparticles/ml. Following concentration, a solution of 1.5μM DTTC iodide was added to the particle surface and the solution incubated for 1 hour. After incubation, PEGylated antibodies were added to the nanoparticle solution at a ratio of 200 antibodies per nanoparticle. Antibody binding to the gold surface was mediated by the disulfide group of OPSS-PEG, which strongly binds to the gold surface. PEGylated antibodies were incubated with the gold nanoparticles for 1 hour. The nanoparticles were stabilized and blocked against non-specific protein binding using SH-PEG. SH-PEG was added to the gold nanoparticles surface at a concentration of 10uM and was incubated for 10 minutes. It was then removed from the solution by centrifugation at 5000xg for 15 minutes.

The schema for development of a SERS immunoassay is illustrated in Figure 5.13. A medium protein binding 96-well polystyrene plate surface was functionalized with Human IgG control protein at a concentration of 50ug/ml (Figure 5.13., Step 1). After antigen binding, the plate was washed with 1x TBST buffer (Figure 5.13., Step 2) and 100ul of AAA superblock was added to each well (Figure 5.13., Step 3). SERS probe antibodies were added to the first column in each well and a 1:2 serial dilution of these probes was made down each column (Figure 5.13., Step 4). The antibodies were incubated for 2.5 hours and then washed with 1x TBST buffer (Figure 5.13., Step 5). Finally, light scattering from the assay was detected using UV/Vis spectroscopy and Raman spectroscopy (Figure 5.13., Step 6).

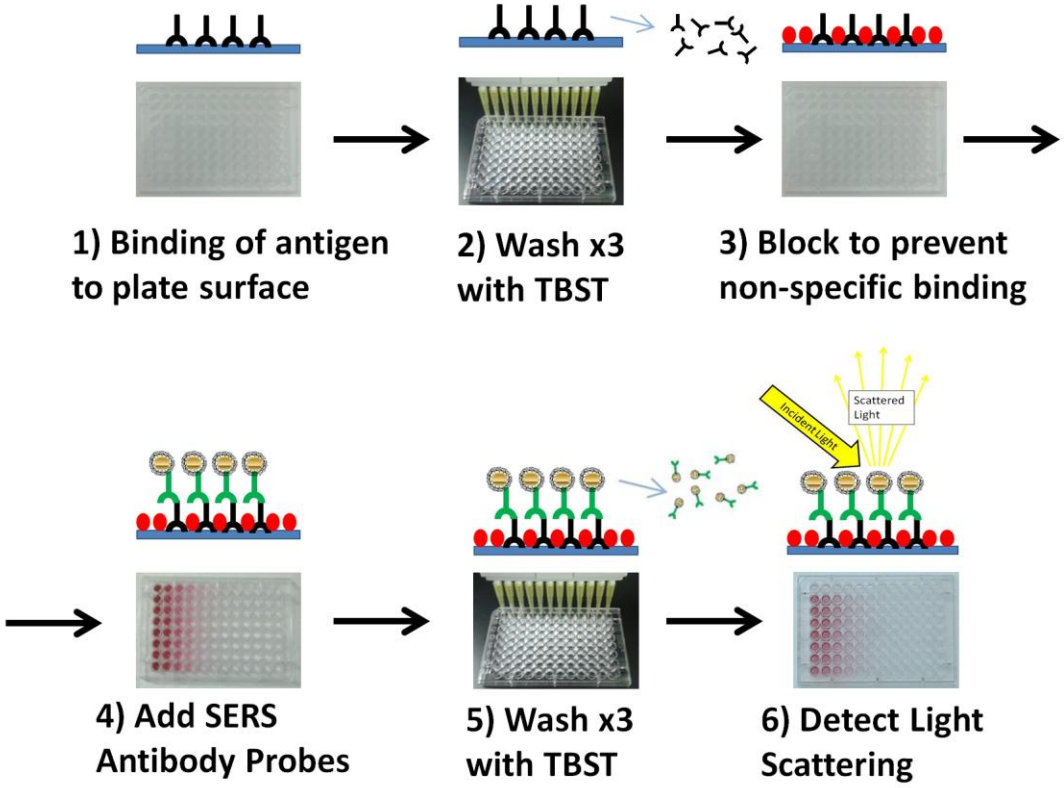

Figure 5.13 Light Scattering Immunoassay. Using light scattering processes, a sensitive direct immunoassay has been developed. Steps 1 through 6 illustrate the process of preparing this light scattering immunoassay.

The addition of high molecular weight PEG molecules to antibodies can interfere with the antibody function [177]. To test the effect of PEG interference on antibody function, SERS probes were fabricated with PEG to antibody molar conjugation ratios of 1:1, 2:1, 4:1, 6:1, 8:1, 10:1, and 15:1. These SERS probes were used in the immunoassay format described in Figure 5.13. The resulting assay shown in Figure 5.14 demonstrates that for conjugation ratios as high at 15:1 there is very little PEG inference. When compared to the control condition (Row A, Figure 5.14) there is significant immunochemical binding in rows B-H. This assay demonstrates the successful development of SERS probes for biomarker targeting and detection.

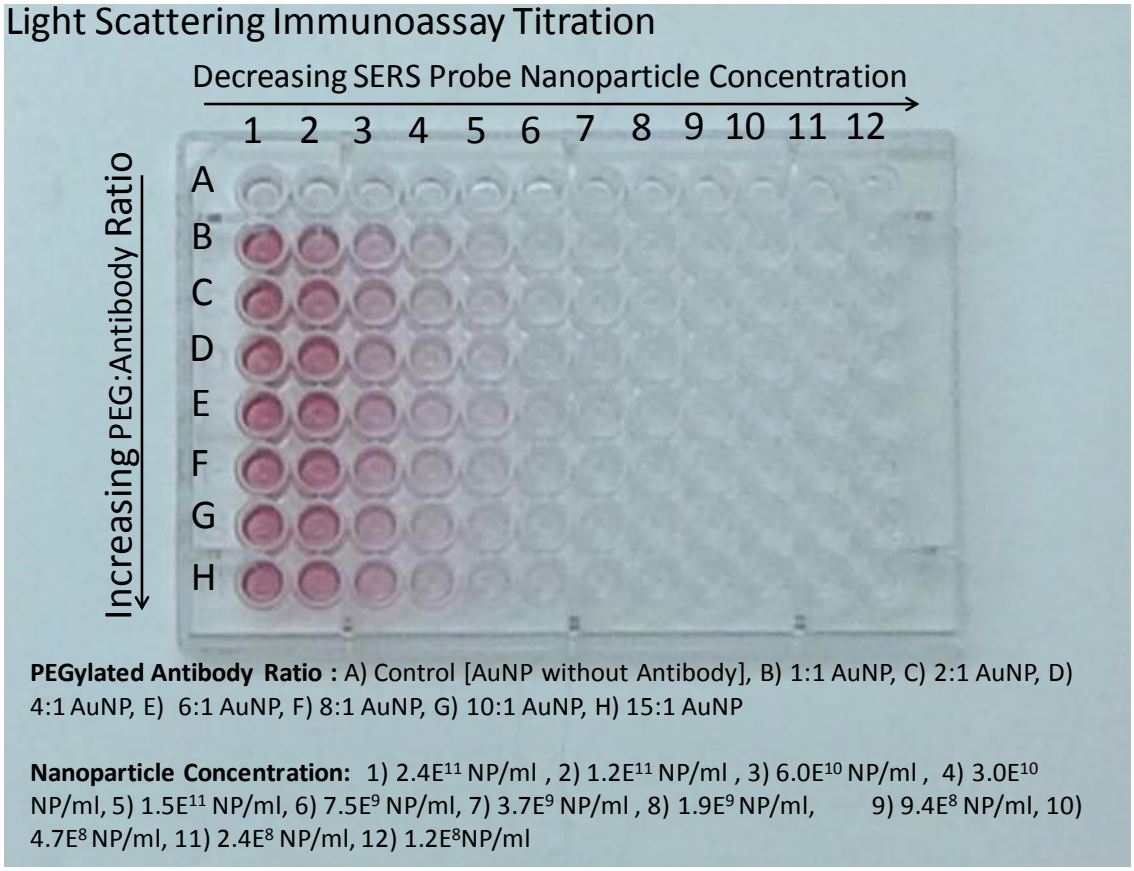

Figure 5.14 Light Scattering Immunoassay Titration. This immunoassay plate demonstrates that specific binding of the human IgG SERS probes was achieved. PEGylation ratios up to 15:1 have minimal interference on the binding ability of the Human IgG SERS probe.

To further quantify the SERS probe immunoassay, measurement of light scattering was acquired using UV/Vis spectroscopy and Raman spectroscopy. UV/Vis spectroscopy was used to measure the absorbance of each well at the LSPR peak position (536 nm). In a typical assay, the absorbance at the LSPR peak could be correlated to the concentration of SERS probe particle using non-linear regression. This relationship is consistent with binding site limited antibody adhesion that is experienced at high concentrations of secondary antibody in a typical ELISA assay [178]. In Figure 5.15, the calibration curve for an anti-mouse SERS probe immunoassay is

shown. This assay used two control conditions. The first control was SERS probes with a conjugated mouse IgG isotype antigen and the second was SERS probe conjugated to human serum albumin. Both control conditions showed negligible light scattering while the anti-mouse SERS probes showed noticeable absorption at the LSPR peak wavelength. Light scattering and absorption from the SERS probes proved to be a valuable technique for the detection of direct immunochemical binding and has applications for direct cell labeling applications.

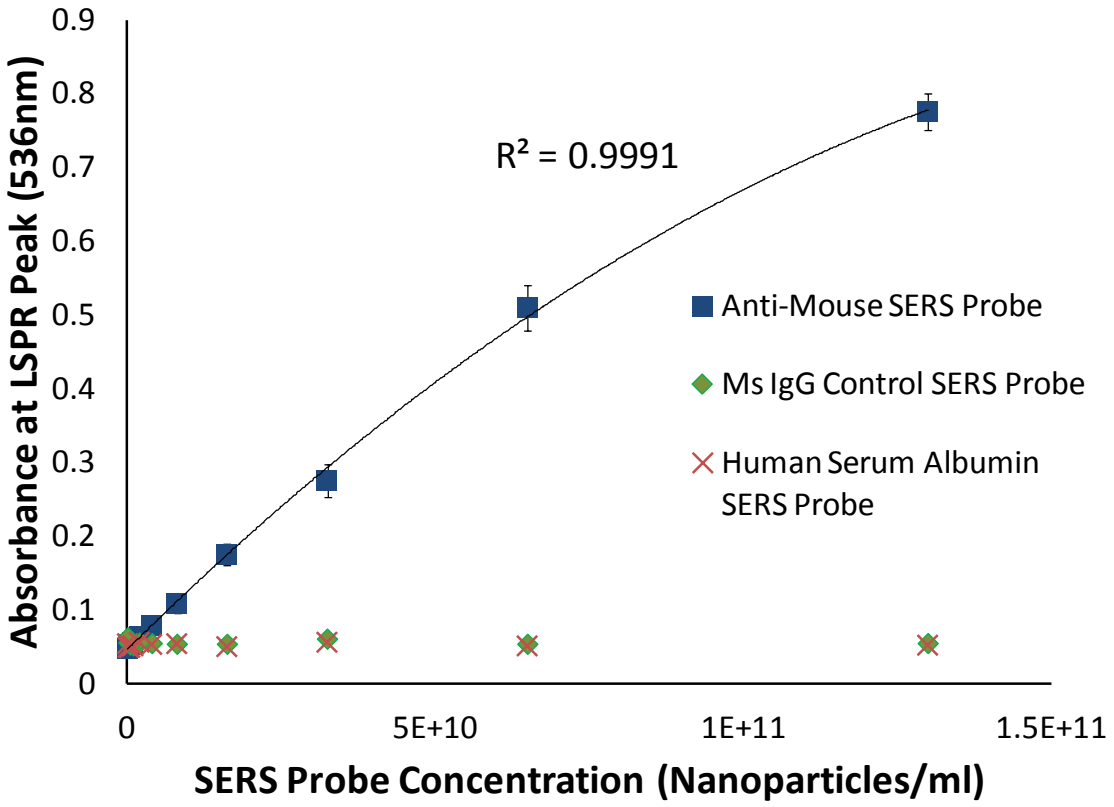

Figure 5.15 Anti-Mouse SERS Probe Immunoassay. The LSPR peak intensities of anti-mouse SERS probes were plotted over a large concentration range. The SERS probe concentration can be related to the absorbance at the LSPR peak position (536nm). Both mouse IgG and human serum albumin SERS probes were used as a control condition. Both controls showed negligible light scattering across the entire concentration range.

To detect the inelastic light scattering from gold nanoparticle immunoassay, Raman spectra were collected using a 3-second acquisition time and 40mW incident laser power. The resulting Raman spectra in Figure 5.16 show peaks that correspond to vibrational modes of both DTTC iodide and polystyrene. The height and spectral area of the DTTC peaks at 493 cm^{-1} and 508 cm^{-1} can be correlated to the concentration of SERS probe added to the solution, see Figure 5.17. On the other hand, the height of the polystyrene peaks at 1002 cm^{-1} and 1032 cm^{-1} are constant for all Raman spectra.

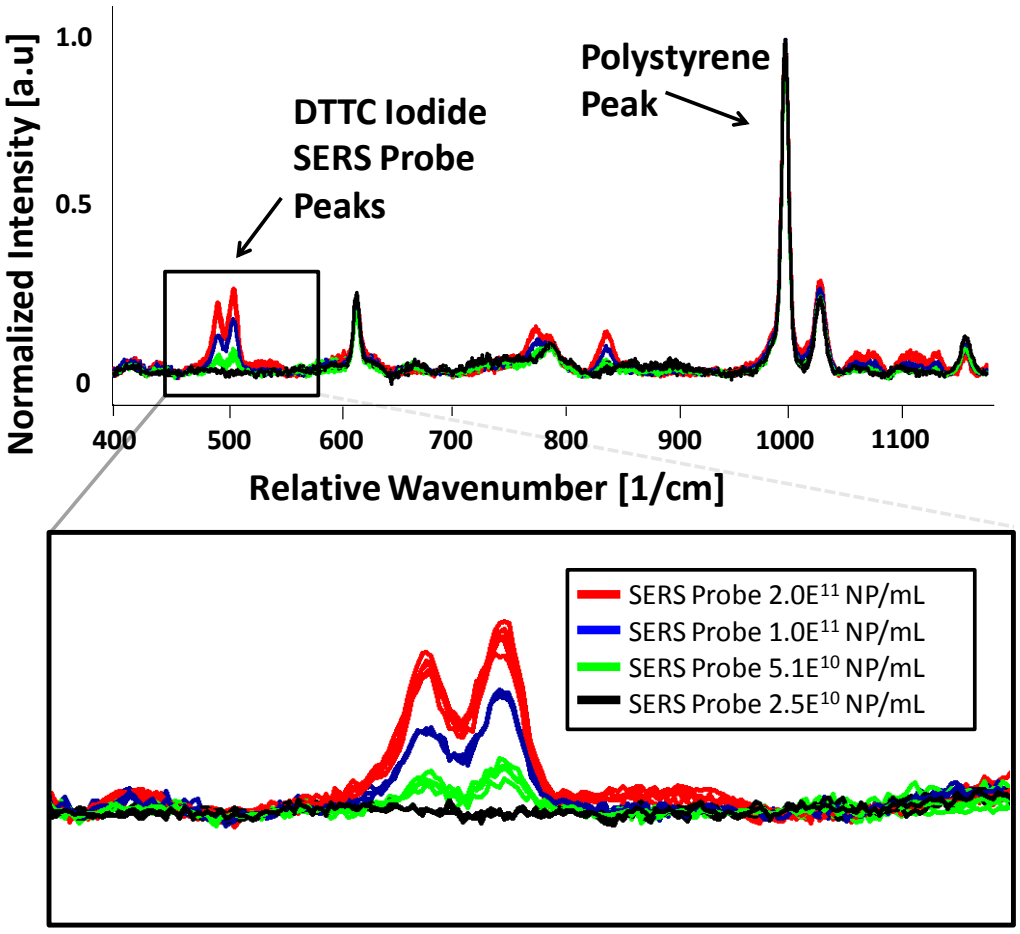

Figure 5.16 SERS Probe Immunoassay Measured Using Raman Spectroscopy. The spectral area of the peaks at 493 cm^{-1} and 508 cm^{-1} can be correlated to the amount of SERS probe nanoparticle added to each well of the immunoassay, while the polystyrene peaks at 1002 cm^{-1} and 1032 cm^{-1} are constant for all immunoassay wells.

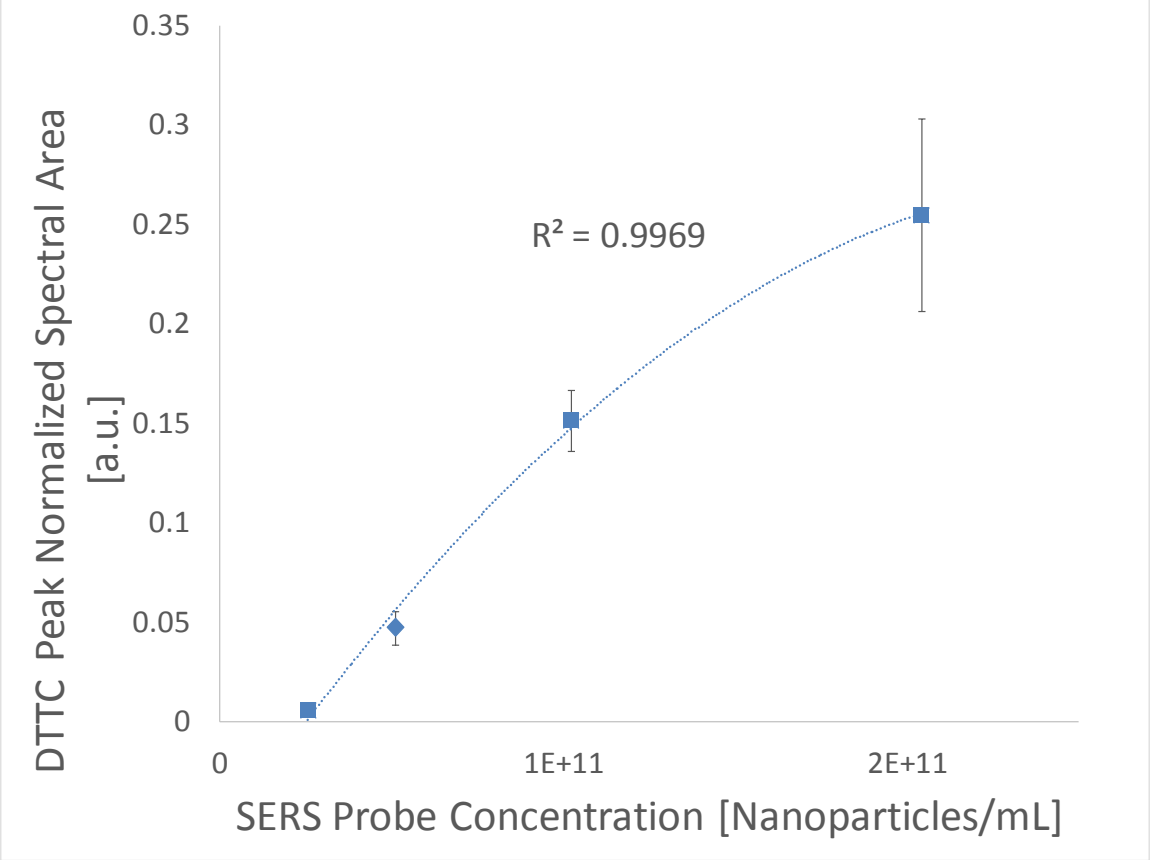

Figure 5.17 Calibration plot of a SERS Probe Immunoassay Measured With Raman. There is a non-linear relationship between the concentration of SERS probe antibody added to the assay and the resulting spectral area of the DTTC peak. This relationship is consistent with binding site limited antibody adhesion seen with high concentrations of secondary antibody.

This assay demonstrates the multiplexing capabilities of SERS-based techniques, since the DTTC iodide SERS probes and the polystyrene plate surface were both detected simultaneously. With future development, this assay could be used to quantify multiple uniquely labeled SERS probes that are each designed to target a specific biomarker. This method for multiplex biomarker quantification can be used for sensitive and specific molecular detection within a very narrow spectral range and has applications for the sensitive detection of B-cell surface markers.

5.4 Conclusion

The successful development and testing of SERS probe nanoparticles for the detection of molecular biomarkers has been demonstrated. These probes were fabricated using step-by-step characterization methods to ensure that a balance was maintained between protein stability and nanoparticle aggregation state. A NIR Raman reporter (DTTC) was bound to the SERS probe nanoparticle surface for specific and sensitive recognition. These probes were stabilized with a PEG surface layer and were tested for robustness. Once fabricated and tested, these SERS probes were used in the development of a SERS-based immunoassay. This assay was used for the direct detection of molecular biomarkers bound to the surface of a polystyrene microplate. The SERS probe signals were detected using both UV/Vis spectroscopy and Raman spectroscopy. Using both methods, the SERS probe signal was correlated to the concentration of SERS probe added to the immunoassay. This method is a novel technique for the testing of SERS probe nanoparticles and shows sensitive results for specific biomarker detection. More information about the experiments and concepts discussed in Chapter 5 can be found in a journal article that is currently under review by the Journal of Biological Engineering.

CHAPTER 6

CONCLUSION AND FUTURE WORK

6.1 Conclusion

Surface-enhanced Raman spectroscopy (SERS) is a valuable analytical technique for the simultaneous detection of multiple biomarkers. The detection of multiple biomarkers is specifically important for treatment of B-cell malignancies such as leukemia, myeloma, and lymphoma. The effective treatment of these lymphoproliferative disorders requires targeted immunophenotyping. Successful immunophenotyping can require the simultaneous detection of up to 20 different cell surface markers (CSM). Traditional methods for biomarker detection are not capable of the simultaneous detection of such large numbers of CSMs. This thesis explored methods for the development of SERS probe nanoparticles for the detection of biomarkers, as a potential solution for increased multiplex biomarker detection.

Before the development of these SERS probe nanoparticles, an appropriate Raman system was required. Several commercial Raman instruments were evaluated based on the factors of excitation wavelength, spectral resolution, spectral range, and system sensitivity. In the process of evaluating these systems, a sensitive SERS substrate was developed based on the galvanic displacement of sliver nitrate onto a copper surface. In addition, a demonstration of the multiplexing capabilities of Raman spectroscopy was performed using mixtures of different solvents. After system evaluation two Raman systems were selected, a Renishaw InVia Raman microscope with a 633nm excitation source, and a custom Raman microscope system with a 785nm excitation source.

To complete the custom Raman microscope system a Nikon TE2000 inverted microscope was modified for Raman based detection. As part of this modification, a 785nm single mode laser was coupled to the microscope through a laser entry port. Laser light was scattered off the sample in a backscattering configuration. Removal of the Rayleigh scattering occurred using a series of long-pass filters that effectively reduced the laser scattering signal so that weak Raman scattering could be observed. The Raman scattered light was dispersed and imaged using a Princeton Instruments Isoplane 160 spectrometer and PIXIS 400 Detector. This Raman microscope was successfully used for sensitive Raman and SERS measurements. Subsequent experiments with SERS probe nanoparticle were performed with this system.

Using the custom 785nm Raman microscope and other characterization methods, SERS probe nanoparticles were fabricated and tested. Initial characterization of unconjugated SERS probes was used to develop a protocol to produce SERS probes that are robust and produce a strong and consistent signal. Conjugation of polyclonal antibodies to the probe surface enabled the specific detection of IgG biomarkers bound to the surface of a polystyrene microplate. This detection schema shows promise for multiplex biomarker analysis. It also illustrates a fabrication method that could be employed for the targeted detection of multiple CSMs commonly found in B-cell malignancies.

6.2 Engineering Significance

The development of a SERS-based immunoassay using a polystyrene microplate substrate is a novel technique with process engineering applications. Polystyrene microplates are commonly used in traditional immunoassays, but are rarely used with Raman spectroscopy because polystyrene produces strong Raman peaks. This thesis demonstrates that by optimizing the Raman reporter molecule, a sensitive SERS-based immunoassay can be developed using a

polystyrene substrate. Significant infrastructure has been developed in the immunoassay industry for 96-well and 384-well polystyrene microplates including machinery to automate the immunoassay process. The use of polystyrene plates for SERS-based biomarker detection can enable the simultaneous detection of multiple proteins while using the existing infrastructure that has been developed for traditional immunoassays.

6.3 Future Work

The development of this SERS-based immunoassay provides a platform for testing and optimization of SERS probe nanoparticles and targeting of more unique antigens. Possible future experiments may demonstrate the actual targeting of a B-cell biomarker. An approach to the experimental plan for this assay uses the CD20 antigen, a B-cell biomarker. The CD20 antigen with a Glutathione S-transferases (GST) protein tag could be bound to an immunoassay plate that has been coated with glutathione. The GST-glutathione interaction is an incomplete enzymatic reaction that causes binding of the CD20 protein to the immunoassay plate without disrupting the CD20 antibody-binding site. After CD20 antigen binding, a mouse monoclonal anti-CD20 antibody could be added to the immunoassay for specific targeting of the CD20 antigen. Following anti-CD20 binding, anti-mouse SERS probes could be added for SERS-based detection of CD20. Figure 6.1, illustrates the proposed experimental design for this assay.

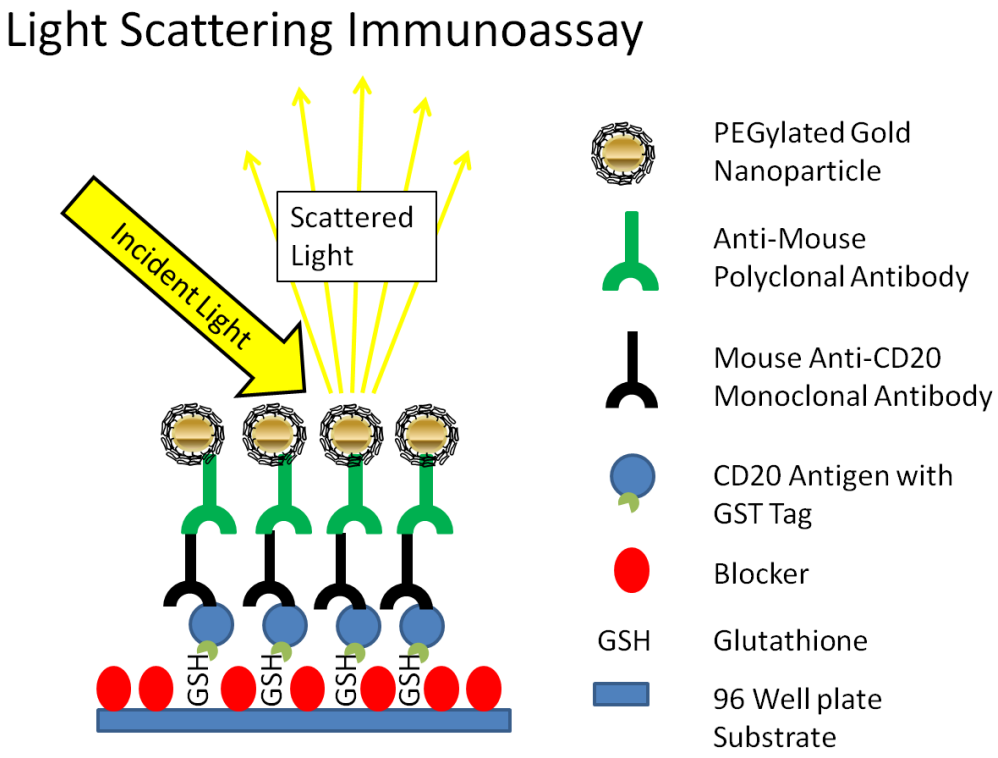

Figure 6.1 CD20 SERS Immunoassay. Proposed SERS immunoassays design for the detection of CD20 a B-cell biomarker. The CD20 antigen is bound to the polystyrene plate surface through an incomplete enzymatic reaction of the GST enzyme with immobilized gluthathione. Detection of the CD20 antigen may be achieved through binding of an anti-CD20 antibody followed by an anti-mouse SERS probe secondary antibody.

REFERENCES

1. Klastersky J, Aoun M. Opportunistic infections in patients with cancer. Ann Oncol 2004, 15:329–335.

2. Non-hodgkin lymphoma - SEER stat fact sheets. http://seer.cancer.gov/statfacts/html/nhl.html. Accessed 28 Nov. 2015

3. Shipp MA, Harrington DP, Anderson JR. A predictive model for aggressive non-Hodgkin's lymphoma. N Engl J Med 1993, 329:987–994.

4. Vaqué JP, Martínez N, Batlle-López A, Pérez C, et al. B-cell lymphoma mutations: improving diagnostics and enabling targeted therapies. Haematologica 2014, 99:222–231.

5. Kneipp K, Wang Y, Kneipp H, Perelman LT, et al. Single molecule detection using surface-enhanced Raman scattering (SERS). Phys Rev Lett 1997, 78:1667–1670.

6. Lee HM, Jin SM, Kim HM, Suh YD: Single-molecule surface-enhanced Raman spectroscopy: a perspective on the current status. Phys Chem Chem Phys 2013, 15:5276–5287.

7. Lim D-K, Jeon K-S, Kim HM, Nam J-M, et al. Nanogap-engineerable Raman-active nanodumbbells for single-molecule detection. Nat Mater 2010, 9:60–67.

8. Dieringer JA, Wustholz KL, Masiello DJ, Camden JP, Kleinman et al. Surface-enhanced Raman excitation spectroscopy of a single rhodamine 6G molecule. J Am Chem Soc 2009, 131:849–854.

9. Cañamares MV, Chenal C, Birke RL, Lombardi JR. DFT, SERS, and single-molecule SERS of crystal violet. J Phys Chem C 2008, 112:20295–20300.

10. Etchegoin PG, Lacharmoise PD, Le Ru EC. Influence of photostability on single-molecule surface enhanced Raman scattering enhancement factors. Anal Chem 2009, 81:682–688.

11. Manson J, Kumar D, Meenan BJ, Dixon D. Polyethylene glycol functionalized gold nanoparticles: the influence of capping density on stability in various media. Gold Bull 2011, 44:99–105.

12. Seol SK, Kim D, Jung S, Chang WS, et al. One-step synthesis of peg-coated gold nanoparticles by rapid microwave heating. J Nanomater 2013, 2013:e531760.

13. Šimáková P, Gautier J, Procházka M, Hervé-Aubert K, et al. Polyethylene-glycol-stabilized Ag nanoparticles for surface-enhanced Raman scattering spectroscopy: Ag surface accessibility studied using metalation of free-base porphyrins. J Phys Chem C 2014, 118:7690–7697.

14. Stiufiuc R, Iacovita C, Nicoara R, Stiufiuc G, et al. One-step synthesis of PEGylated gold nanoparticles with tunable surface charge. J Nanomater 2013, 2013:e146031.

15. Chen H, Paholak H, Ito M, Sansanaphongpricha K, et al. “Living” PEGylation on gold nanoparticles to optimize cancer cell uptake by controlling targeting ligand and charge densities. Nanotechnology 2013, 24.

16. Zhang X-D, Wu D, Shen X, Liu P-X, et al. Size-dependent in vivo toxicity of PEG-coated gold nanoparticles. Int J Nanomedicine 2011, 6:2071–2081.

17. Alcantar NA, Aydil ES, Israelachvili JN. Polyethylene glycol–coated biocompatible surfaces. J Biomed Mater Res 2000, 51:343–351.

18. Kim J, Dadsetan M, Ameenuddin S, Windebank AJ,et al. In vivo biodegradation and biocompatibility of PEG/sebacic acid-based hydrogels using a cage implant system. J Biomed Mater Res A 2010, 95A:191–197.

19. Jain A, Liu R, Xiang YK, Ha T. Single-molecule pull-down for studying protein interactions. Nat Protoc 2012, 7:445–452.

20. Charles PT, Stubbs VR, Soto CM, Martin BD, et al. Reduction of non-specific protein adsorption using poly(ethylene) glycol (peg) modified polyacrylate hydrogels in immunoassays for staphylococcal enterotoxin b detection. Sensors 2009, 9:645–655.

21. Dinish US, Balasundaram G, Chang Y-T, Olivo M. Actively targeted in vivo multiplex detection of intrinsic cancer biomarkers using biocompatible SERS nanotags. Sci Rep 2014, 4.

22. Qian X, Peng X-H, Ansari DO, Yin-Goen Q, et al. In vivo tumor targeting and spectroscopic detection with surface-enhanced Raman nanoparticle tags. Nat Biotechnol 2008, 26:83–90.

23. Salehi M, Schneider L, Ströbel P, Marx A, et al. Two-color SERS microscopy for protein co-localization in prostate tissue with primary antibody–protein A/G–gold nanocluster conjugates. Nanoscale 2014, 6:2361–2367.

24. McFarland AD, Young MA, Dieringer JA, Van Duyne RP: Wavelength-scanned surface-enhanced Raman excitation spectroscopy. J Phys Chem B 2005, 109:11279–11285.

25. Shkilnyy A, Soucé M, Dubois P, Warmont F, et al. Poly(ethylene glycol)-stabilized silver nanoparticles for bioanalytical applications of SERS spectroscopy. Analyst 2009, 134:1868–1872.

26. Lutz B, Dentinger C, Sun L, Nguyen L, et al. Raman nanoparticle probes for antibody-based protein detection in tissues. J Histochem Cytochem 2008, 56:371–379.

27. Lim D-K, Jeon K-S, Hwang J-H, Kim H, et al. Highly uniform and reproducible surface-enhanced Raman scattering from DNA-tailorable nanoparticles with 1-nm interior gap. Nat Nanotechnol 2011, 6:452–460.

28. Goossens T, Klein U, Küppers R. Frequent occurrence of deletions and duplications during somatic hypermutation: Implications for oncogene translocations and heavy chain disease. Proc Natl Acad Sci 1998, 95:2463–2468.

29. Dunn-Walters D, Thiede C, Alpen B, Spencer J. Somatic hypermutation and B-cell lymphoma. Philos Trans R Soc Lond Ser B 2001, 356:73–82.

30. Shaffer AL, Rosenwald A, Staudt LM. Lymphoid Malignancies: the dark side of B-cell differentiation. Nat Rev Immunol 2002, 2:920–933.

31 Janeway CA, Travers P, Walport M, Shlomchik MJ. B-cell activation by armed helper T cells. 2001.

32. Kindt TJ, Goldsby RA, Osborne BA, Kuby J. Kuby Immunology. Macmillan; 2007.

33. Crotty S, Felgner P, Davies H, Glidewell J, et al. Cutting edge: long-term B cell memory in humans after smallpox vaccination. J Immunol 2003, 171:4969–4973.

34. Rickert RC. New insights into pre-BCR and BCR signalling with relevance to B cell malignancies. Nat Rev Immunol 2013, 13:578–591.

35. Mertens D, Stilgenbauer S. Prognostic and predictive factors in patients with chronic lymphocytic leukemia: relevant in the era of novel treatment approaches? J Clin Oncol 2014, 32:869–872.

36. Shaknovich R, Melnick A. Epigenetics and B-cell lymphoma. Curr Opin Hematol 2011, 18:293–299.

37. Mazan-Mamczarz K, Gartenhaus RB. Role of microRNA deregulation in the pathogenesis of diffuse large B-cell lymphoma (DLBCL). Leuk Res 2013, 37:1420–1428.

38. Augello C, Gianelli U, Savi F, Moro A, et al. MicroRNA as potential biomarker in HCV-associated diffuse large B-cell lymphoma. J Clin Pathol 2014, 67:697–701.

39. Strauchen JA. Malignant lymphomas: cell surface markers and advances in classification. West J Med 1981, 135:276–284.

40. Dillman RO. Immunophenotyping of chronic lymphoid leukemias. J Clin Oncol 2008, 26:1193–1194.

41. Zola H, Swart B, Nicholson I, Aasted B, et al. CD molecules 2005: human cell differentiation molecules. Blood 2005, 106:3123–3126.

42. Campbell SM, Peters SB, Zirwas MJ, Wong HK. Immunophenotypic diagnosis of primary cutaneous lymphomas. J Clin Aesthetic Dermatol 2010, 3:21–25.

43. Reilly JT, Bain BJ, England JM, Hyde K, et al. The role of cytology, cytochemistry, immunophenotyping and cytogenetic analysis in the diagnosis of haematological neoplasms. Clin Lab Haematol 1996, 18:231–236.

44. Yeoh E-J, Ross ME, Shurtleff SA, Williams WK, et al. Classification, subtype discovery, and prediction of outcome in pediatric acute lymphoblastic leukemia by gene expression profiling. Cancer Cell 2002, 1:133–143.

45. Raimondi SC, Behm FG, Roberson PK, Williams DL, et al. Cytogenetics of pre-B-cell acute lymphoblastic leukemia with emphasis on prognostic implications of the t(1;19). J Clin Oncol Off J Am Soc Clin Oncol 1990, 8:1380–1388.

46. Pui CH, Frankel LS, Carroll AJ, Raimondi SC, et al. Clinical characteristics and treatment outcome of childhood acute lymphoblastic leukemia with the t(4;11)(q21;q23): a collaborative study of 40 cases. Blood 1991, 77:440–447.

47. Evens AM, Winter JN, Gordon LL, Chiu BCH, et al. Non-Hodgkin lymphoma. Physicians Pract 2014.

48. Craig FE. Flow cytometric evaluation of B-cell lymphoid neoplasms. Clin Lab Med 2007, 27:487–512, vi.

49. Marotta G, Raspadori D, Sestigiani C, Scalia G, et al. Expression of the CD11c antigen in b-cell chronic lymphoproliferative disorders. Leuk Lymphoma 2000, 37:145–149.

50. Inoue T, Yoshida M, Oowashi K, Yoshida T. CD5-positive B-cell prolymphocytic leukemia. Rinshō Ketsueki Jpn J Clin Hematol 2010, 51:80–82.

51. Naeim F, Rao PN, Song S, Grody WW. Atlas of hematopathology: morphology, immunophenotype, cytogenetics, and molecular approaches. Academic Press; 2012.

52. Tuffaha MSA. Phenotypic and genotypic diagnosis of malignancies: an immunohistochemical and molecular approach. John Wiley & Sons; 2008.

53. Salama ME, Lossos IS, Warnke RA, Natkunam Y. Immunoarchitectural patterns in nodal marginal zone B-cell lymphoma: A study of 51 cases. Am J Clin Pathol 2009, 132:39–49.

54. Bautista-Quach MA, Ake CD, Chen M, Wang J. Gastrointestinal lymphomas: morphology, immunophenotype and molecular features. J Gastrointest Oncol 2012, 3:209–225.

55. Kost CB, Holden JT, Mann KP. Marginal zone B-cell lymphoma: a retrospective immunophenotypic analysis. Cytometry B Clin Cytom 2008, 74:282–286.

56. Ando M, Isobe Y, Sasaki M, Sugimoto K, et al. Diffuse large B-cell lymphoma expressing surface immunoglobulin heavy chain (Ig alpha) and lacking light chains. Rinshō Ketsueki Jpn J Clin Hematol 2005, 46:492–495.

57. Gorczyca W. Atlas of differential diagnosis in neoplastic hematopathology, Third Edition. CRC Press; 2014.

58. Gunvén P, Klein G, Klein E, Norin T, et al. Surface immunoglobulins on Burkitt's lymphoma biopsy cells from 91 patients. Int J Cancer J Int Cancer 1980, 25:711–719.

59. Maruta A, Motomura S, Ogawa K, Matsuzaki M, et al. B-prolymphocytic leukemia cells that form rosettes with sheep red blood cells through monoclonal surface immunoglobulin. Am J Hematol 1985, 20:275–281.

60. Seegmiller AC, Xu Y, McKenna RW, Karandikar NJ. Immunophenotypic differentiation between neoplastic plasma cells in mature b-cell lymphoma vs plasma cell myeloma. Am J Clin Pathol 2007, 127:176–181.

61. Kelemen K, Braziel RM, Gatter K, Bakke TC, et al. Immunophenotypic variations of burkitt lymphoma. Am J Clin Pathol 2010, 134:127–138.

62. Herzenberg LA, Tung J, Moore WA, Herzenberg LA, et al. Interpreting flow cytometry data: a guide for the perplexed. Nat Immunol 2006, 7:681–685.

63. Oudejans JJ, van der Valk P. Immunohistochemical classification of B cell neoplasms. J Clin Pathol 2003, 56:193.

64. Van der Loos C: User protocol for multi-color immunohistochemistry staining in intact tissue. BioTecniques 2009:35.

65. Semrock - Flow Cytometry. http://www.semrock.com/flow-cytometry.aspx. Accessed 28 November 2015.

66. Bocsi J, Melzer S, Dähnert I, Tárnok A. 10-Color, 13 antibody panel for in-depth phenotyping of human peripheral blood leukocytes. Cytometry A 2014, 85:781–784.

67. Fluorescence SpectraViewer. http://www.lifetechnologies.com/us/en/home/life-science/cell-analysis/labeling-chemistry/fluorescence-spectraviewer.html. Accessed 28 November 2015.

68. Ekimov AI, Onushchenko AA. Quantum size effect in three-dimensional microscopic semiconductor crystals. Sov J Exp Theor Phys Lett 1981, 34:345.

69. Kim JY, Voznyy O, Zhitomirsky D, Sargent EH. Colloidal quantum dot materials and devices: a quarter-century of advances. Adv Mater 2013, 25:4986–5010.

70. Bera D, Qian L, Tseng T-K, Holloway PH. Quantum dots and their multimodal applications: a review. Materials 2010, 3:2260–2345.

71. Hess O, Gehrig E. Photonics of quantum-dot nanomaterials and devices: theory and modelling. World Scientific; 2012.

72. Han M, Gao X, Su JZ, Nie S. Quantum-dot-tagged microbeads for multiplexed optical coding of biomolecules. Nat Biotechnol 2001, 19:631–635.

73. Xing Y, Chaudry Q, Shen C, Kong KY, et al. Bioconjugated quantum dots for multiplexed and quantitative immunohistochemistry. Nat Protoc 2007, 2:1152–1165.

74. Tsoi KM, Dai Q, Alman BA, Chan WCW. Are quantum dots toxic? Exploring the discrepancy between cell culture and animal studies. Acc Chem Res 2013, 46:662–671.

75. Yong K-T, Law W-C, Hu R, Ye L, et al. Nanotoxicity assessment of quantum dots: from cellular to primate studies. Chem Soc Rev 2013, 42:1236–1250.

76. Ye L, Yong K-T, Liu L, Roy I, et al. A pilot study in non-human primates shows no adverse response to intravenous injection of quantum dots. Nat Nanotechnol 2012, 7:453–458.

77. Greeneltch NG, Davis AS, Valley NA, Casadio F, et al. Near-infrared surface-enhanced Raman spectroscopy (NIR-SERS) for the identification of eosin y: theoretical calculations and evaluation of two different nanoplasmonic substrates. J Phys Chem A 2012, 116:11863–11869.

78. Lutz B, Dentinger C, Sun L, Nguyen L, et al. Raman nanoparticle probes for antibody-based protein detection in tissues. J Histochem Cytochem 2008, 56:371–379.

79. Wang Y, Schlücker S. Rational design and synthesis of SERS labels. Analyst 2013, 138:2224–2238.

80. Zavaleta CL, Smith BR, Walton I, Doering W, et al. Multiplexed imaging of surface enhanced Raman scattering nanotags in living mice using noninvasive Raman spectroscopy. Proc Natl Acad Sci 2009, 106:13511–13516.

81. Gao Y, Li Y, Wang Y, Chen Y, et al. Controlled synthesis of multilayered gold nanoshells for enhanced photothermal therapy and SERS detection. Small 2015, 11:77–83.

82. Zhao L, Kim T-H, Kim H-W, Ahn J-C, et al. Surface-enhanced Raman scattering (SERS)-active gold nanochains for multiplex detection and photodynamic therapy of cancer. Acta Biomater 2015, 20: 155-164.

83. MacLaughlin CM, Mullaithilaga N, Yang G, Ip SY, et al. Surface-enhanced Raman scattering dye-labeled Au nanoparticles for triplexed detection of leukemia and lymphoma cells and SERS flow cytometry. Langmuir ACS J Surf Colloids 2013, 29:1908–1919.

84. Conde J, Bao C, Cui D, Baptista PV, et al. Antibody–drug gold nanoantennas with Raman spectroscopic fingerprints for in vivo tumour theranostics. J Controlled Release 2014, 183:87–93.

85. Raman CV, Krishnan KS. A new type of secondary radiation (Reprinted from Nature, vol 121, pg 501-502, 1928). Curr Sci 1998, 74:381–381.

86. Strutt JW. On the light from the sky, its polarization and colour. Philos Mag Ser 4 1871, 41:107–120.

87. Hayes W, Loudon R. Scattering of light by crystals. Courier Corporation; 2012.

88. Miles RB, Lempert WR, NForkey J. Laser Rayleigh scattering. Meas Sci Technol 2001, 12:R33-R51.

89. Bernath PF. Light scattering and the Raman effect. in spectra of atoms and molecules. second edition. Oxford University Press; 2005:293–317.

90. Atkins PW, Friedman RS. Molecular rotations and vibrations. In: Molecular quantum mechanics fourth edition. Oxford University Press; 2011:342–381.

91. Smith E, Dent G. Introduction in modern Raman spectroscopy: a practical approach. Wiley; 2005:1–21.

92. Harris DC, Bertolucci MD. Symmetry and spectroscopy: an introduction to vibrational and electronic spectroscopy. Courier Corporation; 1978.

93. Wilson EB. Molecular vibrations: the theory of infrared and Raman vibrational spectra. Courier Corporation; 1955.

94. Smith E, Dent G. Modern Raman spectroscopy-a practical approach. John Wiley & Sons, Ltd; 2005.

95. Van Duyne RP, Jeanmaire DL, Shriver DF. Mode-locked laser Raman spectroscopy. New technique for the rejection of interfering background luminescence signals. Anal Chem 1974, 46:213–222.

96. Doering WE, Nie S. Spectroscopic tags using dye-embedded nanoparticles and surface-enhanced Raman scattering. Anal Chem 2003, 75:6171–6176.

97. Van Duyne RP. Laser excitation of Raman scattering from adsorbed molecules on electrode surfaces. In Chemical and Biochemical Applications of Lasers. Edited by MOORE CB. Academic Press; 1979:101–185.

98. Chen L (Ed). Novel optical nanoprobes for chemical and biological analysis. Heidelberg: Springer; 2014. [SpringerBriefs in Molecular Science]

99. Dogra SK. Raman spectroscopy. in molecular spectrocopy. Pearson Education India; 2015.

100. Lewis IR, Edwards H. Handbook of Raman spectroscopy: from the research laboratory to the process line. CRC Press; 2001.

101. Yakovlev VV, Petrov GI, Zhang HF, Noojin GD, et al. Stimulated Raman scattering: old physics, new applications. J Mod Opt 2009, 56:1970–1973.

102. Tolles WM, Nibler JW, McDonald JR, Harvey AB. A review of the theory and application of coherent anti-Stokes Raman spectroscopy (CARS). Appl Spectrosc 1977, 31:253–271.

103. Stiles PL, Dieringer JA, Shah NC, Van Duyne RP. Surface-enhanced Raman spectroscopy. Annu Rev Anal Chem 2008, 1:601–626.

104. Gallagher JW, Brion CE, Samson JAR, Langhoff PW. Absolute cross sections for molecular photoabsorption, partial photoionization, and ionic photofragmentation processes. J Phys Chem Ref Data 1988, 17:9–153.

105. Kastrup L, Hell SW. Absolute optical cross section of individual fluorescent molecules. Angew Chem Int Ed 2004, 43:6646–6649.

106. Kneipp K. Surface-enhanced Raman scattering. Phys Today 2007, 60:40–46.

107. Ory H, Yura HT. Rayleigh and Raman scattering in molecular nitrogen 1965.

108. Fleischmann M, Hendra PJ, McQuillan AJ. Raman spectra of pyridine adsorbed at a silver electrode. Chem Phys Lett 1974, 26:163–166.

109. Campion A, Ivanecky JE, Child CM, Foster M. On the mechanism of chemical enhancement in surface-enhanced raman scattering. J Am Chem Soc 1995, 117:11807–11808.

110. Huang X, El-Sayed MA. Gold nanoparticles: Optical properties and implementations in cancer diagnosis and photothermal therapy. J Adv Res 2010, 1:13–28.

111. Petryayeva E, Krull UJ. Localized surface plasmon resonance: Nanostructures, bioassays and biosensing—A review. Anal Chim Acta 2011, 706:8–24.

112. Grubisic A, Ringe E, Cobley CM, Xia Y, et al. Plasmonic near-electric field enhancement effects in ultrafast photoelectron emission: correlated spatial and laser polarization microscopy studies of individual Ag nanocubes. Nano Lett 2012, 12:4823–4829.

113. Laven P. MiePlot. English; 2015.

114. Bohren CF. Absorption and scattering of light by small particles. New York: Wiley; 1983.

115. Kreibig U, Vollmer M. Optical properties of metal clusters. Springer; 1995.

116. Haes AJ, Duyne RPV. A unified view of propagating and localized surface plasmon resonance biosensors. Anal Bioanal Chem 2004, 379:920–930.

117. Indrasekara ASDS, Meyers S, Shubeita S, Feldman LC, et al. Gold nanostar substrates for SERS-based chemical sensing in the femtomolar regime. Nanoscale 2014, 6:8891–8899.

118. Cheng I-F, Chang H-C, Chen T-Y, Hu C, et al. Rapid (<5 min) identification of pathogen in human blood by electrokinetic concentration and surface-enhanced Raman spectroscopy. Sci Rep 2013, 3.

119. Shanmukh S, Jones L, Driskell J, Zhao Y, et al. Rapid and sensitive detection of respiratory virus molecular signatures using a silver nanorod array sers substrate. Nano Lett 2006, 6:2630–2636.

120. Maiti KK, Dinish US, Samanta A, Vendrell M, et al. Multiplex targeted in vivo cancer detection using sensitive near-infrared SERS nanotags. Nano Today 2012, 7:85–93.

121. Aydin Ö, Kahraman M, Kiliç E, Çulha M. Surface-enhanced Raman scattering of rat tissues. Appl Spectrosc 2009, 63:662–668.

122. Fierro-Mercado PM, Hernandez-Rivera SP. Highly sensitive filter paper substrate for SERS trace explosives detection. Int J Spectrosc 2012, 2012:e716527.

123. Mulvihill M, Tao A, Benjauthrit K, Arnold J,et al. Surface-enhanced Raman spectroscopy for trace arsenic detection in contaminated water. Angew Chem Int Ed 2008, 47:6456–6460.

124. Londero PS, Lombardi JR, Leona M. Laser ablation surface-enhanced Raman microspectroscopy. Anal Chem 2013, 85:5463–5467.

125. Ahijado-Guzmán R, Gómez-Puertas P, Alvarez-Puebla RA, Rivas G, et al. Surface-enhanced Raman scattering-based detection of the interactions between the essential cell division FtsZ protein and bacterial membrane elements. ACS Nano 2012, 6:7514–7520.

126. Han XX, Zhao B, Ozaki Y. Surface-enhanced Raman scattering for protein detection. Anal Bioanal Chem 2009, 394:1719–1727.

127. Meyer SA, Auguié B, Le Ru EC, Etchegoin PG. Combined SPR and SERS Microscopy in the Kretschmann Configuration. J Phys Chem A 2011, 116:1000–1007.

128. Natan MJ. Concluding remarks: surface enhanced Raman scattering. Faraday Discuss 2006, 132:321–328.

129. Diebold ED, Mack NH, Doorn SK, Mazur E. Femtosecond laser-nanostructured substrates for surface-enhanced Raman scattering. Langmuir 2009, 25:1790–1794.

130. Nergiz SZ, Gandra N, Farrell ME, Tian L, et al. Biomimetic SERS substrate: peptide recognition elements for highly selective chemical detection in chemically complex media. J Mater Chem A 2013, 1:6543–6549.

131. Lin X-M, Cui Y, Xu Y-H, Ren B, et al. Surface-enhanced Raman spectroscopy: substrate-related issues. Anal Bioanal Chem 2009, 394:1729–1745.

132. Yang L, Li P, Liu J. Progress in multifunctional surface-enhanced Raman scattering substrate for detection. RSC Adv 2014, 4:49635–49646.

133. Gómez M, Lazzari M. Reliable and cheap SERS active substrates. Mater Today 2014, 17:358–359.

134. Gutés A, Carraro C, Maboudian R. Silver dendrites from galvanic displacement on commercial aluminum foil as an effective SERS substrate. J Am Chem Soc 2010, 132:1476–1477.

135. Tague T. Infrared and Raman microscopy: complimentary or redundant techniques? Microsc Microanal 2007, 13(Supplement S02):1696–1697.

136. Adar F, Mamedov S, Whitely A. Limits of spatial resolution of a Raman microscope. Microsc Microanal 2005, 11(Supplement S02):728–729.

137. Hollricher O. Combine and conquer: confocal Raman microscopy teams high-resolution capabilities with powerful materials analysis. SPIE Biomed Opt Med Imaging 2003.

138. Fox CB, Myers GA, Harris JM. Temperature-controlled confocal Raman microscopy to detect phase transitions in phospholipid vesicles. Appl Spectrosc 2007, 61:465–469.

139. Salzmann CG, Kohl I, Loerting T, Mayer E, et al. Raman spectroscopic study on hydrogen bonding in recovered ice IV. J Phys Chem B 2003, 107:2802–2807.

140. Maiti NC, Apetri MM, Zagorski MG, Carey PR, et al. Raman spectroscopic characterization of secondary structure in natively unfolded proteins: α-synuclein. J Am Chem Soc 2004, 126:2399–2408.

141. Dračínský M, Procházková E, Kessler J, Šebestík J,et al. Resolution of organic polymorphic crystals by Raman spectroscopy. J Phys Chem B 2013, 117:7297–7307.

142. Liu Z-J, Zhao C-H, Han L-G, Mo Y-J. Study on the configuration and applications of high spectral resolution Raman spectrometer. Guang Pu Xue Yu Guang Pu Fen Xi Guang Pu 2010, 30:567–570.

143. Hemmi N, Zimmerman KA, Dreger ZA, Gupta YM. High spectral resolution, real-time, Raman spectroscopy in shock compression experiments. Rev Sci Instrum 2011, 82:083109.

144. Bei-Jing Z, Fu-Sheng L, Ning-Chao Z, Li-Peng F, et al. A high-spectral-resolution laser Raman system and its application in shock compressed benzene. Chin Phys Lett 2013, 30:030701.

145. Sensitivity of CCD cameras - Key factors to consider. http://www.andor.com/learning-academy/sensitivity-of-ccd-cameras-key-factors-to-consider Accessed 28 November 2015.

146. Zhu Z. Thermally generated leakage current mechanisms of metal-induced laterally crystallized n-type poly-Si TFTs under hot-carrier stress. Solid-State Electron 2011, 62:62–66.

147. Widenhorn R, Blouke MM, Weber A, Rest A,et al. Temperature dependence of dark current in a CCD. Volume 4669; 2002:193–201.

148. Nie C-S, Feng Z. Simple preparation method for silver SERS substrate by reduction of AgNO3 on copper foil. Appl Spectrosc 2002, 56:300–305.

149. Zhou Y, Cao H. An augmented classical least squares method for quantitative Raman spectral analysis against component information loss. Sci World J 2013, 2013:e306937.

150. Pallaoro A, Hoonejani MR, Braun GB, Meinhart CD,et al. Rapid identification by surface-enhanced Raman spectroscopy of cancer cells at low concentrations flowing in a microfluidic channel. ACS Nano 2015.

151. Balslev I, Larsen JE, Larsen S. Noise amplification and resolution improvement in deconvolution of experimental spectra. Appl Spectrosc 1978, 32:454–457.

152. Nikon MicroscopyU | Fluorescence Microscopy | Filter Combinations. http://www.microscopyu.com/articles/fluorescence/filtercubes/filterindex.html. Accessed 28 November 2015.

153. Singh SP, Gangwar R, Singh N. Nonlinear scattering effects in optical fibers. Prog Electromagn Res 2007, 74:379–405.

154. Palmer C, Loewen E. Diffraction grating handbook. sixth edition. Newport Corporation; 2005.

155. Lerner JM. Imaging spectrometer fundamentals for researchers in the biosciences—A tutorial. Cytometry A 2006, 69A:712–734.

156. Lee W, Lee H, Hahn JW. Correction of spectral deformation by second-order diffraction overlap in a mid-infrared range grating spectrometer using a PbSe array detector. Infrared Phys Technol 2014, 67:327–332.

157. Princeton Instruments - Imaging. http://www.princetoninstruments.com/products/imcam/pixis/ Accessed 28 November 2015.

158. NIST Atomic Spectra Database. http://www.nist.gov/pml/data/asd.cfm. Accessed 28 November 2015.

159. Princeton Instruments: Automated Wavelength and Intensity Calibration Routines. 2015.

160. McCusker LB, Von Dreele RB, Cox DE, Louër D, et al. Rietveld refinement guidelines. J Appl Crystallogr 1999, 32:36–50.

161. Chegel V, Rachkov O, Lopatynskyi A, Ishihara S, et al. Gold nanoparticles aggregation: drastic effect of cooperative functionalities in a single molecular conjugate. J Phys Chem C 2012, 116:2683–2690.

162. Tan T, Tian C, Ren Z, Yang J, et al. LSPR-dependent SERS performance of silver nanoplates with highly stable and broad tunable LSPRs prepared through an improved seed-mediated strategy. Phys Chem Chem Phys PCCP 2013, 15:21034–21042.

163. Mahmoud MA, El-Sayed MA. Aggregation of gold nanoframes reduces, rather than enhances, SERS efficiency due to the trade-off of the inter- and intraparticle plasmonic fields. Nano Lett 2009, 9:3025–3031.

164. Schwartzberg AM, Grant CD, Wolcott A, Talley CE, et al. Unique gold nanoparticle aggregates as a highly active surface-enhanced Raman scattering substrate. J Phys Chem B 2004, 108:19191–19197.

165. Radziuk D, Moehwald H. Highly effective hot spots for SERS signatures of live fibroblasts. Nanoscale 2014, 6:6115.

166. Moskovits M. Surface-enhanced Raman spectroscopy: a brief retrospective. J Raman Spectrosc 2005, 36:485–496.

167. Drenth J. Principles of protein x-ray crystallography. Springer Science & Business Media; 1999.

168. Hall GM. Methods of testing protein functionality. Springer Science & Business Media; 1996.

169. Hassan PA, Rana S, Verma G. Making sense of brownian motion: colloid characterization by dynamic light scattering. Langmuir 2015, 31:3–12.

170. Berne BJ, Pecora R. Dynamic light scattering: with applications to chemistry, biology, and physics. Courier Corporation; 2000.

171. Li L, Steiner U, Mahajan S. Single nanoparticle SERS probes of ion intercalation in metal-oxide electrodes. Nano Lett 2014, 14:495–498.

172. Cui Y, Phang IY, Lee YH, Lee MR, et al. Multiplex plasmonic anti-counterfeiting security labels based on surface-enhanced Raman scattering. Chem Commun 2015, 51:5363–5366.

173. Jadzinsky PD, Calero G, Ackerson CJ, Bushnell DA, et al. Structure of a thiol monolayer-protected gold nanoparticle at 1.1 å resolution. Science 2007, 318:430–433. [New Series]

174. Woehrle GH, Brown LO, Hutchison JE. Thiol-functionalized, 1.5-nm gold nanoparticles through ligand exchange reactions: scope and mechanism of ligand exchange. J Am Chem Soc 2005, 127:2172–2183.

175. Kurfürst MM. Detection and molecular weight determination of polyethylene glycol-modified hirudin by staining after sodium dodecyl sulfate-polyacrylamide gel electrophoresis. Anal Biochem 1992, 200:244–248.

176. Sims GEC, Snape TJ. A method for the estimation of polyethylene glycol in plasma protein fractions. Anal Biochem 1980, 107:60–63.

177. Chapman AP. PEGylated antibodies and antibody fragments for improved therapy: a review. Adv Drug Deliv Rev 2002, 54:531–545.

178. Leng SX, McElhaney JE, Walston JD, Xie D, et al. Elisa and multiplex technologies for cytokine measurement in inflammation and aging research. J Gerontol A Biol Sci Med Sci 2008, 63:879–884.

179. Grating Dispersion Calculator. http://www.princetoninstruments.com/spectroscopy/calculator/ Accessed 28 November 2015.

APPENDIX A

SUPPLEMENTARY FIGURES

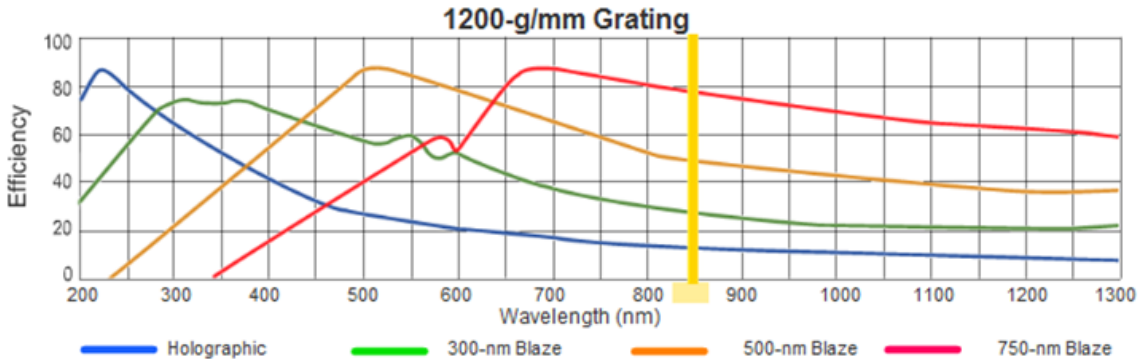

Figure A1: Princeton Instruments Grating Profile. The quantum efficiency of the grating used in the Raman microscope design is presented for several grating blaze angles; a 750 nm blaze grating was used in the custom Raman microscope design. Grating efficiency data was obtained using the Princeton Instruments grating dispersion calculator [179].

APPENDIX B

CONSENT/PERMISSION TO REPRINT

B1.0 Permission to reprint Figure 2.1

NATURE PUBLISHING GROUP LICENSE
TERMS AND CONDITIONS

Nov 28, 2015

This is a License Agreement between Nathan D Israelsen ("You") and Nature Publishing Group ("Nature Publishing Group") provided by Copyright Clearance Center ("CCC"). The license consists of your order details, the terms and conditions provided by Nature Publishing Group, and the payment terms and conditions.

License Number	3757820805243
License date	Nov 28, 2015
Licensed content publisher	Nature Publishing Group
Licensed content publication	Nature Reviews Immunology
Licensed content title	New insights into pre-BCR and BCR signalling with relevance to B cell malignancies
Licensed content author	Robert C. Rickert
Licensed content date	Jul 25, 2013
Volume number	13
Issue number	8
Type of Use	reuse in a dissertation / thesis
Requestor type	academic/educational
Format	print and electronic
Portion	figures/tables/illustrations
Number of figures/tables/illustrations	1
High-res required	no
Figures	Figure 1: B cell neoplasms arise at different stages of B cell differentiation.
Author of this NPG article	no
Your reference number	None
Title of your thesis / dissertation	SURFACE-ENHANCED RAMAN SPECTROSCOPY-BASED BIOMARKER DETECTION FOR B-CELL MALIGNANCIES
Expected completion date	Dec 2015
Estimated size (number of pages)	128
Total	0.00 USD
Terms and Conditions	

Terms and Conditions for Permissions

Nature Publishing Group hereby grants you a non-exclusive license to reproduce this material for this purpose, and for no other use, subject to the conditions below:

1. NPG warrants that it has, to the best of its knowledge, the rights to license reuse of this material. However, you should ensure that the material you are requesting is original to Nature Publishing Group and does not carry the copyright of another entity (as credited in the published version). If the credit line on any part of the material you have requested indicates that it was reprinted or adapted by NPG with permission from another source, then you should also seek permission from that source to reuse the material.

2. Permission granted free of charge for material in print is also usually granted for any electronic version of that work, provided that the material is incidental to the work as a whole and that the electronic version is essentially equivalent to, or substitutes for, the print version. Where print permission has been granted for a fee, separate permission must be obtained for any additional, electronic re-use (unless, as in the case of a full paper, this has already been accounted for during your initial request in the calculation of a print run).NB: In all cases, web-based use of full-text articles must be authorized separately through the 'Use on a Web Site' option when requesting permission.

3. Permission granted for a first edition does not apply to second and subsequent editions and for editions in other languages (except for signatories to the STM Permissions Guidelines, or where the first edition permission was granted for free).

4. Nature Publishing Group's permission must be acknowledged next to the figure, table or abstract in print. In electronic form, this acknowledgement must be visible at the same time as the figure/table/abstract, and must be hyperlinked to the journal's homepage.
5. The credit line should read:
   Reprinted by permission from Macmillan Publishers Ltd: [JOURNAL NAME] (reference citation), copyright (year of publication)
   For AOP papers, the credit line should read:
   Reprinted by permission from Macmillan Publishers Ltd: [JOURNAL NAME], advance online publication, day month year (doi: 10.1038/sj.[JOURNAL ACRONYM].XXXXX)

   Note: For republication from the *British Journal of Cancer,* the following credit lines apply.
   Reprinted by permission from Macmillan Publishers Ltd on behalf of Cancer Research UK: [JOURNAL NAME] (reference citation), copyright (year of publication)For AOP papers, the credit line should read:
   Reprinted by permission from Macmillan Publishers Ltd on behalf of Cancer Research UK: [JOURNAL NAME], advance online publication, day month year (doi: 10.1038/sj.[JOURNAL ACRONYM].XXXXX)

6. Adaptations of single figures do not require NPG approval. However, the adaptation should be credited as follows:

   Adapted by permission from Macmillan Publishers Ltd: [JOURNAL NAME] (reference citation), copyright (year of publication)

   Note: For adaptation from the *British Journal of Cancer,* the following credit line applies.

Adapted by permission from Macmillan Publishers Ltd on behalf of Cancer Research UK: [JOURNAL NAME] (reference citation), copyright (year of publication)

7. Translations of 401 words up to a whole article require NPG approval. Please visithttp://www.macmillanmedicalcommunications.com for more information.Translations of up to a 400 words do not require NPG approval. The translation should be credited as follows:

   Translated by permission from Macmillan Publishers Ltd: [JOURNAL NAME] (reference citation), copyright (year of publication).

   Note: For translation from the *British Journal of Cancer*, the following credit line applies.
   Translated by permission from Macmillan Publishers Ltd on behalf of Cancer Research UK: [JOURNAL NAME] (reference citation), copyright (year of publication)

We are certain that all parties will benefit from this agreement and wish you the best in the use of this material. Thank you.
Special Terms:
v1.1

B2.0 Permission to reprint Figure 2.2

From: Nathan.Israelsen@gmail.com
Sent: Friday, March 27, 2015 7:05 PM
To: semrock@idexcorp.com
Subject: Request to republish flow cytometry figure from your website

To whom it may be concerned,

I would like to use the flow cytometry figure (see attached) published on your website in my master's thesis. The thesis will be published in a university online archive. I will be sure to include an appropriate reference to your website in my document.

Please let me know if you can approve the use of this figure.

Sincerely,

Nathan Israelsen

From: semrock@idexcorp.com
Sent: Mon, Mar 30, 2015 at 7:09 AM
To: Nathan.Israelsen@gmail.com
Subject: FW: Request to republish flow cytometry figure from your website

Hello Nathan,

You are welcome to use our image in your thesis with credit given.

Best of luck on your project.

Amanda MacDonald
Director of Marketing Communications
Idex Optics and Photonics